Friedrich-Alexander-Universität
Faculty of Sciences

Master’s thesis

in Physics

Statistical analysis of atmospheric river projections and their link to extreme precipitation events

Lars Henrik Radtke

Supervisor: Prof. Dr. Michael Schmiedeberg
Institute of Theoretical Physics
Produced at: Potsdam Institute for Climate Impact Research (PIK)

Submission date: 18. March, 2026

Abstract

Atmospheric rivers (ARs) play a crucial role in the global distribution and transportation of moisture and are often linked to extreme precipitation events. While extreme precipitation intensifies with global warming, the relative contribution of atmospheric rivers remains uncertain. This study applies the PIKART algorithm to catalog projected atmospheric rivers from simulated integrated water-vapor transport (IVT) in a multi-model ensemble. A spatial and temporal resolution test showed a strong sensitivity of results, with substantial reductions in AR metrics for coarser grids. Atmospheric river characteristics are then analyzed with 1° spatial and 6 h temporal resolution to determine differences in the future scenarios SSP1-2.6 and SSP5-8.5 to the historical simulation. Results indicate a strong intensity increase, a poleward shift of mid-latitude atmospheric river tracks and a slight decrease in the number of detected annual tracks. Size, shape and lifetime showed no significant differences. Impact-relevant changes of atmospheric rivers are evaluated by their link to extreme precipitation intensity and frequency. Precipitation events are classified as AR-associated when detected footprints spatially overlap on the same day. A low-frequency component analysis on global near-surface air temperature and the extreme precipitation metrics is applied to separate forced radiative trends from internal variability. Land-averaged changes of extreme events, relative to a 1950-1970 historical baseline, are evaluated against global-mean temperature. Exponential scaling rates are estimated and compared to theoretical expectations, resulting in ensemble mean intensity rates of $(5.8 \pm 1.3)\,\%/\mathrm{K}$ for all events, $(7.5 \pm 2.7)\,\%/\mathrm{K}$ for AR-associated events and $(5.2 \pm 1.4)\,\%/\mathrm{K}$ for non-AR events. All rates align with a strong thermodynamic contribution. The frequency of extremes scales with $(12.9 \pm 1.9)\,\%/\mathrm{K}$ for all events, $(18 \pm 7)\,\%/\mathrm{K}$ for AR-associated events and $(12.8 \pm 1.2)\,\%/\mathrm{K}$ for non-AR events. Faster scaling of AR-associated compared to non-AR events is projected in all models for both extreme intensity and frequency, but large uncertainties remain from model spread and low AR event statistics.

Contents

Chapter 1

Introduction

Global population grows increasingly centralized with up to 45 % of our planets population living in cities (*European Commission: Joint Research Center* n.d.), compared to only 20 % in 1950. This concentration exposes large groups to the impacts of spatially small but heavy rainfall events. Climate change strengthens not only the intensity, but also the frequency of these extreme precipitation events, which are therefore important to investigate for future mitigation strategies.

Figure 1.1: True color satellite image of the atmosphere over the Caribbean and North Atlantic Ocean during daytime, showing an atmospheric river stretching from the Caribbean towards Europe. Country borders are shown as white lines for orientation. Figure obtained from `https://www.star.nesdis.noaa.gov/GOES/` on February 3, 2026 at 13:40 (UTC+1).

For many costal regions, extreme precipitation events are closely linked to atmospheric rivers (ARs) with up to 80 % of recent events caused by ARs in Norway (Michel et al. 2021). Atmospheric rivers are processes that transport large amounts of water vapor and occur mostly due to the complex dynamics in the mid-latitudinal troposphere. They span 200 km to 300 km in width and more than 2000 km in length (Guan and Waliser 2019). ARs typically emerge over large ocean basins and travel north-eastward embedded in surface trade winds, while carrying water amounts similar to the worlds largest rivers (Gimeno, Nieto, et al. 2014). Their creation is linked to Rossby-Wave breaking, which creates a sharp temperature gradient and they are usually accompanied by a low-level jet. ARs typically terminate by precipitating down when elevated terrain forces their vertical rise. Four to five ARs are present on the globe at any given time (Gimeno, Nieto, et al. 2014).

ARs are crucial for the hydrological cycle in mid-latitudes, because most water evaporates in the extra-tropics and only small amounts are transported poleward (Etling 2008). Here ARs contribute up to 95 % of this poleward transportation in mid-latitudes (Gimeno, Nieto, et al. 2014). The precipitation of AR carried moisture supplies mid-latitudinal areas with water for vegetation, agricultural industry and the regeneration of fresh water reservoirs. Up to 22 % of total global runoff (Paltan et al. 2017) and 20 % to 30 % of precipitation in western Europe and USA is caused by ARs with strong seasonality (David A. Lavers and Villarini 2015). The current dynamic of ARs are therefore important for the fresh water supply of many mid-latitudinal countries and their agricultural industry.

While large amounts of precipitation is partly beneficial, the continuous supply of moisture can also lead to heavy precipitation events of either extremely long duration or high intensities. The resulting extreme events cause floods and landslides with hazardous effects on local infrastructure and lives. As an example, up to 80 % of floods were linked to ARs and their absence promotes dry periods with following droughts (Paltan et al. 2017). Both floods and droughts can induce large economic damages, if no adaptation strategies are applied.

The increasing global mean air temperature due to climate change increases the evaporation and therefore the input into the hydrological cycle. The amount of additional water vapor in the atmosphere is typically estimated as 7 %/K following Clausius-Clapeyron scaling (Boer 1993). The increased moisture availability impacts the intensity of ARs and leads to stronger, longer and more frequent extreme precipitation events (Jeon et al. 2015). A variety of studies (for example David A. Lavers and Villarini 2015, Warner, Mass, and Jr. 2015, and Jeon et al. 2015) have investigated the impact of climate change on ARs and predict that changes are dominated by thermodynamical over dynamical effects. ARs are therefore not expected to emerge quicker or move faster, but the overall higher intensity can lead to more frequent extreme events and therefore to higher social and economical damage.

The scaling of precipitation extremes due to climate change was recently investigated by Kotz et al. 2023 to an intensity increase of $(6.1 \pm 1.4)\,\%/\mathrm{K}$ and a frequency increase of $(12.0 \pm 3.6)\,\%/\mathrm{K}$. While the scaling of intensity agreed with expectations, the frequency scaling fell short and both estimates were smaller than observations. The contribution of AR-associated extremes to this overall increase remains unknown and will be subject in this study.

The need for automatic detection and tracking algorithms arises quickly in global studies, with up to 10^5 possible ARs per year. Multiple methods have been developed with prominent examples like tARget from Guan and Waliser 2019 and IPART from Xu et al. 2020. The most recent PIKART algorithm published in Vallejo-Bernal et al. 2025 tries to combine the two major advantages of both and produces a catalog with many characteristic information of ARs on observational data. It has, however, not been used to catalog future projections of ARs, which will be done in this work to provide additional confirmation and robustness of the projected AR changes.

This work aims to analyze the scaling of extreme events caused by ARs by producing an AR catalog for future projections of multiple general circulation models. First of all, an ensemble of climate models is selected which includes high-resolution atmospheric data for atmospheric river detection and temperature and precipitation data of the same simulation run to allow the estimation of extreme events and their comparison to increasing global mean temperature. The analysis is done for a historical simulation and two future scenarios with different radiative forcing. The ARs are detected by calculating the integrated water-vapor transport along with a sensitivity test of the detection algorithm for different spatiotemporal resolutions. Results of the catalog are then analyzed for future differences in a large variety of metrics. The extreme precipitation events are then defined in analogy to the work of Kotz et al. 2023. AR events are separated from non-AR events by spatially overlapping the detected AR shapes. A low-frequency component analysis (LFCA) is used as in Kotz et al. 2023 to filter out the climate change signal and reduce noise. The LFCA is also applied on global mean surface air temperature to compare the relative changes to the increase in temperature and to estimate resulting exponential scaling rates.

The previously discovered intensification and poleward shift of AR tracks under climate change could be confirmed in this study with a different AR detection algorithm. A test of the methods to detect differences between AR and non-AR events on integrated water-vapor transport (IVT) shows potential, as it successfully separated AR-associated IVT extremes from non-AR extremes and resulted in the expected faster scaling of AR-IVT from previous studies. The faster scaling of AR extremes in precipitation data is estimated in all models while a large inter-model spread concerning the size of the differences made results insignificant.

This thesis first introduces aspects of theoretical meteorology in chapter 2 to explain the dynamics in which atmospheric rivers are embedded in, followed by a structural introduction of atmospheric rivers. An overview is given for the structure and typical conventions of general circulation models to strengthen the understanding of often used terms in climate analysis studies. Thereafter, in chapter 3 the criteria for the selected climate models are discussed, along with the obtained datasets. Here, the applied metrics and methods to detect atmospheric rivers and calculate changes of AR and non-AR associated extreme precipitation events are also presented. In chapter 4 the results of a resolution comparison, possible differences in future AR metrics, the identified climate change signal and the scaling of relative changes with increasing temperature are displayed, followed by their interpretation and discussion of methods in chapter 5. Lastly, a short conclusion is given in chapter 6, followed by the list of all used references and a declaration of originality.

Chapter 2

Theory and Background

Before introducing the methods and data sources used, it can be helpful to investigate a thermodynamical approach on our atmosphere and derive explanations for known phenomena, whose comprehension will be assumed later. For this work, a motivation for the general global movement of surface air is especially important, since atmospheric rivers are embedded in them. A short introduction into precipitation extremes and atmospheric rivers is given, followed by the general structure and use of climate models along with often used conventions in the climate analysis community.

2.1 Theoretical Meteorology

This section tries to motivate large movement patterns and dynamics of surface air, as well as the global distribution of atmospheric moisture. In addition, the classification and interpretation of variable values shall be improved by comparing them to known phenomena.

2.1.1 The Climate System and Global Warming

The Atmosphere is a large-scale thermodynamical system, governed by thermodynamical and dynamical equations which are described here to gain a deeper understanding of occurring weather events, global gradients, major air flows and their key driving factors. The reasoning in this chapter closely follows the textbook from Dieter Etling (Etling 2008), which is recommended for more detailed descriptions and additional information. Topics are here consolidated by their importance to understand later used data and effects and by their link to atmospheric river dynamics.

In general one differentiates between closed systems, where only energy is exchanged with the environment and open systems, where additionally particles exchange is possible. The state Z of a system is described as $Z = f(p, V, T)$, with pressure p, volume V and temperature T. The Atmosphere is typically described as closed systems of air packages with exceptions only for specific problems like the formation of clouds, where mass exchange is necessary.

Dry air in the atmosphere can be described with the ideal gas equation

$$pV = mRT, \tag{2.1}$$

where m is the mass and R is the specific gas constant. The atmosphere consists of 78.110 % N_2 (nitrogen), 20.952 % O_2 (oxygen), 0.934 % Ar (argon) and additional neglected substances ($\approx 0.003\,\%$) with minor shares like carbon dioxide CO_2 or methane CH_4. These gases with partial masses m_i can all be described separately as ideal gases and combined with Dalton's Law to

$$p_l V = \left(\sum_i m_i R_i \right) T = m R_l T, \tag{2.2}$$

where $R_l = \sum_i m_i R_i / m_l$ is the effective gas constant of dry air with a total mass m_l and pressure p_l. The Dalton Law states that the total pressure and volume are the sums of their partial pressures and volumes. In addition to these "dry" gases, water vapor plays a significant role in the atmosphere and can also be well approximated as ideal gas with a specific gas constant of $R_w = R_l/\epsilon$. Here R_w is the effective gas constant of water vapor and $\epsilon = 0.622$ an often occurring factor. The partial pressure of water vapor is commonly labeled e, which gives

$$eV = R_l T/\epsilon. \tag{2.3}$$

The mass share of water vapor m_w to total mass m is called specific humidity $q = m_w/m \approx m_w/m_l$, but difficult to measure directly. Therefore one often uses

$$\frac{e}{p-e} = \frac{m_w R_w}{m_l R_l} \approx \frac{q}{\epsilon}, \tag{2.4}$$

with the easier measurable partial pressure of water vapor e and total pressure $p = p_l + e$. Dry air cannot contain arbitrary amounts of water vapor, but only partial pressures e up to a saturation pressure $e \leq E$. A temperature relation of this saturation $E(T)$ has been discovered in the early 18th century with empirical measurements from H. G. Magnus leading to the estimation

$$E(T) = 6.1 \cdot 10^{\frac{7.45 \cdot T/^\circ\mathrm{C}}{235+T/^\circ\mathrm{C}}-2}. \tag{2.5}$$

As a comparison $E(0\,^\circ\mathrm{C}) = 6.1\,\mathrm{hPa}$ and $E(35\,^\circ\mathrm{C}) = 56.4\,\mathrm{hPa}$, with $35\,^\circ\mathrm{C}$ hardly ever reached above oceans where saturation is close to its maximum. The partial pressure of water vapor therefore accounts for at most $5\,\%$ of air pressure at sea level. The temperature dependent relationship of saturation pressure can also be derived from the Clausius-Clapeyron equation, which yields similar results as the empirical equation for conditions in the real atmosphere with aberrations of $0.1\,\%$ to $0.5\,\%$ for $T = 30\,^\circ\mathrm{C}$ and increasing with larger temperatures. A closer investigation of implications from the Clausius-Clapeyron equation for the amount of water vapor in the atmosphere is done in subsection 2.1.3.

Heat transfer between the air packages occurs in both horizontal (x, y) and vertical direction (z), but can here be limited to the vertical direction for simplicity. The total energy is

$$\mathrm{d}E = -p\mathrm{dV} + \delta Q, \tag{2.6}$$

with the work of/at the system $-p\mathrm{d}V$ and the net heat exchange δQ. The energy fluxes participating in the energy balance of the state of the system are the molar heat conduction $\dot{W} = -\lambda \mathrm{d}T/\mathrm{d}t$, convection, short-wave solar fluxes $\dot{S}_s$ and long-wave black body radiation S_l. Here λ is the molecular thermal conductivity and long-wave radiation is approximately governed by the Stefan-Boltzmann Law

$$\dot{S}_l = \sigma T^4. \tag{2.7}$$

The first principal of thermodynamics can be re-written as

$$c_p \frac{\mathrm{d}T}{\mathrm{d}t} - \frac{1}{\rho}\frac{\mathrm{d}p}{\mathrm{d}t} = -\frac{1}{\rho}\frac{\mathrm{d}\dot{Q}}{\mathrm{d}z} = -\frac{1}{\rho}\left\{\frac{\mathrm{d}\dot{S}_l}{\mathrm{d}z} + \frac{\mathrm{d}\dot{S}_s}{\mathrm{d}z} + \frac{\mathrm{d}\dot{W}}{\mathrm{d}z}\right\}. \tag{2.8}$$

Here c_p is the specific heat storage capacity at constant pressure, ρ the density of the atmosphere and $\dot{Q}$ the energy flux density. Short-wave radiation from the sun is absorbed to $\approx 70\,\%$ at the surface. The generated heat at the surface is then vertically transported into higher layers of the atmosphere over the day by molar heat conduction and convection. With the assumption, that all absorbed heat at the surface is transported to the atmosphere up to a height H, it follows for small heights ($p \approx \mathit{const.}$)

$$\frac{\mathrm{d}T}{\mathrm{d}t} = +\frac{1}{\rho c_p}\frac{\dot{W}_0}{H} \tag{2.9}$$

and therefore an increase of temperature over time with $\mathrm{d}T/\mathrm{d}t \approx 6.9\,\mathrm{K\,h^{-1}}$ for $H = 100\,\mathrm{m}$. This is of course only a rough estimate for mid-day conditions without air currents at the ground, but shows the origin of strong daily air temperature fluctuations in the lower atmosphere. The vertical motion of a heated air package can then lead to a complicated process of condensation and cloud formation. Over night, the solar short-wave component vanishes from the balance, while the long-wave emission continues. This cools the surface, stops the vertical heat transport into the atmosphere and resets the daily cycle.

Lets now have a look at the total energy balance of the system earth. The earth surface itself radiates long-wave radiation approximately like a black body with $S_l \sim \sigma T^4$ and absorbs short-wave radiation from the sun $S_s = \pi R^2 S_0 (1-\alpha)$, with the solar constant S_0. The albedo α accounts for reflection on the earth surface and gases in the atmosphere. The atmosphere can also emit and absorb long-wave radiation like a black body and radiates isotropic long-waves, mostly due to clouds (water vapor), CO_2 and O_3. The share of atmospheric radiation directed back to the earth is called back-radiation (S_{BR}) and contributes to the total energy balance

$$\frac{S_0}{4\pi(1-\alpha)} = \sigma T^4 - S_{BR}. \tag{2.10}$$

The radiation and scattering of long-wave radiation in the atmosphere has a significant effect on the equilibrium temperature T_m and is called greenhouse-effect. Inserting known constants yields a global mean surface temperature of $T_m = 15\,^\circ\mathrm{C}$, which aligns well with observations. The back-radiation is roughly proportional to the total mass of contributing gases and their action on long-wave radiation. The anthropogenic addition of the vary gases leads to an additional increase of the back-radiation, which is therefore called anthropogenic greenhouse-effect. Over time the equilibrium temperature adjusts, which is called climate change.

To achieve more precise estimates of the global mean temperature T_m, additional more complex relations have to be considered, like the increase of water vapor, which leads to more frequent cloud formation and a higher albedo. This would decreases the greenhouse-effect, while the melting of strongly reflective ice shields due to the higher temperature increases it. The future amount of anthropogenic added greenhouse-gases is unknown and can take many different pathways. This opens the questions of which pathways to use when estimating future climate projections, which is regarded at the end of this chapter.

2.1.2 Global Motion Patterns in the Atmosphere

This section derives large-scale air currents, emerging from regionally dependent solar energy absorption and largely follows the textbook of Dieter Etling (Etling 2008). The aim is to understand the mechanisms causing global horizontal and vertical movements of surface air.

In the previous chapter, the system earth was described as homogeneous to evaluate energy input and output as global averages and estimate an equilibrium temperature. However, in reality there is a positive energy flux at the equator and a net negative at the poles. Gradients of temperature and pressure lead to complex dynamics in the atmosphere, which are important for the formation of atmospheric rivers and shortly motivated here.

First of all, the hydrostatic vertical pressure gradient is investigated. Due to gravitation, the pressure on a package of air is given by

$$p(z) = \frac{m(z)g}{F}, \tag{2.11}$$

with the mass m of the package, the gravity of earth g and the area below the package F. The real atmosphere can be approximated by two different ways. The first assumes constant temperature $T(z) = T_0$ and is therefore called isothermal atmosphere, which results from additionally using the mass $m(z) = \rho(z)Fz$ in

$$\frac{\partial p(z)}{\partial z} = -g\rho(z) = -\frac{gp}{RT} \quad \Rightarrow \quad p(z) = p_0 \exp\left(-\frac{gz}{RT_0}\right). \tag{2.12}$$

Here $p(0) = p_0$ is the maximum pressure at the surface. The second approach is the linear change of temperature $T(z) = T_0 - \gamma z$, with the constant slope γ. It follows the polytropic atmosphere

$$p(z) = p_o \left(\frac{T_0 - \gamma z}{T_0}\right)^{\frac{g}{\gamma R}}. \tag{2.13}$$

For conditions at mid-latitudes ($\phi \approx 45°$), both of these solutions are combined to best describe the real atmosphere with a constant temperature increase $\gamma = 65 \times 10^{-4}\,\mathrm{K\,m^{-1}}$ in the troposphere for heights

$z < 10\,\mathrm{km}$. Above a fixed temperature ($\gamma = 0$) follows in the stratosphere for heights $10\,\mathrm{km} < z < 20\,\mathrm{km}$ and a linear increase in temperature with $\gamma = 1 \times 10^{-3}\,\mathrm{K\,m^{-1}}$ above. The resulting trend is shown in Figure 2.1, which also shows the separation of the atmosphere into the lower troposphere and the higher stratosphere with the tropopause dividing it. It can therefore be recorded for the troposphere, that pressure and temperature decrease with height.

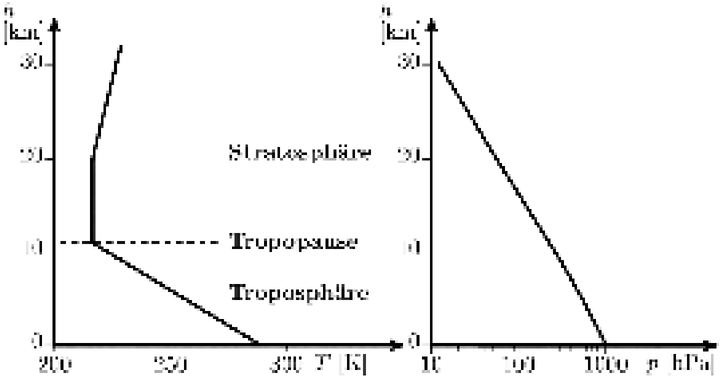

Figure 2.1: Temperature and pressure for different vertical heights z in the mid-latitude approximation. Polytropic and isothermal atmospheres are stepwise combined with a first switch at the tropopause, which marks the transition of the troposphere ("Troposphäre") to the stratosphere ("Stratosphäre"). Figure extracted from Etling 2008.

Now that the vertical pressure gradient is established, the motion of horizontal currents under rotations are investigated. A key driving factor for motion change in the atmosphere is the Coriolis-Force F_C. The earth rotates around its own axis with $\Omega = 2\pi/24\,\mathrm{h}$, which acts on a acceleration-free motion in an inertial reference frame as

$$\frac{\mathrm{d}\mathbf{v}}{\mathrm{d}t} = -2\boldsymbol{\Omega} \times \mathbf{v} - \boldsymbol{\Omega} \times \boldsymbol{\Omega} \times \mathbf{r} \tag{2.14}$$

in a rotating reference frame. The first term corresponds to the Coriolis and the second term to the Centrifugal acceleration. Here $\mathbf{r}$ is the positional radius vector and $\mathbf{v}$ the velocity. Consider an inertial observer outside the atmosphere. A wind starting at the equator and moving toward the North Pole initially has an eastward velocity equal to Earths rotational velocity at the equator. For an observer on the surface, the wind therefore initially appears to move only northward. As the air moves poleward, it approaches Earths rotational axis, where the eastward velocity of the surface and surrounding air is smaller. The wind however, conserves its original eastward velocity which is now larger than that of the underlying surface. As a result, the wind appears to deflect to the right. It follows more generally that the direction of motion in the northern hemisphere deflects to the right, while in the southern hemisphere it deflects to the left. The magnitude of the wind velocity stays unchanged.

In a tangential plane at the surface of the earth, the rotation frequency can be split into

$$f = 2\boldsymbol{\Omega}\sin(\phi) \quad \text{and} \quad f^* = 2\boldsymbol{\Omega}\cos(\phi), \tag{2.15}$$

which are called Coriolis Parameters and dependent on the latitude ϕ. The equation of motion follows as

$$\frac{\mathrm{d}\mathbf{v}}{\mathrm{d}t} + 2\boldsymbol{\Omega} \times \mathbf{v} = -\nabla\Phi - \frac{1}{\rho}\nabla p. \tag{2.16}$$

Here $\nabla_i = \partial/\partial x_i$ is the Nabla operator, ρ the density, p the pressure and $\Phi = gz$ the geopotential.

As an example for an important air current relationship with pressure gradients, assume a friction-free horizontal and stationary current $\mathbf{v}_g$ ($\mathrm{d}\mathbf{v}_g/\mathrm{d}t = 0$), then the equation of motion from above simplifies with the equilibrium between Coriolis-Force and pressure gradient to

$$\mathbf{v}_g = \frac{1}{gf} e_z \times \nabla p, \tag{2.17}$$

where e_z is the vertical unit vector. The resulting air current is called geostrophic wind $\mathbf{v}_g$. This shows, that currents produced by horizontal pressure gradients flow along isobaric trajectories when the equilibrium between Coriolis-Force and pressure gradient is reached. Because the Coriolis parameter f diminishes towards the equator, the absolute velocity increases. The assumption of equilibrium falls close to the equator but gives good estimations at mid-latitudes.

The change of the geostrophic wind with pressure defines barotropic $\partial \mathbf{v}_g / \partial p = 0$ and baroklinic $\partial \mathbf{v}_g / \partial p \neq 0$ conditions, which is of importance for the emergence of cyclones, but not further analyzed here. With an additional temperature gradient, the geostrophic wind changes magnitude in vertical direction by

$$\frac{\partial \mathbf{v}_g}{\partial z} = \frac{g}{fT} e_z \times \nabla T. \tag{2.18}$$

This relation follows from the statical equation of motion (Equation 2.16) in a rotation reference frame and the ideal gas equation (Equation 2.1). Additionally, to understand the deviation of our example air current, we have to consider the total torsional moment of the atmosphere is preserved, which implies the total vorticity $\eta = \zeta + f$ is also preserved. Here ζ is the relative vorticity, where the Coriolis parameter f must be added to account for the rotating reference frame. Lets look again at the friction-free horizontal and stationary geostrophic wind resulting from pressure gradients as described above. A current in positive zonal direction (from west to east) with a small disturbance in positive meridional direction (from north to south) slowly changes latitude position with changing Coriolis Parameter f. To keep the total vorticity preserved, the current needs a reversed curvature, which changes the wind direction to point back to its original position. When crossing the initial latitude, the effect reverses with an opposite curvature. This results in a pendulum motion of the current, which can be observed on a large scale and is called Rossby-waves after Carl-Gustaf Rossby.

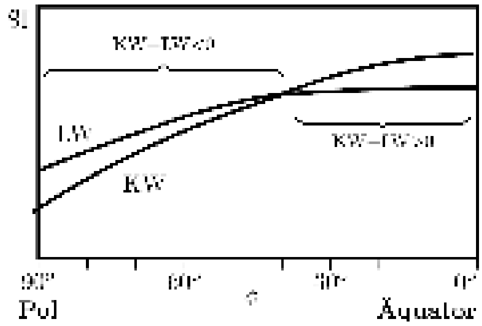

Figure 2.2: Schematic energy balance of the earth for different latitudes ϕ between equator ("Äquator") and pole ("Pol"). The absorbed short-wave radiation (KW) from the sun and the emitted long-wave black body radiation (LW) are largest at the equator, but follow different relations. The resulting net heat amount is positive at the equator and negative at the poles. Figure extracted from Etling 2008.

Finally, having introduced the origins of smaller dynamical movement we return to the global scheme and the temperature gradient between equator and poles. It has already been made clear, that the net heat input on the surface is passed on to the atmosphere and determines the temperature of the vertical air column above. The total energy stays in equilibrium. However, the incoming solar flux is largest per unit area on the equator, because the inclination to the radiation is zero, while the inclination increases towards 90° at the poles. The energy input is therefore larger at the equator. On the other hand, the larger energy input leads to higher temperatures and hence to more long-wave black-body radiation due to the temperature dependency $\sim T^4$. While these effects cancel globally, they exhibit different latitudinal dependencies as sketched in Figure 2.2. An initial homogeneous planet heats up quicker at the equator because of the larger directly radiated area. The increased temperature does increase equatorial black body radiation, but not enough to make up for all incoming energy. This regional difference leads to a net positive heat flux at the equator and net negative heat flux at the poles, if a static atmosphere and no energy transport is assumed. The equilibrium is at around $\pm 40°$ latitude.

The heat flux difference must therefore constantly be settled by transporting heat in the atmosphere from the equator to the poles. A portion of the heat is also transported in the ocean, but can be neglected here. How can the energy difference be equalized? First of all, lets assume a atmosphere with no horizontal temperature or pressure gradients across all latitudes. The net heat flux difference would then cause an increase in temperature at the poles, which leads to a vertical rise of air and low-pressure regions at the surface. At the poles the temperature decreases with descending air and high pressure regions at the surface. The pressure gradient would then create an air flow from the equator to the poles above the tropopause at 12 km to 15 km, and a reverse flow from the pole to the equator in the lower atmosphere due to continuity. This formation of vertical circulation is called Hadley Cell after their discovery in 1735 by George Hadley and could transport warm air from the equator to the poles and therefore transport heat in the form of internal energy. However, while moving poleward the air masses are compressed, because the meridians crowd together. To express it in numbers: the distance of 1° separated meridians is 111 km at the equator and only 96 km at $\phi = 30^\circ$. The higher density currents evade standing air downwards, which leads to the collapse of the first Hadley Cell. The forced descend of these air masses leads to an increase in temperature due to Equation 2.1 and to stable high pressure regions at the very latitude of 30°.

It has already been shown that horizontal currents on the earth are deflected by the Coriolis Force. This also applies to the currents inside the Hadley Cell and results in an additional eastward wind component in the higher and a westward component in the lower atmosphere (on both hemispheres). This deflection drastically decreases the effectiveness of the very heat transport it was created by. For conditions and temperature gradients on the earth, the remaining circulation is not able to produce the heat transport needed to balance the equator-pole difference.

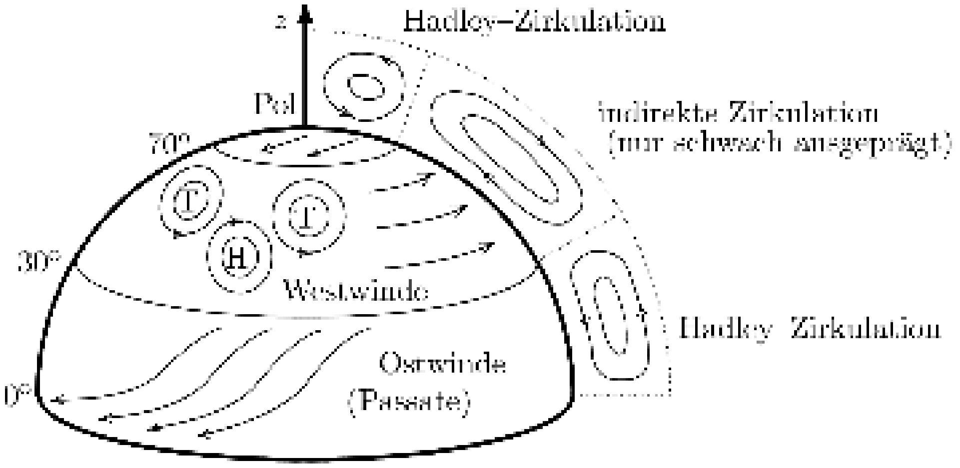

Figure 2.3: Sketch of the near-surface air currents in the northern hemisphere. In latitudes below 30°, the air moves westwards and slightly to the equator. This is a consequence from continuity of the north-eastward wind at higher atmospheric levels. The first Hadley Cell ("Hadley-Zirkulation") collapses at 30°N with resulting stable high- and low-pressure regions and pole/eastward trade winds. Close to the pole a second Hadley Cell exists. Here surface-near air again moves opposite to the winds at larger heights. These dynamics ensure constant transport of heat from the equator to the poles. Figure extracted from Etling 2008.

Moreover, the high temperature and pressure gradient in mid-latitudes leads to baroclinic instability ($\nabla\rho \times \nabla p \neq 0$). Ergo planes of constant temperature and pressure are not parallel. Currents of air are therefore not of equal velocity as discussed above and shown in Equation 2.18, which leads to the formation of cyclones and jets. These largely carry the remaining heat and level the equator-pole temperature gradient.

The resulting dynamics and motions are a result of the collapse of the mid-latitude Hadley Cell. The total tropospheric motion from equator-pole heat transport on near surface air is sketched in Figure 2.3 for the northern hemisphere. It shows the equatorial Hadley Cell and resulting surface winds in west-equator direction. Another stable Hadley like circulation occurs at the poles with alike west-equatorial winds at the surface (this is commonly called Polar Cell). Friction at the boundary of the mid-latitude regime leads to a weaker indirect anti-circulation cell with north-east winds at the surface and the occurrence of complex dynamics and mostly stable high- and low-pressure regions. These stable surface winds are commonly referred to as trade winds.

2.1.3 Atmospheric Moisture and the Hydrological Cycle

For atmospheric rivers as well as precipitation the two aspects of air dynamics and water vapor are crucial. Having investigated the dynamics in the previous paragraphs, we will now focus on the moisture creation, its impacts and its global distribution. Water vapor makes up only an extremely small portion of the planetary water. When liquefied, atmospheric water would form a layer of 25 mm, with oceans of multiple thousand meters deepness (Peixóto and Oort 1984). Nevertheless, water vapor has a significant impact on global weather and climate because it serves as an important greenhouse gas, as mentioned earlier. Water vapor is found exceedingly at the equator and above oceans, while air above deserts and mountain ranges remain rather dry (Peixóto and Oort 1984).

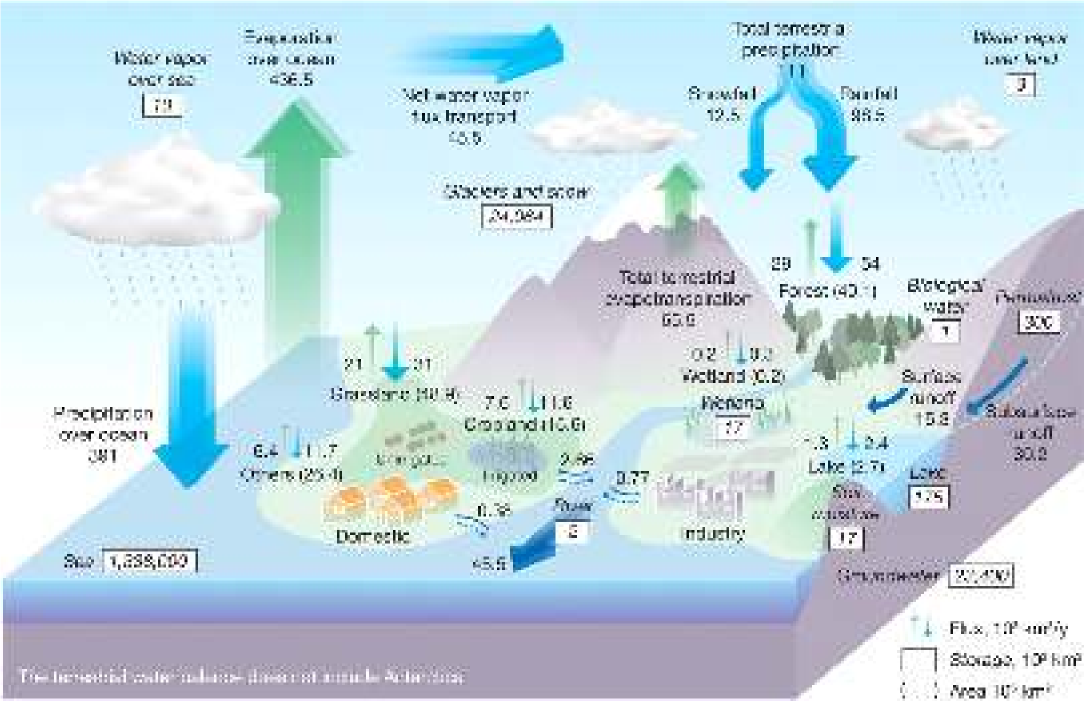

Figure 2.4: A sketch of the hydrological cycle in- and outputs with water vapor fluxes into the atmosphere in green and fluxes out of the atmosphere in blue. Global fluxes and contribution areas are separated into ocean and terrestrial components. Values in white boxes show the water storage amount for different subsystems. Figure extracted from Oki and Kanae 2006.

The hydrological cycle, displayed in Figure 2.4 describes the continuous process of water being moved from the surface to atmosphere by evaporation and its return by precipitation. Evaporation and precipitation are both quantities which are difficult to measure precisely at a global scale. For evaporation, the created water vapor impacts the local surrounding air strongly, which makes measurements difficult. For precipitation observations on land, rough topography requires high observation density and the needed large-scale measurements on the open sea for global estimate are difficult due to the size of the oceans (Peixóto and Oort 1984).

With the total water vapor in the atmosphere measured to be about 25 mm, the annual mean global precipitation and evaporation are estimated at roughly 1000 $\mathrm{mm\,yr^{-1}}$, which results in a cycle period of about 9 days (Peixóto and Oort 1984). Most of the water vapor is located in the troposphere and concentrated at the surface and the equator. The specific humidity decreases slowly towards the poles and quickly in vertical direction, which is displayed in Figure 2.5a. Most evaporation and therefore input in the hydrological cycle is observed over oceans between 10° and 30° latitude on both hemispheres. While strong precipitation occurs mostly around the equator, some water vapor is transported in the mid-latitudes where precipitation dominates over evaporation (Peixóto and Oort 1984). A vertical cross-section of observed water fluxes can be seen in Figure 2.5b.

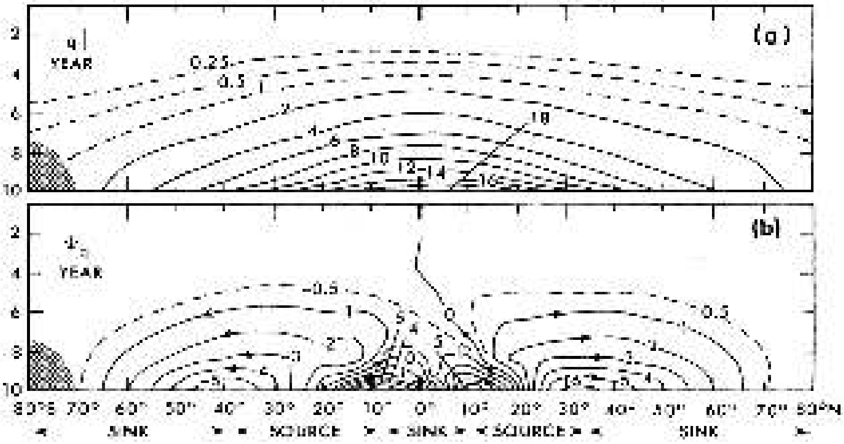

Figure 2.5: Annual mean distributions across latitudes for a) the specific humidity and b) the atmospheric water flux proportional to the later defined IVT. Figure extracted from Peixóto and Oort 1984.

A useful metric to describe the atmospheric water transport is the integrated water vapor transport (IVT)

$$IVT_u = -\frac{1}{g} \int_{p_1}^{p_2} u(p) \cdot q(p) \, \mathrm{d}p, \tag{2.19}$$

$$IVT_v = -\frac{1}{g} \int_{p_1}^{p_2} v(p) \cdot q(p) \, \mathrm{d}p, \tag{2.20}$$

$$IVT = \sqrt{IVT_u^2 + IVT_v^2}, \tag{2.21}$$

with pressures $p_1 > p_2$, the specific humidity q and the meridional and zonal wind u, v, respectively. This includes both amount and speed of the vapor transport. Earth's gravitational constant g is used to express the resulting field as a flux (kg/ms), while the pressure integration includes all lower height levels. Negative signs are convention to obtain positive values for north/east-directed transport. A simulated map of global IVT can be seen in Figure 2.6. Here the westward wind in the equatorial Hadley Cells and the north-eastward wind in the mid-latitudes can also be seen, which are described in the previous paragraph, while known locations of mountain ranges and other topography also shows the size of deviations from this earlier simplistic derivation. Three bands of high water vapor transport can be identified: one at the equator and two in the mid-latitudes of each hemisphere at roughly ±40°N.

The amount of water vapor in the atmosphere increases due to the higher temperatures caused by climate change. As discussed previously for water vapor saturation pressure, the temperature-pressure relationship is derived from the Clausius-Clapeyron equation (Nolting 2016)

$$\frac{\mathrm{d}p}{\mathrm{d}T} = \frac{Q_m}{v_g - v_l}, \tag{2.22}$$

describing equilibrium states between gaseous and liquid phases. Here p denotes pressure, T temperature, Q_m the molar heat of evaporation (i.e., the latent heat) and v_g, v_l the molar volume of gas and liquid, respectively. With $v_g \approx \frac{RT}{p}$ from the ideal gas equation (Equation 2.1), $v_l << v_g$ due to the significantly higher density of liquids compared to gases and neglected compressibility, the equation can be simplified to

$$\frac{1}{p}\frac{\mathrm{d}p}{\mathrm{d}T} = \frac{Q_m}{RT^2}. \tag{2.23}$$

This differential equation can be solved by separation of variables and results in

$$p/p_0 = e^{\frac{Q_m}{R}\left[\frac{1}{T_0} - \frac{1}{T}\right]}, \tag{2.24}$$

with a reference temperature T_0 and a starting pressure $p(T_0) \equiv p_0$. Using a rough estimate of historical global mean surface-air temperature $T \approx 287.2\,\mathrm{K}$ (14.2 °C), the gas constant R and a molar latent heat of $Q_m = 4.4 \times 10^4$ J/mol, the vapor pressure changes with 6.4 %/K. Considering varying mean temperatures across latitudes and heights, the relative vapor pressure change ranges from 6 %/K to 7 %/K (Boer 1993).

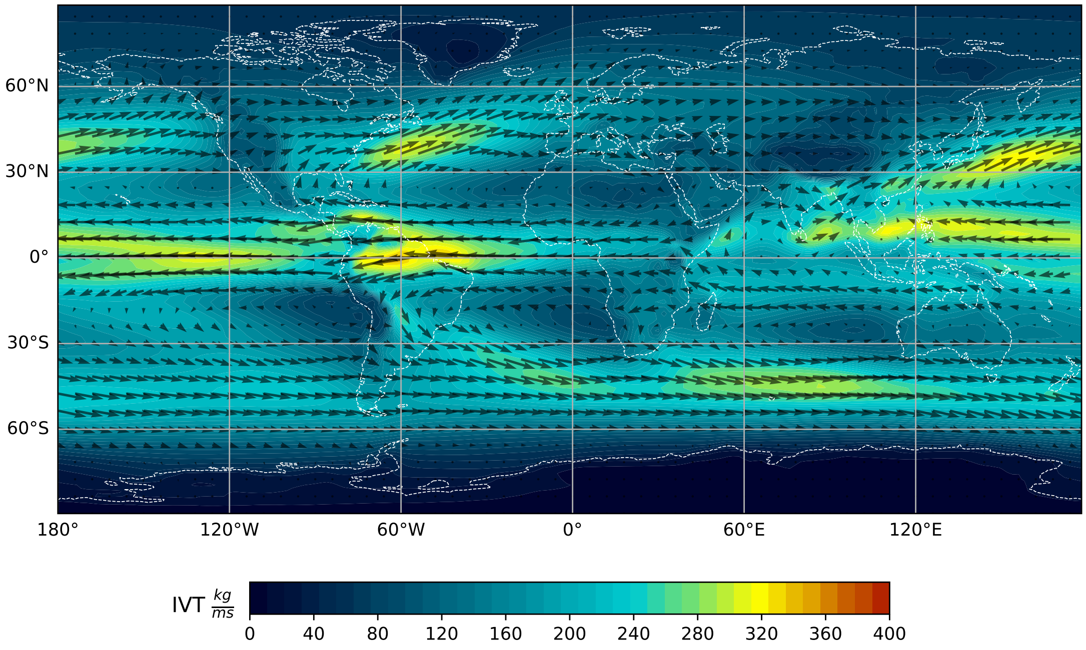

Figure 2.6: Global integrated water-vapor transport (IVT) with streamline arrows indicating direction and color indicating magnitude. This is not an observation, but the ensemble mean simulation of four general circulation models from Table 3.1 for a future scenario (ssp585). The data source, interpretation and IVT calculation will be discussed in chapter 3. That said, contemporary IVT fields are merely smaller in magnitude, but otherwise follow the same patterns.

The saturated specific humidity q_e is approximately proportional to the saturation vapor pressure p_e in the troposphere and therefore the same exponential scaling is expected. Since specific humidity values q above oceans are close to saturation q_e (Allen and Ingram 2002), this directly transfers to IVT values.

Intensity of extreme precipitation events ($px1$, as defined in subsection 3.2.2) occurs when nearly all available air moisture is rained down and therefore expected to scale with the same rate. The scaling of frequency of extreme precipitation events (fx; as defined in subsection 3.2.2) differs and was assessed in the work of Kotz et al. 2023 to 16.7 %/K by scaling up daily data of the historical period with 7 %/K and calculating the exceedance of the original 99th percentile threshold. This estimate is not repeated in this work due to time constraints. These scaling rates are later used as comparison and validation of the results.

2.2 Precipitation Extremes: Intensity, Frequency, and Scaling

Here, extreme precipitation events are introduced with their typical definition methods in literature. Furthermore, their typical temporal and spatial extent is discussed, as well as dynamical and climate change impacts and their formation reasons.

General circulation models still display low consistency in the projection of precipitation and extreme events as response to anthropogenic forcing, largely because of different sub-gird processes parameterizations like convection and cloud microphysics. As a result, future projections - especially of extreme events - are subject to large uncertainties, because underlying mechanisms are represented differently across models and may respond differently under radiative forcing (Gimeno, Sorí, et al. 2022).

Extremes can be defined by either looking at the caused impacts (social effects, economical losses, etc.), or by looking at the statistics of all events. In climate sciences, the second approach is usually taken with some statistical measure of rareness of the events (Gimeno, Sorí, et al. 2022). Additionally compound events can also take an important role in extreme impacts, even though they consist of multiple usual events that only acted in an extreme way by occurring together. Many metrics exist and are used to define extremes, with absolute thresholds like precipitation events above 10 mm or relative thresholds like events above the 99th percentile of some distribution. For frequency typical approaches are metrics like the annual count of days, where precipitation surpasses 10 mm, or the 99th percentile. While the first absolute threshold kind is better suited to evaluate the total damage, the second allows for better regional comparison (Gimeno, Sorí, et al. 2022). In the latter case, the sensitivity of results to the threshold selection can play a major role. In both cases one has to be careful not to misinterpret the results and choose good thresholds. It is also possible to use parametrized methods, like fitting extreme value distributions to the ensemble of events to gain a threshold. While archiving higher accuracy in some cases, the need of large datasets to apply the extreme value distribution and the sensitivity on fitting functions and parametrization methods limit their usefulness (Gimeno, Sorí, et al. 2022). As of now, the climate science community has gained no consent on which method to use in which cases.

The spatial extent of extreme precipitation events was analyzed in Matte, Christensen, and Ozturk 2021 on ERA5 data with 30 km resolution and found an average size of $\approx 65 \times 10^3\,\mathrm{km}^2$ for the 99th percentile core of precipitation events. Independent of their size, they showed daily intensity of $\approx 40\,\mathrm{mm}$. The size of all events increased under global warming with roughly 20 % for 3 °C warming. The intensity increased by the same factor for small events, while the intensity of larger sized extremes increased slower (Matte, Christensen, and Ozturk 2021). Extreme events can either be the result of continuous precipitation over the day, or short and intense with durations $< 1\,\mathrm{h}$ and can not be distinguished in most cases.

The occurrence of extreme precipitation events are linked to different atmospheric mechanisms. Close to the tropics, the cyclones are responsible for many extreme events, while globally the most dominant moisture transport causes are atmospheric rivers and low-level jets. They also contribute the strongest to global water vapor transport and are crucial for keeping the hydrological cycle intact (Gimeno, Sorí, et al. 2022).

Climate change impacts the available moisture in the atmosphere and thereby the hydrological cycle. The effect of warmer global temperatures on global mean precipitation is estimated by general circulation models to scale with 1 %/K to 3 %/K, which falls considerably below the expected 7 %/K from Clausius-Clapeyron. The observed increase in mean precipitation also falls below the expectations, with yet unclear reason. Extreme events are however not governed by the global energy balance, but subject to more complex regionally different dynamics and may increase significantly stronger - especially for heavy events of short duration (Gimeno, Sorí, et al. 2022).

While both intensity and frequency of extreme precipitation increases, the effect on frequencies is much stronger. A consent exists that extreme events are expected to follow the prediction from Clausius-Clapeyron (Gimeno, Sorí, et al. 2022). One generally differentiates between thermodynamical changes, like the increase of humidity due to Clausius-Clapeyron and dynamical changes. The latter can typically not be approximated by simple formulas. A possible dynamic example on climate change impacts could be an increased circulation speed of the hydrological cycle, or the increase of weather event speeds due to the increased internal energy of the atmosphere. A difference in contribution of thermodynamical and dynamical changes on extreme precipitation has been observed in Gimeno, Sorí, et al. 2022, with domination of the first in mid-latitude regions and domination of the latter in the tropics.

2.3 Atmospheric Rivers: Physical Definition and Relevance

This section introduces atmospheric rivers, their importance in the hydrological cycle in mid-latitude regions and the current understanding of their formation.

Atmospheric rivers (ARs) are small conduits in the troposphere that transport water vapor with similar amounts to the worlds largest rivers. An AR is typically identified as a long elongated shape of high water vapor flux with more than 2000 km in length and about 500 km in width. An example is shown in Figure 1.1 from satellite images with true colors and in Figure 2.7 with highlighted water vapor. In contrast to real rivers, they are not stationary in time or space, but occurrences that emerge over large water basins, travel around the globe and terminate by making landfall. At any time, there are roughly 4 to 5 separate ARs present somewhere on the globe with average lifetimes of 20 h (Gimeno, Nieto, et al. 2014).

The structure and trajectory of an AR is usually governed by a sharp horizontal temperature gradient. ARs live inside the warm conveyor belts next to the cold front left by cyclones and low-level jets. Four conditions are usually met for ARs: 1) It includes large amounts of moisture in the lower troposphere which bundles against the cold side of the temperature gradient 2) a low-level jet flows in front of the

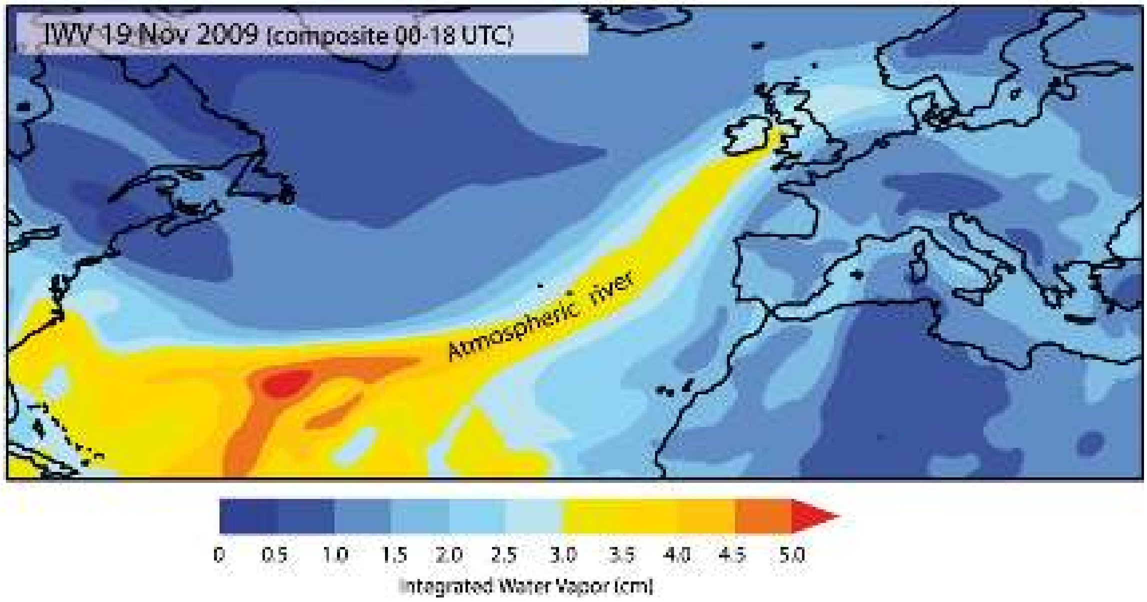

Figure 2.7: Visualization of an atmospheric river by color coding the vertically integrated water vapor (IWV). The AR stretches over most of the North Atlantic up to the British Isles on the 19. November 2009. Figure extracted from Gimeno, Nieto, et al. 2014.

cold-front due to the thermal wind relation (s. Equation 2.18), 3) a stable vertical layering of temperature on the AR side and 4) a low, dry area in front of the AR (Gimeno, Nieto, et al. 2014). The moisture originates from either converging the remaining humidity of previously passed cyclones or directly from the tropics. A vertical cross section is displayed in Figure 2.8, showing gradient levels of wind speed, humidity and moisture flux.

In mid-latitudes ARs contribute with $< 90\,\%$ to the total meridional water vapor transport, which makes them a crucial key for the hydrological cycle and for life on higher latitudes. The most common reason for ARs to terminate is orographic lifting, ergo the forced vertical rise due to the topography beneath them. Up to 30 % of all precipitation in the western USA and Europe originates from ARs (Gimeno, Nieto, et al. 2014). While being an important source of fresh water in many regions and ending many droughts, the large amounts of moisture concentrated on small spatial scales can lead to strong precipitation events with disastrous consequences. The hazardous effects of ARs were investigated in Paltan et al. 2017, who found up to 80 % of floods are caused by ARs while their absent causes 90 % of droughts.

When ARs make landfall, the continuous replenishment of moisture due to the high wind speeds can strengthen the intensity and duration of precipitation events drastically. This can often result in soil incapable of soaking up or rivers incapable of distributing the large water amounts fast enough. The link between ARs and extreme precipitation events has been studied in many cases (Jeon et al. 2015; Michel et al. 2021; Mukherjee and Mishra 2021; David A Lavers et al. 2013). Especially in westward oriented coastal regions, AR cause most extreme precipitation events, while climate change may have a strengthening effect on this link (Whan et al. 2020).

As discussed in the chapter about the hydrological cycle, most water vapor is created in the tropics, while only a small portion is transported into mid-latitudes. Here ARs play the dominant transportation mechanism. The region of AR occurrences begins with the collapse of the equatorial Hadley Cell and stretches over the mid-latitudes up to the poles. This is the region where complex atmospheric dynamics are needed for the equator-pole heat transport, with ARs being one of them. Since moisture is concentrated close to the ground the atmospheric motions in the lower troposphere govern the movement of ARs. The surface near air currents in mid-latitudes move poleward with an eastward contribution due to the Coriolis force. This is therefore is also the general trajectory of most atmospheric rivers. ARs not only utilize the tropical moisture, but also water vapor created in the mid-latitudes (Gimeno, Nieto, et al. 2014). They therefore emerge mostly above large water basins, move to the north-east until elevated topography forces their vertical rise and they make landfall.

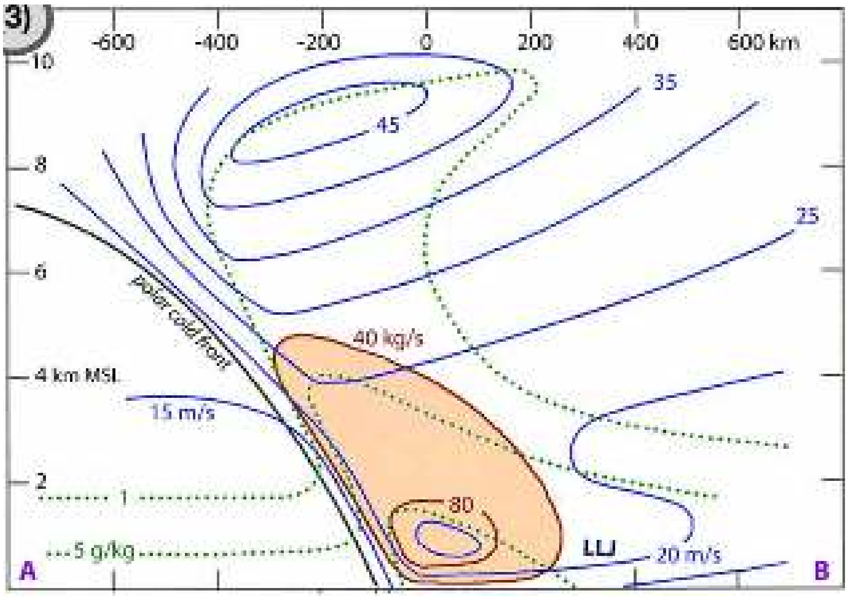

Figure 2.8: Vertical cross-section of an atmospheric river with a sharp temperature gradient shown as a black line (polar cold front), levels of constant specific humidity as dotted green lines, moisture flux in shaded orange and the levels of constant wind speeds as blue lines. Figure extracted from Gimeno, Nieto, et al. 2014.

2.4 Climate Projections and Emission Scenarios (SSPs)

General circulation models (GCMs) - sometimes also named global climate models - are the groundwork for large climate analyses. They divide the earth into evenly spaced grid cells and define their evolution and interaction by numerically approximating a set of equations for discrete time steps. Processes that occur on sub-grid scales, like convection have to be parametrized and are a major contribution to the uncertainty of climate model projections (McSweeney and Hausfather 2018). This section aims to deepen the understanding of the reader of how climate models work and to introduce key terms, conventions and definitions commonly used in climate analysis to facilitate clearer interpretation of results.

2.4.1 Climate Model Structure

The ground set of equations for weather and climate projection models are the evolution of wind speed $\mathbf{v}$ following from the equation of motion (Etling 2008)

$$\frac{\partial \mathbf{v}}{\partial t} + \mathbf{v} \cdot \nabla \mathbf{v} = \mathbf{F} + K_v \nabla^2 \mathbf{v} \tag{2.25}$$

the continuity equation for incompressible media

$$\frac{\partial \rho}{\partial t} + \mathbf{v} \cdot \nabla \rho = Q_l \tag{2.26}$$

the equation for inner energy

$$\frac{\partial T}{\partial t} + \mathbf{v} \cdot \nabla T = Q_T + K_T \nabla^2 T \tag{2.27}$$

the balance equation for the water phases q_i

$$\frac{\partial q_i}{\partial t} + \mathbf{v} \cdot \nabla q_i = Q_{q_i} + K_q \nabla^2 q_i \tag{2.28}$$

and the balance equation for different substances c_n

$$\frac{\partial c_n}{\partial t} + \mathbf{v} \cdot \nabla c_n = Q_{c_n} + K_c \nabla^2 c_n. \tag{2.29}$$

All of these equations consist of a numerically approximated variable evolution term $\partial/\partial t$, a convection term $\mathbf{v} \cdot \nabla \cdot$, a source term Q (or acting force $\mathbf{F}$) and a diffusion term $K\nabla^2$ with parameters Q and K. A motivation for all of these equations is given in the beginning of this chapter. Typically the velocity $\mathbf{v}$ and density ρ describe a package of wet air and the water phases q_i for gaseous, fluid and solid water govern their transition. An intuitive example for substances c_n are carbon dioxide (CO_2), ozone (O_3) and methane (CH_4). All of these substances are included in processes that occur on considerably smaller sizes than grid cells, but play an important role in the energy balance as greenhouse gases. Additional equations are used for specific problems, coupling mechanism, parameter evolution and other interactions.

Over the last centuries these models became more complex by simulating not only the atmosphere, but the ocean, land and sea ice in separate models that interact with each other by coupling mechanisms. To make sure the model does not drift away from physically reasonable states, it is tuned by varying observed parameters - like the source and diffusion parameters Q and K - within their uncertainties. As an example, the global coverage of ice sheets contributes to the earths albedo and can be used to keep the total energy balanced. The parameters are chosen such that the uncertainties are high relative to the desired impact. A more in depth introduction to climate models can be found in Spangler 2012.

Weather and climate models often use the exact same set of equations, but large differences remain. While weather models try to forecast time and location of single weather events, climate models specify on the statistical projection of long term trends. The weather forecast therefore needs precise initial conditions, while for decade long trends the boundary conditions like the energy balance are far more important. For the latter, multiple computations with different initial conditions are typically used to estimate the models uncertainty.

2.4.2 Model Inter-comparison Projects - CMIP6 and ScenarioMIP

Different coupling mechanisms, described processes and projection focuses can be challenging for analysts. To make multi-model analyses easier, the climate model inter-comparison project (CMIP) was founded, which aims to make the climate models of independent institutions easier to compare. All models can take part in CMIP by simulating a collection of test scenarios. Developers are helped with diagnostics, evaluation and characterization of experiments, which set the ground for comparability and reliability of results. These experiments consist of

1. an atmospheric model inter-comparison project
2. a preindustrial control with ocean-atmosphere coupling (piControl)
3. abrupt quadrupling of CO_2 concentrations (abrupt-4xCO_2) and
4. CO_2 concentration forced to increase by 1% per year (1pctCO_2).

To take part in the latest version (CMIP6), all four of them are mandatory to conduct. The first experiment uses the atmospheric component of the model and historical sea surface temperature (SST) and sea ice concentrations as boundary conditions. This makes it easy to evaluate the resulting error without contributions from the ocean and other components. The piControl simulation is a test of the global energy budget, which should not change without CO_2 forcing in the preindustrial conditions of 1850. The last two experiments are meant to help examine the atmosphere-ocean coupling.

Additional historical simulations are run by models with included radiative forcing, as observed from 1850 to the present. Radiative-forcing (RF) defines the evolution of greenhouse gases, which is then applied on grid cell parameters to force the system into different energy states. This impact test on historical data makes sure that the model is able to simulate trends lasting centuries long and the global climate as a whole. Models without RF can compare their results with directly with preindustrial observations. However, this might be redundant when tuning the model on the basis of these data.

The four mandatory experiments are chosen so that they are expected to vary little over time and do not have to be changed in different phases of CMIP. They were also established so developers do not have to invest much extra effort but run the experiments as part of the developing process either way. Another important success of CMIP was the establishment of common metadata and documentation. Alongside with this the infrastructure was built to allow automatic analysis with packages and therefore reduce effort for new projects. More information on the CMIP6 structure and organization can be found in Eyring et al. 2016.

As introduced earlier, greenhouse gases like CO_2 play a key role in the energy balance and therefore in long lasting trends of future projections. Since the real emissions are unknown, assumptions must be made to account for future concentrations. A range of different scenarios were proclaimed by the Intergovernmental Panel on Climate Change (IPCC), covering the space of realistically possible concentrations of greenhouse gas trajectories and providing a useful tool for analysts. The temporal evolution of greenhouse-gas emissions has to be defined before running the simulation and is called radiative forcing (RF). To achieve lasting comparability between models, emission pathways are defined in ScenarioMIP and run by most models. Resulting projections can then be directly compared between models of different institutes.

The scenarios are based on shared socioeconomic pathways (SSPs) and describe evolution possibilities of the worlds population, urbanization and GDP. These scenarios are solely based on socioeconomic narratives, where the five main ones are

1. Sustainability (SSP1)
2. Middle of the Road (SSP2)
3. Regional Rivalry (SSP3)
4. Inequality (SSP4)
5. Fossil-fueled Development (SSP5).

These are called the "tier 1" scenarios and have been developed in O'Neill, Kriegler, et al. 2013, O'Neill et al. 2015 and O'Neill, Tebaldi, et al. 2016. More scenarios with different progressions are also available as "tier 2" options. Integrated assessment models evaluated these SSPs and calculate the energy balance, land use, greenhouse gas emissions, air pollution and more, which can in turn be summarized as the amount of radiative forcing to be expected over the twenty first century. This has been done by Bauer et al. 2016 and Riahi et al. 2016 for the tier 1 SSPs listed above and is widely used by GCMs to project future developments.

While the real global development may take none of the above described pathways, it will partly consist of regionally different contributions of them. The best and worst case scenarios (SSP1 and SSP5, respectively) act as boundary scenarios with minimal and maximal conceivable greenhouse gas emissions and it is valid to assume the real pathway will evolve somewhere between them. The results therefore have to be interpreted accordingly, not as prediction of values but as boundaries of possible future developments.

2.4.3 Uncertainty in Climate Projections

Three sources of variability must be differentiated in climate projection analysis (Hawkins and Sutton 2009). The first one called scenario variability is introduced in the previous paragraph and covers the likelihood of the future pathway in regard to the actual socioeconomic development. The largest contributor here is the greenhouse gas emission estimate which is typically implemented as radiative forcing. Running the same model with identical radiative forcing and initial condition but different scenarios can help to access the magnitude of scenario variability.

The second source is the model variability and originates from process implementation, parametrization and resolution restrictions. Complex processes on sub-grid spatial scales like convection cells or radiation reflection can not be simulated and must be parametrized, which can embezzle their impact or lead to different dynamics. Moreover are the linear approximations of partial derivatives contributing to the model uncertainty and increase for longer simulated time periods. To quantify the resulting amount of variability, a large ensemble of GCMs with the same scenario can be run. The different sub-grid process

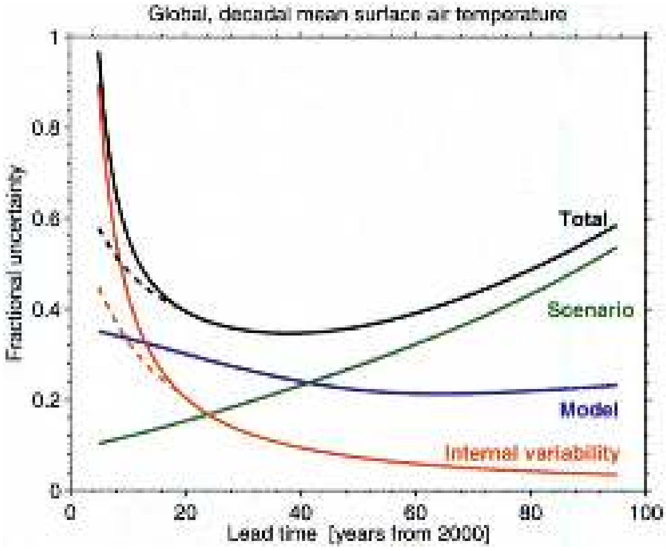

Figure 2.9: Relative contributions of internal variability, model variability ("model spread") and scenario variability to the total uncertainty of projected global mean surface air temperature over the number of simulated years. Fractional uncertainty is the division of the 90 % confidence interval by the mean prediction. Dashed lines show the possible improvement by special methods for starting conditions. Figure extracted from Hawkins and Sutton 2009.

implementation and parametrization leads to different results, where the model spread gives intel about the magnitude of model variability.

Internal variability originates from fluctuations due to the complex dynamics in the system, even without any radiative forcing. In the CMIP6 inter-comparison project, this observed historical fluctuation is also accessed by simulations, because the models are gauged to produce the same statistical output. Future scenario computations include this variability, since the underlying model structure does not change. As discussed before, the precise initial condition of the system does not play a significant role in climate models, because only the statistics of events have physical meaning. A set of different system starting states can therefore be used to evaluate a models internal variability.

The total uncertainty results from the combined contribution of the scenario, model and internal variability, which increases for larger projected time periods. The contribution of each variability source to the total uncertainty was evaluated in Hawkins and Sutton 2009 on an ensemble of GCMs for the surface air temperature. Internal variability is roughly constant in time, while model variability increases slowly and scenario variability is negligible for short time periods, but increases the quickest, which is sketched in Figure 2.9.

For projections into the far future, the scenario uncertainty is therefore the larges and model variability the second largest contributor to total uncertainty. To diminish the uncertainty of estimates a few methods are usually performed. First of all, multiple scenarios can be evaluated to compare the different results between the best and worst case to give an estimate of the possible range and upper and lower limits, which helps to project the change when humanity chooses a specific pathway. Longer simulation periods further enhance this difference, where the higher radiative forcing results in stronger impacts.

A second approach concerns the model variability, which is accessed by using an ensemble with different GCMs and using the spread of results as uncertainty. An underestimation of uncertainties can result when the models used are strongly correlated, which occurs often when institutes, for example, focus on the development of specific parts like the ocean-atmosphere coupling, but use the exact same atmosphere model. Lastly the internal variability can be handled by filter methods that try to identify the effect of radiative forcing as long lasting trends and suppress modes of higher fluctuations.

Chapter 3

Data and Methods

This section first explains the selection of general circulation models (GCMs) and the criteria and boundaries limiting the available data sets for this work. Furthermore the data sets used are explained and the calculated metrics are introduced, followed by the discussion of the PIKART atmospheric river catalog algorithm and the separation of extreme precipitation events into AR-associated and non-AR events. Afterwards, the low-frequency component analysis is explained, to filter out the feedback of radiative forcing from internal variability and how the results are used to calculate relative changes from low-frequency patterns.

3.1 Model Selection

The list of available general circulation models is long. To contain the necessary data for this work, the models need to be part of the climate model inter-comparison project in phase 6 (CMIP6) and part of the scenario inter-comparison project (ScenarioMIP) to have comparable simulations of multiple future scenarios. Both CMIP6 and ScenarioMIP have been introduced earlier in subsection 2.4.1. CMIP6 datasets are made publicly available on the Earth System Grid Federation meta grid (Federation 2019). Due to the high amount of data storage space and preparation time, only a selection of models can be evaluated. The criteria limiting the choice are listed below.

In atmospheric river analytics the integrated water vapor transport (IVT) is essential. It is calculated from specific humidity and zonal/meridional wind. The three variables must be accessible in pressure levels with a temporal resolution of 6 hours, which is denoted as "6hrPlevPt", where Pt denotes point-like representation of the 6 hour interval and Plev a division into vertical pressure levels. There are also hight levels available for some models which can be transformed into pressure levels, but they are excluded to save preparation time due to the abundance of better models. Precipitation and near-surface air temperature data are also needed, but available in nearly all models and therefore do not limit the range of options.

To assure comparability of different variables the same starting conditions (realization), initialization method, physics and forcing needs to be used. This is summarized as variant label and denoted as r1i1p1f1 (as an example), where the numbers indicate an ID from the models institution that do not have to align with labels from other institutions. The variant label can differ between models and scenarios, but must be the same for variables used in the same calculation. This ensures that, for example, the specific humidity and precipitation are from the same simulation run and will later regionally overlap, such that precipitation events can be liked to an identified atmospheric river.

Finally, the models should be somewhat independent, since otherwise the confidence in results will be overestimated when calculating ensemble means. For this, a cosine similarity score of < 0.8 from the evaluation of Ashfaq et al. 2022 is used. The chosen models and their native spatial resolution are listed in Table 3.1 and a table with all models considered and the selection criteria can be found in the appendix (Table A.1).

Model	Institution	spatial resolution (°)
GISS-E2-1-G	NASA-GISS	2.0 x 2.5
MIROC6	University of Tokyo	1.4 x 1.4
MPI-ESM1-2-HR	Max-Plank-Institute Hamburg	≈ 0.9
MRI-SM2-0	University of Hamburg	1.1 x 1.1
$NorESM2 - MM^*$	University of Oslo	1.2 x 0.9

Table 3.1: Selected Models satisfying all criteria with developing institution and native spatial grid resolution. The data of the model NorESM2-MM was not accessible because the data node (noresg.nird.sigma2.no) could not be reached.

3.2 Data

This section introduces all used variables, data sources and processing steps. To detect ARs one needs only three variables, the specific humidity q to account for the relative amount of water contained in the atmosphere and meridional/zonal wind u/v to describe the dynamics. Precipitation pr and near-surface air temperature tas are used to calculate impact related metrics and to quantify global climate change, respectively.

First of all, the meteorological weather reanalysis data ERA5 from the European Center for Medium-Range Weather Forecasts is used. It is available for free use on `https://cds.climate.copernicus.eu/datasets/reanalysis-era5-single-levels?tab=overview` ((C3S) 2018) and uses observational data combined with models to produce a uniform grid of the atmosphere, ocean and land from 1950 (or earlier, but with larger uncertainty) to present. This dataset gives the best current estimate of historical weather events and is widely used in climate and impact related studies. The native grid has a 0.25° spatial and hourly temporal resolution. The specific humidity q and meridional/zonal wind u/v are used to test the functionality of the PIKART algorithm for different grid resolutions to help decide which models to use for the projection analysis.

This work focuses on the future projection of atmospheric river statistics and impacts. Therefore data is necessary which includes all years from the historical period (1950) to the far future period (2100). The model selection is already described in subsection 2.4.1. The scenarios SSP1-2.6 and SSP5-8.5 are chosen to have the maximal projection discrepancy and to increase the signal-to-noise ratio by having larger projected differences. The scenarios stand for the best and worst case socioeconomic pathways introduced in subsection 2.4.1 with radiative forcing of $2.6\,\mathrm{W\,m^{-2}}$ and $8.5\,\mathrm{W\,m^{-2}}$, respectively. To simplify their often used labels, they will be called "ssp126" and "ssp585" from here on.

All variables are downloaded with the highest possible spatial resolution, resulting in 6 hour time steps for q, u, v and daily time steps for pr, tas. The spatial step width within each model is identical for all variables, but deviates across models and meridional/zonal directions between 0.9° and 2.5°. Model specific resolutions are listed in Table 3.1. All atmospheric river data (q, u, v) are interpolated to a shared grid with $1° \times 1°$ spatial steps by bi-cubic interpolation to preserve extreme values. If necessary the data are shifted (by 3 hours) in time to commonly start at 3 am. Missing leap years are filled in by copying the last entry of the 28th February (this only applies to the model GISS-E2-1-G). This makes it easier to check the completeness of the downloaded dataset and for further analyses. Daily data (pr, tas) are also re-gridded to the same grid and missing leap years are added.

3.2.1 Extreme Precipitation Metrics

To evaluate the impact of climate change on precipitation hazards, we define the annual maximum precipitation per grid cell

$$(px1)_{np} = max_n(p_{dp}; d = 1, ..., n_y) \tag{3.1}$$

as the intensity of extremes and the frequency of extreme precipitation with

$$(fx)_{np} = \sum_{d=1}^{n_y} H(p_{dp} > 99\%), \tag{3.2}$$

where subscripts p, d, n, n_y denote grid points, days, years and days of a year, respectively. p denotes global precipitation flux in kg/m^{2}s. The frequency is obtained by first calculating the 99th percentile threshold of the historical time span from 1950 to 1970. Then, the days per year in which this threshold is surpassed are counted. The historical reference period is chosen to increase the sample size for increased statistical precision on the one hand, but limit the impact of radiative forcing on this period to accurately determine relative changes due to increased global temperature on the other hand.

The real impact damage of extreme precipitation events is difficult to quantify. Heavy rainfall benefits if the ground can soak the water up and can cause landslides and flooding otherwise. The metrics used here strongly simplify a complex evaluation, but they are intuitive, quick to implement, and good first impact indicators. A more in depth evaluation is not possible in this work due to time constraints. The same variables are used in Kotz et al. 2023 except for a different threshold time period. The one here is chosen simply for data availability reasons.

Extreme precipitation events are typically considerably smaller in temporal and spatial size compared to the resolution of climate models (Matte, Christensen, and Ozturk 2021). One must therefore be cautious to keep the tail of the distribution. The re-gridded fields here mostly do not downsample the datasets and the bi-cubic method marginalizes the risk of smoothening peak values from the native grid. This attempts to retain as many extreme values and their intensity as possible.

3.2.2 Integrated Water-Vapor Transport (IVT)

To analyze atmospheric river (AR) projections, the specific humidity q and the zonal/meridional wind u/v are taken with 6 hour temporal and the highest available spatial resolution (s. Table 3.1) to calculate the integrated water vapor transport (IVT).

Here, the AR variables are combined to one field of integrated water vapor transport (IVT). This is one of two typical approaches to identify ARs with the benefit of accounting for both amount and velocity of water moisture across all height levels. The second approach is to use integrated water vapor (IWV) to describe the amount of water vapor in an atmospheric column which gives an upper limit for the possible precipitation. The IVT fields are calculated with

$$IVT_u = -\frac{1}{g}\int_{925hPa}^{250hPa} u(p)\cdot q(p)\,\mathrm{d}p, \tag{3.3}$$

$$IVT_v = -\frac{1}{g}\int_{925hPa}^{250hPa} v(p)\cdot q(p)\,\mathrm{d}p, \tag{3.4}$$

$$IVT = \sqrt{IVT_u^2 + IVT_v^2}. \tag{3.5}$$

Earth's gravitational constant g is used to express the resulting field as a flux (kg/ms), while the pressure integration includes all height levels. Negative signs are convention to obtain positive values for north/east-directed transport. For observational data, the integration limits usually range from 1000 hPa to 300 hPa, but the boundaries here are chosen to align better with the pressure levels produced by the models. Since most of the water vapor remains in lower levels, the contribution of the upper most levels is small and the pressure in the lowest level is usually not reached in the simulations, resulting in missing values. Therefore, the change in the integration boundaries of pressure levels can be neglected.

3.3 Atmospheric River Tracking Algorithm (PIKART)

The new PIKART method from the Potsdam Institute for Climate Impact Research (PIK) to detect and track atmospheric rivers will be used in this work to produce a catalog of future ARs from multiple global climate models. The algorithm was developed by Sara M. Vallejo-Bernal and published in Vallejo-Bernal et al. 2025. The source code was made available and has been changed only slightly to handle different input grids and models. The first parts of the algorithm handles data preparation and was done manually here due to the differences in input data.

To produce a catalog, the PIKART algorithm calculates IVT fields and identifies anomalies using a top-hat by reconstruction process (THR; first used in IPART and developed by Xu et al. 2020). The resulting anomalies are taken as AR candidates. Then, typical geometric criteria are applied to filter out unreasonable shapes and other atmospheric phenomena like cyclones and low-level jets. The remaining shapes are assembled to AR tracks and then saved after calculating track specific metrics.

3.3.1 Top-Hat by Reconstruction (THR)

Top-hat by reconstruction is an image processing operation that extracts the peaks of a arbitrary dimensional distribution. It is used by the PIKART algorithm and explained here to better understand the catalog results. In the THR, dilation is performed on a marker image J until stability and then subtracted from the original image I as explained in Vincent 1993.

Dilation is an elementary image operator where the pixels take the maximum value of a given neighborhood E of the initial marker image J, as long as the image I is not surpassed. It is denoted as $\delta_I^{(n)}(J)$, where n is the number of times this operator is applied. For sufficiently high n this operation is called reconstruction and the peak values fill the whole subarea of I. This is illustrated in Figure 3.2 and can easily be extended to grayscale images by repeating for every gray level.

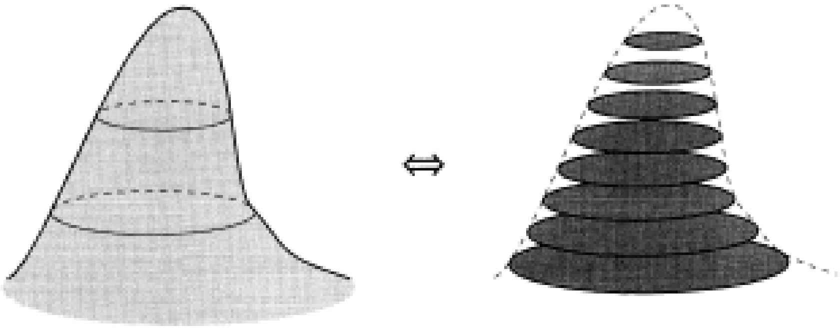

Figure 3.1: Segmentation of a grayscale image into layers where THR can be performed separately. Figure extracted from Vincent 1993

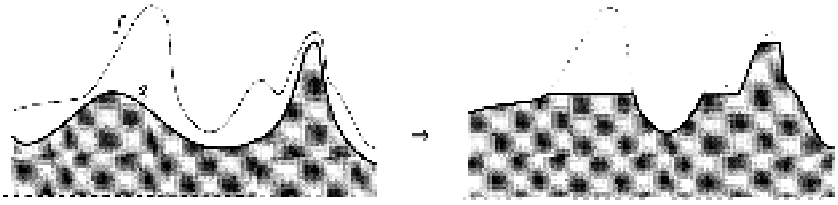

Figure 3.2: Grayscale reconstruction of image I with values $f(p)$ and marker image J with values $g(p) < f(p)\ \forall p \in I, J$ in the one dimensional case. Figure extracted from Vincent 1993

Luc Vincent proposed to subtract a fixed height parameter h from the original image I to obtain the marker image J, such that

$$\forall p_j \in J, p_i \in I : f(p_j) \leq f(p_i), \tag{3.6}$$

(denoted as $J < I$) is satisfied. Here, $f(p)$ is the pixel value of point p. Another option is to do grayscale erosion, which is similar to dilation, except that the neighborhood minimum is taken. This also fulfills $J < I$ and is used by Xu et al. 2020 who first proposed this method to identify ARs from IVT fields. In the PIKART algorithm (Vallejo-Bernal et al. 2025), a 87.5 % local threshold is used as marker image J and therefore also in this work.

In THR, the size of the spatiotemporal neighborhood plays a significant role, since it determines the magnitude of anomalies which are searched for. It is therefore important to choose parameters such that the resulting region spans the size of typical AR activity. This is around 1000 km in length and 8 days in lifetime (Guan and Waliser 2019). A resolution of 6 h and 1° × 1° results in

$$k_0 = \frac{8 \cdot 24\,\mathrm{h}}{2 \cdot \tau_{time}} = 16 \tag{3.7}$$

$$k_{1,2} = \frac{1000\,\mathrm{km}}{2 \cdot 110\,\mathrm{km}/^\circ \cdot \tau_{lat/lon}} \approx 5 \tag{3.8}$$

grid points and serve as semi-major/semi-minor axis to define the spatiotemporal ellipsoid neighborhood $(k_0, k_1, k_2) = (16, 5, 5)$, where k_0 is the number of grid points in time and $k_{1,2}$ the number of grid points in longitude and latitude, respectively.

The THR reliably detects anomalies, even if the background experiences strong changes. The IVT field shows seasonal differences, spatial changes from the tropics over the extra tropics to the poles, and temporal changes with increasing IVT values over decades due to climate change. This makes THR the optimal method for the dataset used in this work.

3.3.2 Geometric Criteria

The resulting high-IVT anomalies are taken as AR candidates and then further analyzed to satisfy typical AR geometric criteria to filter out other high-IVT atmospheric phenomena such as nearly stationary moisture fields, cyclones or low-level jets. The length criterion is $l \geq 1500\,\mathrm{km}$ to filter out possible remaining noise and other small anomalies that cannot transport large amounts of water due to their size. The area $a \in [5 \cdot 10^5 \mathrm{km}^2, 18 \cdot 10^6 \mathrm{km}^2]$ criterion also filters small candidates for the same reason and areas too large to be created in ocean-basins.

The roundness $4\pi a/\rho^2 \leq 0.7$ with the perimeter ρ is introduced in Xu et al. 2020 to pre-separate ARs from cyclones with minimal false-negative, i.e. most AR shapes are kept at the expense of also falsely keeping many cyclones. Afterwards, the length-width ratio $l/w \geq 2$ with typically observed values of $\approx 5 - 6$ (Guan and Waliser 2017) are calculated by finding the AR axis. Since this involves path-finding optimization, the prior out sorting of some cyclones saves time. Both roundness and length/width ratio aim to exclude cyclones efficiently, which are of similar IVT magnitude but typically round due to their rotation. However, events can coexist and overlap, which makes perfect separation impossible.

3.3.3 Tracking

The remaining fields are then tracked in time by calculating a similarity index of the shape of AR_i at time t and the shape of AR_j at time $t+1$ as

$$SI_{ij} = \frac{\sum_{p \in AR_i \cap AR_j} IVT_p^i \cdot area_p}{\sum_p IVT_p^j \cdot area_p}, \tag{3.9}$$

where the AR candidate of the next time point with the largest index is interpreted as the continuation and a list of connected AR candidates is called an AR track. Single tracks are discarded, as well as unrealistic centroid velocities outside the interval $v \in [9\frac{km}{h}, 90\frac{km}{h}]$. A more detailed description and exceptions can be found in Vallejo-Bernal et al. 2025. The resulting AR tracks and their properties are then saved in the PIKART catalog.

3.3.4 Separation of Atmospheric River Caused Extreme Precipitation Events

The calculation of intensity and frequency of extreme precipitation as well as the identification of ARs with the PIKART algorithm are already introduced in the previous sections. Both these methods/metrics now have to be combined into the calculation of separate AR and non-AR caused events by using the precipitation extremes defined in Kotz et al. 2023 and the AR footprints from the algorithm created by Vallejo-Bernal et al. 2025. The general idea is to use the spatiotemporal AR shapes identified by the catalog and combine all daily shapes into one, to account for the time resolution change from 6 h to 1 d. A causal connection is assumed between AR and precipitation, if the AR was present in the same grid cell at the same time step.

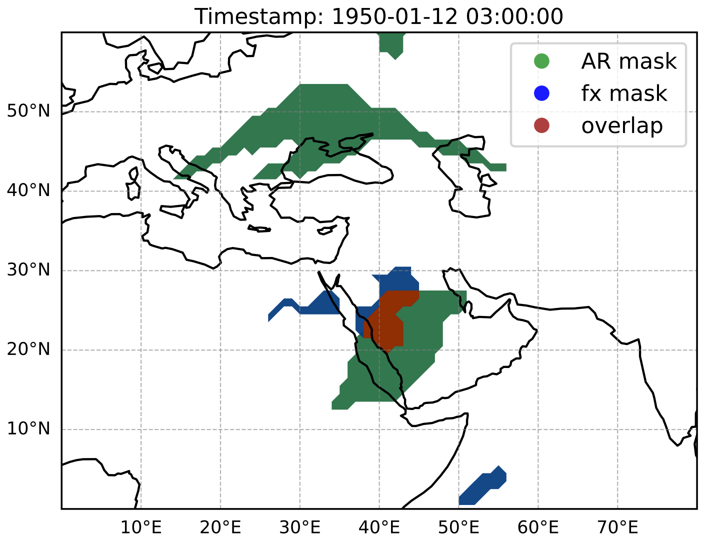

Figure 3.3: Identification of AR caused extreme precipitation events. Displayed is a historical timestamp of the model GISS-E2-1-G over Arabia, with AR footprints in green, precipitation events exceeding the 99th percentile in blue and overlapping regions in orange.

Intensities are linked with ARs by multiplying the footprint masks with daily precipitation data before taking the annual maximum. This drastically reduces the number of remaining time steps and can lead to empty grid cells. The prior maximum of annual precipitation may then no longer be included and the new maximum is calculated from the list of remaining AR caused events.

Frequencies are linked by combining the regions which surpass the historical 99th percentile with the daily aggregated AR shapes. This is visualized for one example timestamp in Figure 3.3 over the Arabian Peninsula. AR caused extreme precipitation events are then identified as overlapping regions and summed up per year to calculate the annual AR cause extreme frequency.

The remaining events not caused by ARs are also evaluated by inverting the AR footprint masks. The three different metrics are labeled AR caused, noAR caused, and pr (short for all precipitation) events.

3.4 Climate Change Signal Identification

To identify the climate change signal in the data, a low-frequency component analysis (LFCA) is performed. It filters the impact of radiative forcing from internal variability, like seasonal cycles and multi-year oscillations in sea-surface temperatures. In LFCA a standard principal component analysis is combined with a linear Lanczos low-pass filter on the temporal dimension of the data. The realization followed the theoretical framework of R. C. Wills et al. 2018 and results in better signal-to-noise ratios than other methods (R. C. J. Wills, Battisti, and Armour 2020).

3.4.1 Lanczos Low-pass Filter

The Lanczos low-pass filter is defined as the convolution of the Lanczos window

$$L_a(x) = \begin{cases} 1, & x = 0 \\ \frac{a\sin(\pi x \cdot f_c)\sin(\pi \frac{x}{a})}{\pi^2 x^2 f_c}, & -a \leq n \leq a; x \neq 0 \\ 0, & \text{otherwise} \end{cases} \tag{3.10}$$

with the data. The parameter a determines the size of the window and therefore the number of neighbors considered in the smoothing. The cutoff frequency f_c is introduced as a relative parameter to handle discrete data and is fixed between $0 < f_c \leq 0.5$, so that some frequencies must be passed, but frequencies equal to or higher than the Nyquist frequency (half the sample frequency) are always cut off. The Lanczos windows for different window sizes a are shown in Figure 3.4a and their discrete Fourier transform (DFT) in Figure 3.4b to visualize the effect of the cut-off frequency. The latter approximates a step function for the larger a, which makes clear that a increases the sharpness of the frequency cutoff and that the frequencies $f = f_c$ are halved in amplitude.

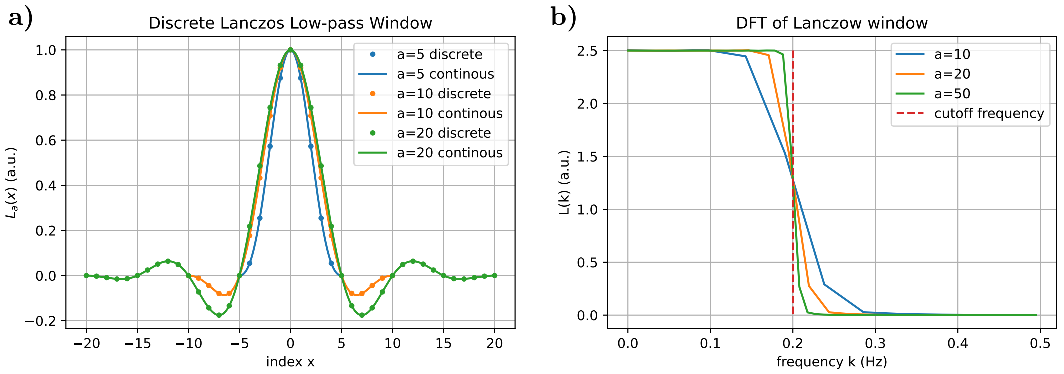

Figure 3.4: a) Lanczos window for fixed cut-off frequency f_c and different parameters a in its continuous form and the discrete realization. b) DFT of Lanczos windows with different a and the same cut-off frequency f_c.

The Lanzcos low-pass filter acts on a given sample matrix X like a linear matrix

$$(L_a \circ X)(t) = XL := X[l_1\, l_2\, l_3 \ldots], \tag{3.11}$$

where the discrete Lanczos windows l_k per sample k span the symmetric matrix L. To better understand the effect of the Lanczos low-pass filter, a double frequency example with a sample rate of $f_r = 1s$ is analyzed and shown in Figure 3.5. The data is defined as

$$X = \sin(0.21t) + 0.5\sin(2.23t), \tag{3.12}$$

with 100 samples and the low-pass is configured with $a = 50$ and $f_c = 0.2$. Subsequently, the data frequencies are $f_1 = \frac{0.21}{2\pi \cdot f_r} = 0.033Hz$ and $f_2 = \frac{2.23}{2\pi \cdot f_r} = 0.355Hz$ with a cut-off frequency of $f_c = 0.2 \cdot f_r = 0.2Hz$. In Figure 3.5, it can be seen that the lower frequency f_1 remains, while the higher f_2 is suppressed, as intended.

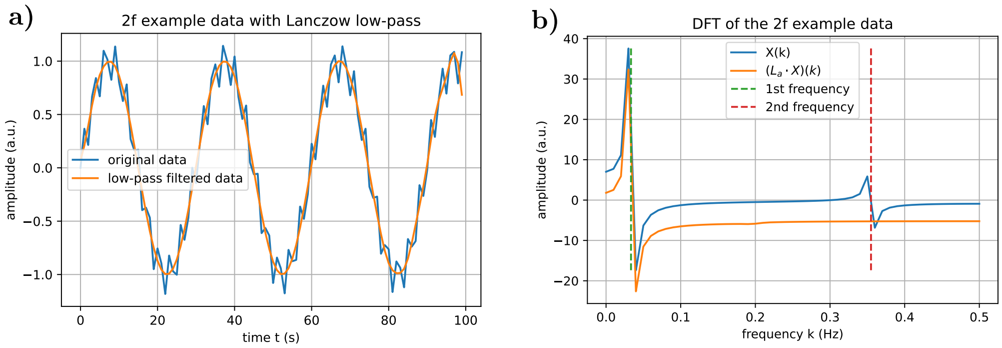

Figure 3.5: a) Double frequency (f_1, f_2) example data X with sample frequency $f_r = 1\,\mathrm{s}$ and applied Lanczos low-pass filter with cut-off frequency $f_1 < f_c < f_2$. b) DFT of the $2f$ example data and the low-pass filtered data. The latter is shifted down for better visibility.

3.4.2 Low-Frequency Component Analysis (LFCA)

The LFCA starts as a principal component analysis (PCA) by calculating the temporal variances and their corresponding principal components (PCs). The data is then Lanczos low-pass filtered, before maximizing the ratio of low-frequency variance to total variance by a basis transformation.

The original three-dimensional ($time \times lat \times lon$) data is reshaped to a two-dimensional $n \times p$ spatiotemporal data matrix X, where $n = dim(time)$ is the temporal dimension and $p = dim(lat) \cdot dim(lon)$ is the spatial dimension. The data matrix X is shifted to have zero time-mean and weighted by the square root of grid-cell area. One defines the covariance matrix

$$C = \frac{X^T X}{n-1}, \tag{3.13}$$

to calculate the eigenvectors v_k and eigenvalues σ_k^2 such that $Cv_k = \sigma_k^2 v_k$ and the sum $\sum_{k=1}^{p} \sigma_k^2 = \sigma_{tot}^2$ is the total temporal variance of the data. Since C is symmetric and positive semi-definite, and

$$Rank(C) = Rank(X^T X) = Rank(X) \leq min(n, p), \tag{3.14}$$

there are $p - Rank(X)$ zero eigenvalues and the rest are real and positive. The numerical calculation produces positive and negative near-zero eigenvalues due to machine noise, which are filtered together with small variances by reducing the dimension to the truncation N, so that only the N largest variances and their eigenvectors remain. These N vectors are also often called the empirical orthogonal function (EOF's) and their projection onto the data matrix produces the principal components $PC_k = \sigma_k^{-1} X v_k$.

In LFCA one produces the low-pass filtered principal components $\widetilde{PC}_k = \sigma_k^{-1} \widetilde{X} v_k$ by projecting the filtered data $\widetilde{X} := XL$ onto the original eigenvectors of C. Then, their covariance matrix $R_{ij} = cov(\widetilde{PC}_i, \widetilde{PC}_j)$ for $i, j \in [1, N]$ is calculated with eigenvalues

$$r_k = \frac{(\widetilde{X} u_k)^T (\widetilde{X} u_k)}{(X u_k)^T X u_k} = \frac{u_k^T L^T C L u_k}{u_k^T C u_k}, \tag{3.15}$$

such that $Re_k = r_k e_k$. The vectors u_k are the new basis vectors that are chosen as

$$u_k = \left[\frac{v_1}{\sigma_1} \; \frac{v_2}{\sigma_2} \; \ldots \frac{v_N}{\sigma_N} \right] e_k \tag{3.16}$$

to maximize the ratios of low frequency variance to total variance r_k. By projecting the Covariance onto this basis, the spatial low frequency patterns $LFP_k = X^T X u_k$ are calculated and show the low-frequency temporal variance per grid point. The low frequency components $LFC_k = X u_k$ are determined by projecting the data onto the new basis vectors and display the strength of the corresponding pattern LFP_k over time.

The total climate change signal is then identified as spatial pattern in the first LFP and as temporal evolution in the first LFC and can be reconstructed as

$$\text{reconstruction}_{p,y} = \text{LFP}_p \cdot \text{LFC}_y + \text{climatology}_{p,y}, \tag{3.17}$$

with subscripts p, y as spatial grid points and year, respectively. The climatology represents the original time-mean in the data.

In this work, the Lanzcos window size a is set to halve the temporal size of the data ($N_y/2$ for positive N_y and $(N_y - 1)/2$ for odd N_y, where N_y is the number of years). This ensures a reasonable computation time and relatively sharp frequency filtering, while keeping edge-effects in check. The effect of the truncation N and cutoff time T have been studied in R. C. Wills et al. 2018 with $N = 30$ and $T = 10$ years. However, since they investigated slowly changing sea-surface temperatures to identify multiple patterns apart from climate change, such as the pacific-decadal oscillation and El Niño southern oscillation, a higher cutoff time of $T = 20$ years is chosen to filter out these fluctuations, since this work focuses only on climate change. To retain the full extend of climate change impacts in the data, a flexible truncation number $N \geq 10$ is chosen to ensure at least 70 % of total spatiotemporal variability is kept. These ideas were first presented in Kotz et al. 2023 and are adopted for both their underlying rational and to provide comparability.

3.5 Projected Changes and Scaling Rates

With the climate change signal identified and reconstructed as described above, the results can now be used to calculate differences between historical and future projections, which are then compared to expected scaling rates. The differences are calculated by subtracting the reconstructed historical average from 1950 to 1970:

$$\mathrm{diff}_{p,y} = \mathrm{reconstruction}_{p,y} - \langle \mathrm{reconstruction}_{p,1950-1970} \rangle. \tag{3.18}$$

Changes can then be expressed relative to the historical baseline values, which is again a 20-year average of the original data X from 1950 to 1970:

$$\mathrm{change}_{p,y} = \frac{\mathrm{diff}_{p,y}}{\langle \mathrm{X}_{p,1950-1970} \rangle}. \tag{3.19}$$

Here, division by zero and small machine noise values is prevented by calculating only those grid points, where the historical baseline is larger than a threshold. Otherwise, uncontrolled missing values occur together with extremely large relative changes. The thresholds are set to $0.21\,\mathrm{mm}$ and $0.01\,\mathrm{yr}^{-1}$ for intensity $px1$ and frequency fx of extremes, respectively. Actual found minima in intensities ranged from $0.7\,\mathrm{mm}$ to $0.3\,\mathrm{mm}$ and from $1.4 \times 10^{-4}\,\mathrm{mm}$ to $1.7 \times 10^{-14}\,\mathrm{mm}$. This gap is interpreted as separation between machine noise and real values. The minimum in frequency data when excluding zeros is $0.04\,\mathrm{yr}^{-1}$, which the threshold undercuts.

Zero occurring precipitation events in a given grid-cell over a historical period of 20-years do not exist in normal precipitation data. However, when selecting AR-events as discussed above, regions with few AR activity (here mostly contributing are the Himalayas, Andes and Antarctica) reduce the number events drastically and produce these problems. Excluding those affected regions can slightly increases global averages, but this effect is only relevant in AR events with $\approx 3\,\%$ affected land area.

Changes of intensity and frequency are then computed into area-weighted averages. Spatial averaging is restricted to land areas without Antarctica to improve the relevance for impact assessments. The continent is excluded because it is a desert with little precipitation, it is poorly simulated due to lacking high-resolution historical observations and it is uninhabited, which limits its relevance for impact studies. Moreover, the comparability of results with Kotz et al. 2023 remains intact, where the same choice has been made. Areas excluded from the historical period and the land mask are also excluded from the total area considered. Temperature differences are still treated globally, because water vapor is created in many grid-cells and transported large distances before precipitating down. Therefore, the temperature in grid-cell p does not cause the changes in extreme precipitation metrics of grid-cell p, but many different regions do. The temperature differences are therefore computed into global averages.

Exponential scaling rates are then estimated on these averages based on the expected thermodynamical relationship in Equation 2.24, which is introduced in the theory chapter and states

$$p/p_0 = e^{\frac{Q_m}{R}\left[\frac{1}{T_0} - \frac{1}{T}\right]}.$$

Here p denotes pressure, with the reference value $p_0 \equiv p(T_0)$, Q_m is the molar latent heat, R the effective gas constant for wet air and T_0 the reference temperature. This can be simplified with a Taylor expansion for small temperature differences $\frac{1}{T} \approx \frac{1}{T_0} - \frac{T-T_0}{T_0^2}$ and therefore $p(T)/p_0 \approx e^{\mu \Delta T}$ with the exponential scaling factor $\mu = \frac{Q_m}{RT_0^2}$. Resulting changes and temperatures are then least-square fitted with the function

$$f(\Delta T) = e^{\mu \Delta T} - 1, \tag{3.20}$$

where μ is the desired scaling rate and $\Delta T = T - T_0$ the difference in global-mean temperature tas to the historical reference period. The leading error of this approximation is therefore the third component of the Taylor-expansion with a difference $\mathcal{O}(\Delta T^2/T_0^3) \approx \mathcal{O}(7 \times 10^{-7}\,\mathrm{K}^{-1})$ for temperature changes up to $4\,\mathrm{K}$ and a reference temperature of $T_0 = 287.2\,\mathrm{K}$.

Chapter 4

Results

With the chosen models and their data calculated into the needed metrics, the elaborated methods can now be applied. This section presents all results from the analysis performed, starting with a test of the PIKART algorithm on observation-consistent data for different resolutions. Afterwards the projected catalog results are analyzed for their temporal evolution and possible differences in their distributions are investigated. Lastly, the climate change signal is identified in temperature and extreme precipitation metrics along with a scaling rate comparison of AR- and non-AR-caused extreme precipitation events with a prior test of the methods on simulated integrated water-vapor transport.

4.1 Spatiotemporal Resolution Differences

First, the PIKART algorithm from Vallejo-Bernal et al. 2025 is tested for its resolution sensitivity on ERA5 reanalysis data with a native spatial 0.25° and hourly temporal resolution. ERA5 data from 2018 to 2020 (included) is downloaded and downscaled to different temporal and spatial resolutions to check the impact on AR detection results. The number of grid points and therefore roughly the amount of required data space inversely scales with multiples of the native resolution, i.e. if the resolution in one dimension is doubled, the required data space is approximately halved. This section aims to determine an appropriate regridding resolution for the model data while preserving the detection results.

The highest resolution tested is 0.5° spatially and 6 hours temporally. This is similar to most other AR studies in the literature and the highest reasonable values, since most models have spatial resolutions between 1° and 3° and temporal resolution of 6 hours or longer. Upscaling those would only increase effort, but the input information stays unchanged and increased result quality cannot be expected. The kernel size of the top-hat by reconstruction (THR) method used to identify anomalies in the integrated water-vapor transport (IVT) fields is resolution dependent and must be changed according to Equation 3.7 to match the resulting grid-cells with actual AR observations. The spatial step widths in the latitude and longitude directions are always kept the same. Figure 4.1 shows a probability mass function of lifetime, area and IVT and the total number of ARs detected for different spatial and temporal resolutions. All distributions are normalized by the total counts of the highest resolution tested. Long tails are cut off, since the few counts result in strong fluctuations but no visible resolution dependent differences. The metrics are chosen as first AR indicators to evaluate the impact of lost tracks.

Different spatial resolutions of 0.5°, 1°, 2° and 3° are tested with fixed 6 h time steps and are shown in Figure 4.1a-c. All results are shown relative to the first case. Since the data is two-dimensional in space the factor by which the data amount changes is squared. The listed steps divide the number of remaining data points by 4, 16 and 36, respectively. The first case reduces the count of detected AR tracks to 95 %, while for the last only 77 % of tracks remain. Lifetime values are slightly reduced for higher spatial resolutions, but overall change little due to the fixed temporal step width of 6 h. Area and IVT decline mainly at the peak of their distribution.

For temporal resolutions, 6 h, 12 h and 24 h are tested with fixed spatial step widths of 1°. The results are shown in Figure 4.1d-f, relative to the grid with 6 h and 0.5°. The approximate data reduction factor is 4, 8 and 16, respectively from contributions of both time and space regridding. The detected ARs reduce

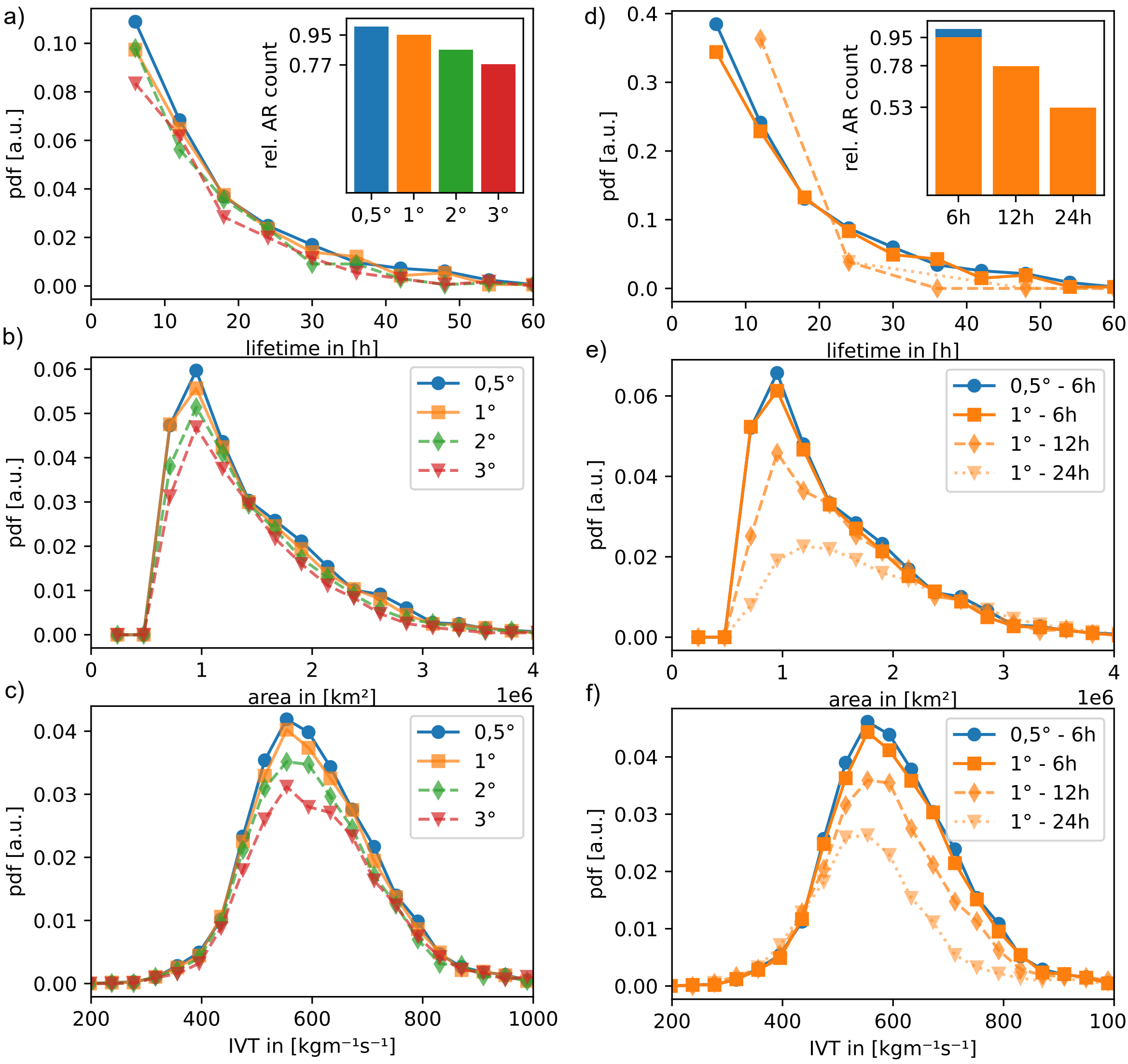

Figure 4.1: Catalog comparison for a)-c) different spatial and d)-f) different temporal resolutions of ERA5 reanalysis data from 2018 to 2020, included. Total AR counts and probability mass functions are shown relative to the highest tested resolution (blue). Tails of the probability density function are cut off to highlight high-count changes.

quicker with only 95 %, 78 % and 53 % remaining. Lifetime distributions are time-resolved according to the step widths. The 12 h case still detects some shorter tracks, while the 24 h case cuts off most of them. The distributions in area and IVT show large losses for small areas and large IVT values. This occurs, because AR shapes overlap less in consecutive time steps if the time distance increases. Therefore IVT fields are averaged which strongly reduces intensity. ARs with small area are then less likely to be detected, while IVT values are diminished overall. For large time steps, AR shapes can stop overlapping completely and are no longer recognized as ARs by the PIKART algorithm, which needs overlapping to concatenate shapes into tracks.

For spatial downscaling the losses are smaller compared to the saved data space, while temporal downscaling has a stronger and irregular impact. An optimal resolution of 1° is chosen in the longitude and latitude direction and 6 h in time. This results in only 5% additional losses in this ERA5 test sample and reduces the amount of data by a factor of 4, while also aligning well with the typical available resolutions from most general circulation models.

4.2 Projections of the Atmospheric River Catalog

With the data prepared as discussed in section 3.2 and the resolution choice from the section above, the PIKART algorithm from Vallejo-Bernal et al. 2025 is now applied for the first time on simulated data of a historical and two future scenarios of four different climate models. The source code of the algorithm was provided to the author and only minor changes had to be made to accommodate for different datasets and spatiotemporal resolutions. The resulting catalogs include many characteristic AR variables from which a selection is analyzed here.

4.2.1 Future Trends

First of all, a general development is investigated by calculating yearly averages (except for AR counts, which are summed up). This is a good estimate of causality since years with high global-mean temperature induce changes to AR characteristics rather quickly due to the fast dynamics of the atmosphere. A consecutive cold year will therefore show little to no delayed changes caused by the previous hot year. The yearly metrics are then plotted against the global area-weighted mean near-surface air temperatures for that year. This shows the changing trends due to climate change.

The investigated metrics are lifetime, area, length, width, mean IVT, centroid latitude and longitude, speed and the count of detected ARs. Counts are the total number of AR tracks in a year. Centroid longitudes are the circular-mean values per track to better evaluate the position of the AR and prevent boundary issues, while all other metrics are maximal values per track. The centroid latitude estimation takes the maximum of absolute values to increase visibility of possible poleward shifts and reduce noise by doubling counts. This gives a broad insight into the geometrical and physical characteristics of ARs and their temperature dependent evolution. The results along with the ensemble means are shown in Figure 4.2. Linear trends are identified by least-square fitting the ensemble means with uncertainties resulting from estimated covariances.

The included IVT changes most dominantly with $(29.1 \pm 0.8)\,\mathrm{kg/msK}$ and high agreement between models. Trends in all other metrics are small with relative changes on the order of $\mathcal{O}(10^{-3})$ compared to mean values. Uncertainties are large relative to magnitudes, which makes most changes either statistically insignificant, or indistinguishable from zero. Detectable social, environmental or economical impacts are therefore unlikely.

Nevertheless, slight trends may be present for some metrics. The length shows a potential increase by $(16 \pm 8)\,\mathrm{km/K}$. The global mean poleward position (here denoted centroid latitude in $^\circ N$ and means distance to the equator) shows no change, although a poleward shift was expected and will be further analyzed later. Other small potential trends may be inferred for the centroid speed with $(0.16 \pm 0.05)\,\mathrm{km/hK}$, the centroid longitude with $(-0.16 \pm 0.08)\,^\circ/\mathrm{K}$ and the total number of AR tracks with $(-12.8 \pm 1.9)\,1/\mathrm{K}$.

4.2.2 Distributions of Atmospheric River Characteristics

After the analysis of the change of average metrics with global mean temperature above, the probability density function of the same metrics can show additional changes in their distribution. Only 20 years from 1950 to 1970 and 2080 to 2100 for historical and future scenarios are analyzed to highlight possible differences. Ensemble mean's are calculated by the average bin count of all models. The same metrics are used as in the previous paragraph, except for the number of detected AR tracks. Overall, all metrics except IVT show little change between scenarios and trends determined in the previous analysis can not be seen by eye, because the order of estimated relative changes is too small.

Lifetime, area, length and width distributions are displayed in Figure 4.3 with logarithmic y-axis scale to highlight extreme values. The area and length metrics show a cutoff at low values resulting from the geometric criteria. The area, length and width distributions exhibit a peak at roughly $0.75 \times 10^6\,\mathrm{km}^2$, $2500\,\mathrm{km}$ and $350\,\mathrm{km}$, respectively and decay roughly exponentially towards larger values. Lifetimes decay without a prior peak and start from $12\,\mathrm{h}$ because IVT anomalies must exist for at least two time steps to be considered an AR in the PIKART algorithm. All four metrics show no visible or significant differences between the ssp585 scenario and the historical distribution. The extreme values show increased variability due to the low counts, but also no differences between scenarios.

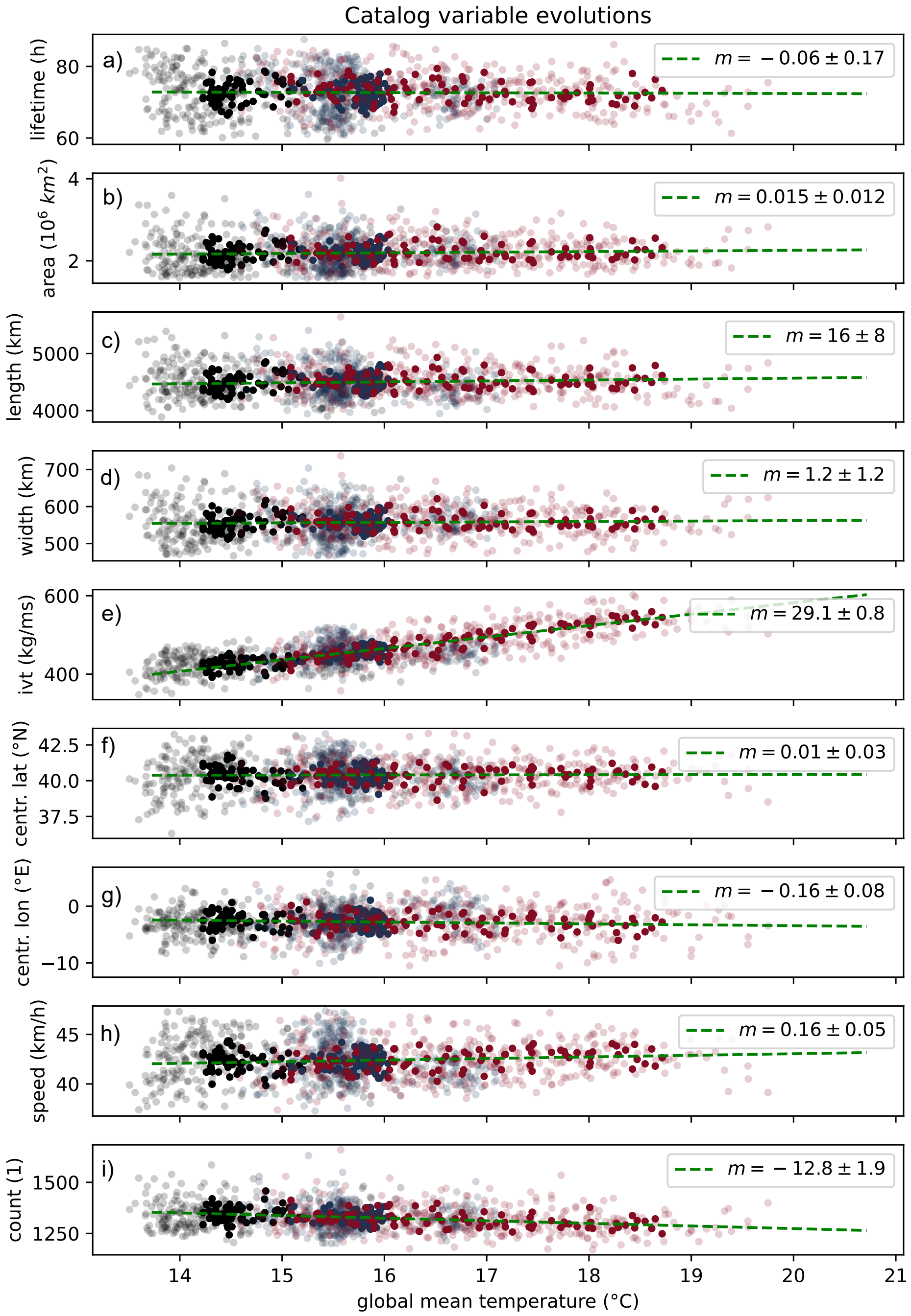

Figure 4.2: AR characteristic metrics from the PIKART catalog for all selected models as listed in Table A.1. Scenarios are color coded according to IPCC convention (black/blue/red for historical/ssp126/ssp585, respectively). Mean values per year (except for counts which is summed up) from 1950 to 2100 are plotted against global area-weighted mean surface air temperature. Individual GCMs are shown in the background and their ensemble means in opaque. Linear trends (green) are least-square fitted on ensemble mean values with their results in variable units by Kelvin.

Distributions of IVT, centroid latitude, centroid longitude and track speed are shown in Figure 4.4 with longer tails being cut off for IVT and speed values, to highlight the peak of the distributions. The IVT peaks show strong scenario differences as before with (436.4 ± 1.7) kg/ms for the historical, (476 ± 2) kg/ms for ssp126 and (561 ± 3) kg/ms for ssp585. IVT peaks are estimated by least-square fitting normal distributions. The projected relative change is roughly 9 % for the ssp126 scenario, where global-mean temperatures rises by (1.45 ± 0.23) K and roughly 28 % for the ssp585 scenario with an

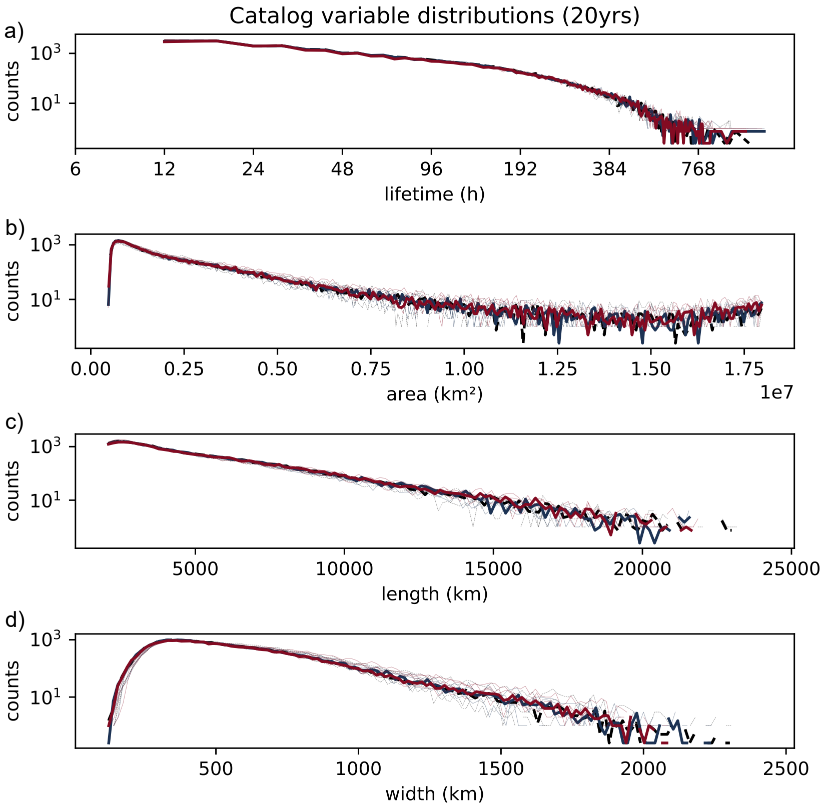

Figure 4.3: Distribution of the first four AR characteristics for the historical (black), ssp126 (blue) and ssp585 (red) scenario. Results for all models are shown along with their scenario ensemble mean in the foreground. All count axis are shown in logarithmic scale and lifetime bins additionally in $\log_2$ scale to highlight possible changes of extremes.

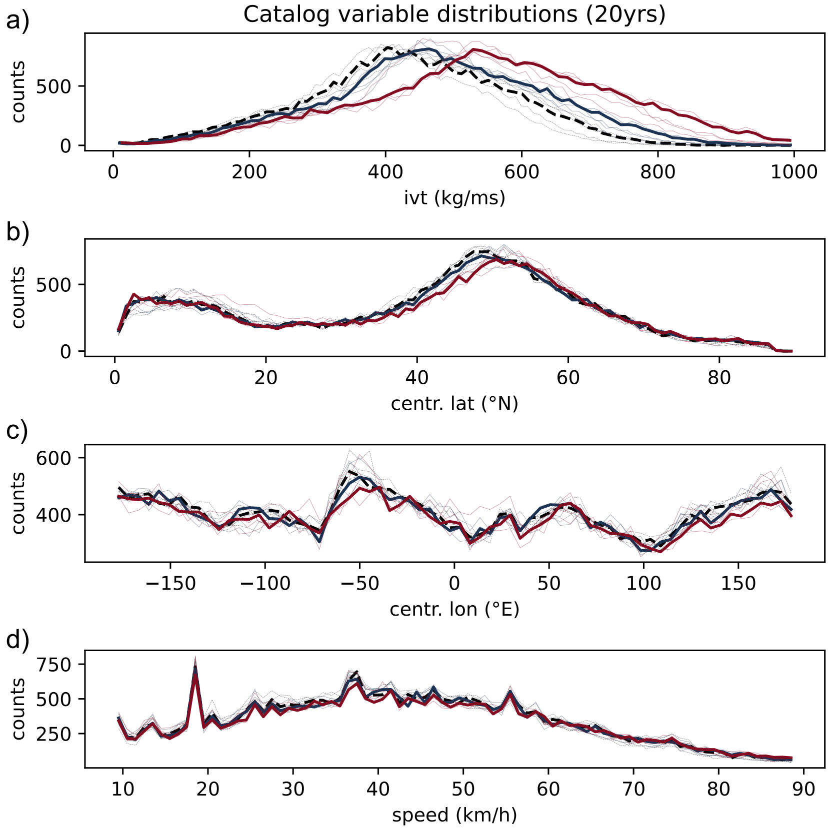

Figure 4.4: Distributions of the last four AR characteristics for the historical (black), ssp126 (blue) and ssp585 (red) scenario. Results for all models are shown along with their scenario ensemble mean in the foreground. Long tails are cut off when no differences are visible to highlight changes in the frequent bins. Every dataset is binned equally. Centroid latitude shows absolute values to increase S/N.

increase in temperature by $(4.30 \pm 0.19)\,\mathrm{K}$. Both temperature differences are estimated from ensemble and area-weighted mean low-frequency changes of near-surface air temperature tas (as calculated and presented in subsection 4.3.1). The measured relative IVT change results in exponential scaling rates of $(6.0 \pm 1.0)\,\%/\mathrm{K}$ and $(5.84 \pm 0.26)\,\%/\mathrm{K}$, when inverting Equation 3.20 and using gaussian error propagation.

ARs usually occur above large water basins where they generate in the west, travel north-eastwards and terminate in the eastern borders of these basins. Absolute values of centroid latitudes show a peak at the expected bands of high water vapor transport in the mid-latitudes and the equator, as explained in section 2.1. A poleward shift in the mid-latitude peak of $(2.0 \pm 0.3)^\circ$ can be seen for the ssp585 scenario, while the shift is less distinct for ssp126 ($(0.5 \pm 0.4)^\circ$). The mean values of mid-latitude peaks are estimated by least-square fitting normal distributions from 30° to 75° with r^2-values of 0.982/0.986/0.990 for historical/ssp126/ssp585. This change cannot be seen in the trend analysis possibly due to global means diminishing the already small signal.

No change can be identified for the centroid longitudes of different scenarios. All distributions show a broad peak at 50°W and 170°E, which aligns well with the active AR regions in the northern Atlantic and northern Pacific, which are further discussed in the next paragraph. Dips are visible for roughly 75°W, 20°E and 100°E, where large land masses span most of the corresponding latitudes.

The AR centroid speed distributions are truncated at 10 km/h by the geometric criteria in the PIKART algorithm and exhibit a broad distribution. Small peaks at approximately 18 km/h, 38 km/h and 56 km/h correspond to AR movement of 1, 2 and 3 grid cells per time step, respectively and are likely associated with short-lived, slow-moving ARs.

4.2.3 Frequency of Atmospheric River Occurrence

ARs show frequent occurrences above oceans, while hardly ever emerging above deserts or regions with high altitude. These regions of high AR activity are well observed and can be replicated with historical AR footprints. Projections are made for the ssp126 and ssp585 scenarios along with the differences to the historical case.

The yearly frequency at which AR conditions occur globally is calculated by counting the number of times a grid cell is covered by an ARs and dividing by the total number of time steps in that year. To increase the signal-to-noise ratio and the projected differences, 10 year averages from 1950 to 1960 and from 2090 to 2100 are made per model. The results are combined in an ensemble mean and shown in Figure 4.5a-b. Areas are cross-hatched where the uncertainty is larger than the frequency.

Uncertainties are estimated by the standard error in 10 year averages and the model spread of predictions. Areas with high uncertainty are where either hardly any ARs occur or where the model predictions are in large disagreement. The first is true in the Himalayas and Antarctica while the second holds mostly for small equatorial ocean areas next to South America.

Resulting dominant AR regions in Figure 4.5a-b reach up to 80 days of AR conditions per year and are all above large water basins. The three major locations are the northern Atlantic, the northern Pacific and the Antarctic Ocean, with the last one being discontinuous. The northern two are shaped elliptically and tilted upwards towards the pole in agreement with the typical life-cycle of ARs. The separate parts of the southern region show the same remarks, but weaker in magnitude. All scenarios show the same overall behavior and magnitude.

A shift in the frequency of AR occurrence is shown in Figure 4.5c as the difference of ssp585 frequencies to the historical case. Notable is that all areas with negative change can be paired with areas of similar magnitude and positive change located further towards the poles. This indicates a poleward shift of AR trajectories most dominant in high activity regions, which can also be seen in the distribution of centroid latitudes in the paragraph above. Regions in Figure 4.5d show the same ssp585-historical difference with cross-hatches where the projected change is smaller than historical variability. Many areas show a significant increase, while a significant decrease is only found in the west of South America. The ssp126 scenario shows the same differences, but weaker in magnitude and projected changes fall below historical variability in most instances.

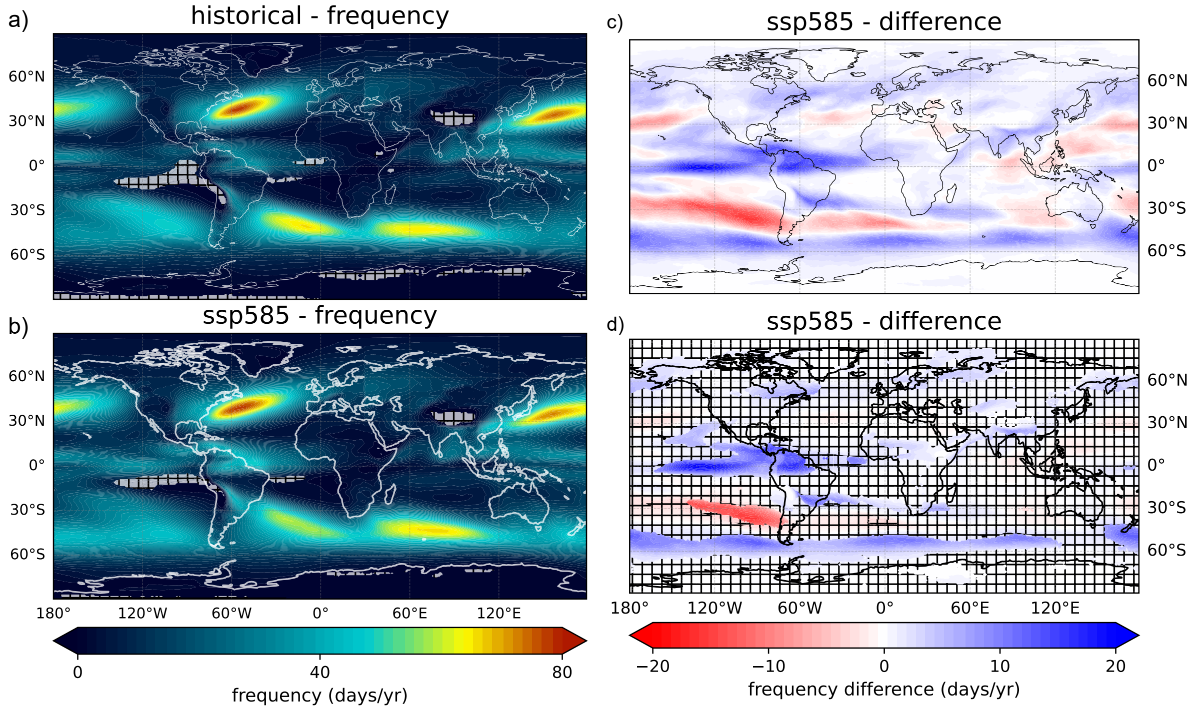

Figure 4.5: Global AR occurrence frequency as ensemble mean of 10-year averages. Results are displayed for a) the historical period from 1950 to 1960 and b) ssp585 from 2090 to 2100. Regions are cross hatched where uncertainties are larger than projections. c) The difference between historical and ssp585 AR occurrences show the projected ensemble mean change and d) the same result, but with areas cross hatched where historical variability surpasses the projected changes.

4.3 Extreme Precipitation Projections

After the analysis of single AR characteristic projections and their dominant regions, another study is performed to evaluate their impact. For this, intensity and frequency of extreme precipitation events are used as impact metrics. The analysis is largely coherent with the work of Kotz et al. 2023 to preserve comparability, but here performed on the three selections of i) all precipitation events (labeled pr) ii) AR caused events (labeled AR) and iii) all except AR caused events (labeled noAR), to determine the projected differences between AR and noAR events while keeping an unaltered result as validation. The separation into AR and noAR events was explained in subsection 3.3.4 with similar association techniques found for example in Michel et al. 2021. The climate change signal is identified first by applying the LFCA method (developed by R. C. Wills et al. 2018 and also applied by Kotz et al. 2023 in the previous study of precipitation extremes) on temperature and extreme precipitation metrics $px1$ and fx. The resulting low-frequency changes of the first patterns are then compared to expectations from Clausius-Clapeyron scaling. A functionality test of all combined methods is first performed on integrated water-vapor transport (IVT), where a closer link to thermodynamic expectations and results of previous studies exist (compare faster AR included IVT in Vallejo-Bernal et al. 2025), to also reinforce the functionality of the AR event separation.

4.3.1 Low-Frequency Changes

This chapter presents the low-frequency changes from LFCA with a cutoff period of $T = 20\,\mathrm{yr}$. The climate change signal is reconstructed from the first pattern by multiplying the spatial low-frequency pattern with the projected temporal evolution of the vary pattern in the low-frequency component.

The global near-surface air temperature is investigated first. Projections for ssp585 are shown in Figure 4.6. The spatial patterns show general similarities across all models. Temperature increases are most dominant in the Arctic and significantly weaker above oceans with agreement across all models and scenarios. Land

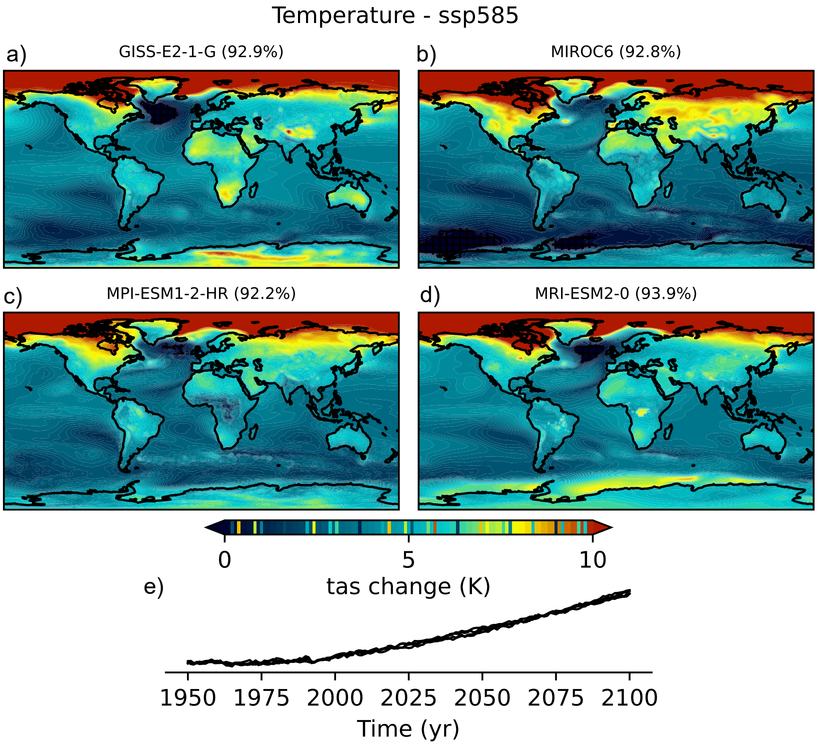

Figure 4.6: a)-d) Low-frequency change of global near-surface air temperature for the ssp585 scenario. Changes are displayed for all four models as the product of the patterns with the far-future difference in their temporal evolution. The pattern's share of variability to total spatiotemporal variability is shown along with the model name. e) The temporal evolutions are overlain for all models to show their similarity. Regions are cross-hatched, where the projected change is smaller than the variability between 1950 and 1970. Results for ssp126 are shown in the appendix.

grid cells heat up faster than ocean cells, but locations alter strongly between models. The spatiotemporal variability in the first pattern accounts for almost all variability with $> 92\,\%$ for all models. Changes in the ssp126 scenarios are predominantly similar, but lower in magnitude. All changes are significant with respect to historical variability. Strong coherence exists in the temporal evolution for both scenarios and across models. The total ensemble mean and area-weighted temperature increase is $(1.45 \pm 0.23)\,\mathrm{K}$ and $(4.30 \pm 0.19)\,\mathrm{K}$ for ssp126 and ssp585, respectively.

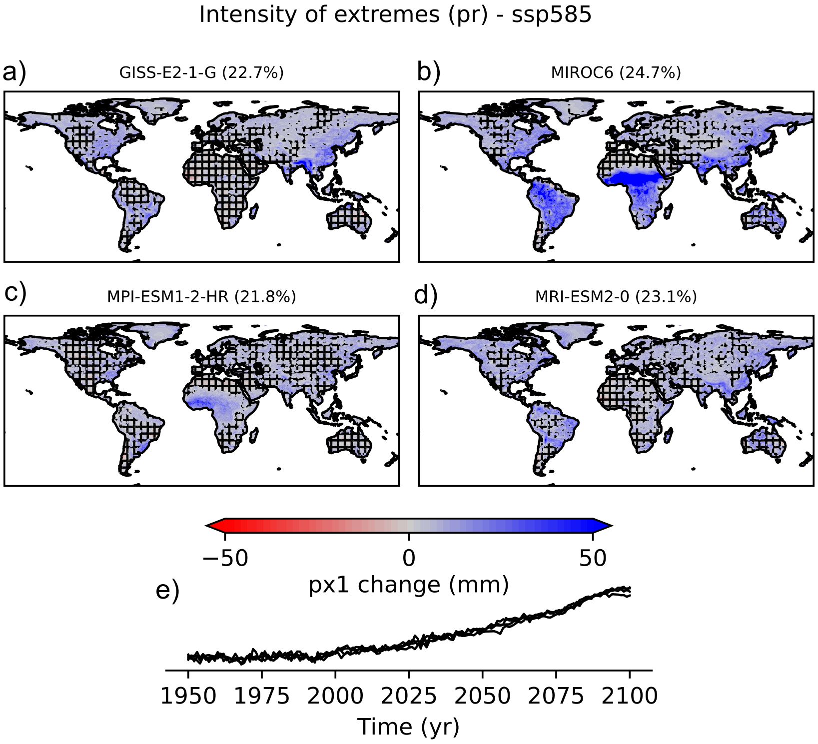

Figure 4.7: As in Figure 4.6 but for low-frequency change of extreme precipitation intensity of all precipitation events (pr) for the ssp585 scenario. Regions are cross-hatched, where the projected change is smaller than the historical variability between 1950 and 1970. Results for ssp126 and AR/noAR events are shown in the appendix.

Changes in the extreme precipitation metrics are analyzed on land without the Antarctica. The continent is ruled out because it is poorly modeled, uninhabited, lacks infrastructure and a desert, making it unfit for precipitation impact studies. The following analysis focuses on ssp585 results for all events. The scenario ssp126 and the selections of AR and noAR events produce equal results per model, but weaker magnitudes.

The low-frequency change in ssp585 of the intensity of annual extreme precipitation is displayed in Figure 4.7a-d for all models and pr events. Again, the temporal pattern evolutions show strong coherence, whereas the spatial patterns disagree strongly on the location and magnitude of changes between models. The first patterns include $> 17.8\,\%$ of total variability. Changes remain smaller than historical variability in many regions and are cross hatched in Figure 4.7a-d. Areas with significant change are mostly close to the equator, where the magnitude of changes is also larger. The general trend is positive with an area-weighted, ensemble mean change of $(9 \pm 4)\,\mathrm{mm}$. For comparison: AR-caused events predict the least absolute global mean change with $(6.8 \pm 2.3)\,\mathrm{mm}$, while noAR events predict $(8 \pm 3)\,\mathrm{mm}$ in the ssp585 scenario.

Changes in the frequency of extreme precipitation events are shown for ssp585 in Figure 4.8a-d for all models and pr events. Again, the temporal evolution shows strong coherence between models, while the spatial patterns differ in shape and magnitude. The first pattern accounts for $23.6\,\%$ of total variability. Historical variability is greater than projected changes in many areas, which is again shown as cross hatched regions. Significant changes are found in Greenland, northern North America, nearly all of Asia and equatorial Africa. Strong agreement exists in the projection of Greenland and north-east Asia, while magnitudes of change are largest close to the equator. The general trend is again positive, with an

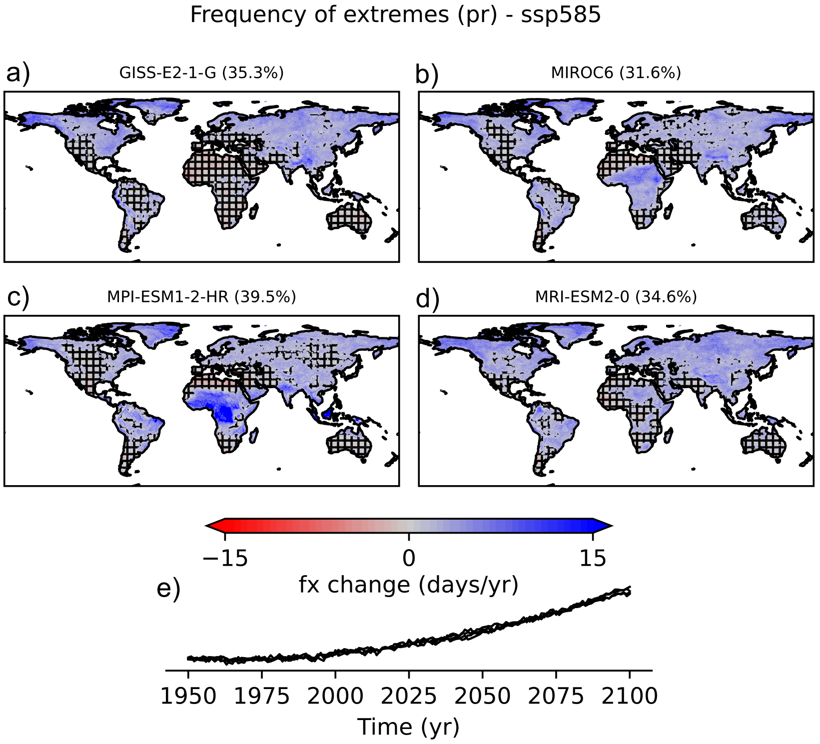

Figure 4.8: As in Figure 4.6 but for low-frequency change of extreme precipitation frequency of all precipitation events (pr) for the ssp585 scenario. Regions are cross-hatched, where the projected change is smaller than the historical variability between 1950 and 1970. Results for ssp126 and AR/noAR caused events are shown in the appendix.

ensemble mean area-weighted change of $(2.5 \pm 0.5)\,\mathrm{d/yr}$. Global mean AR events change significantly less with $(0.64 \pm 0.13)\,\mathrm{d/yr}$ and noAR events with $(1.9 \pm 0.4)\,\mathrm{d/yr}$. In the case of extreme frequencies, the events are summed up per year. The change in pr events is therefore similar to the sum of AR and noAR events, which is represented well in the global means. The absolute frequency increase therefore originates mostly from noAR caused precipitation.

4.3.2 Scaling of Integrated Water-Vapor Transport

Projections of integrated water-vapor transport (IVT) are expected to increase closely with Clausius-Clapeyron scaling, because IVT values are closer linked to specific humidity and therefore to the thermodynamic equations, while precipitation is subject to larger dynamical contributions. IVT is also necessary for AR detection and therefore already available, which makes it the perfect testing dataset for the defined methods on extreme intensities. However, the frequency of extremes cannot be tested adequately, because the expected value taken from Kotz et al. 2023 is calculated by scaling up the historical distribution of precipitation with $7\%/K$, which does not directly translate to IVT.

The same implementations to calculate the extreme metrics, LFCA and the scaling rates are used on IVT data, which are later applied on precipitation extremes. The remaining differences are firstly the 6 h temporal resolution of IVT, while precipitation is aggregated daily. Therefore, AR shapes do not have to be combined into larger daily shapes before matching them with IVT extremes. And secondly, the global evaluation of IVT instead of land-averages, to exclude regionally different feedback. The analysis is performed for all IVT (here labeled "ivt" instead of "pr" to prevent confusion with precipitation), IVT included in ARs (AR) and IVT outside of ARs (noAR). Both event separations are executed with the same methods described in subsection 3.3.4.

Scaling rates for extreme IVT events are obtained by estimating extreme intensity and frequency as described in subsection 3.2.2 and by least-square fitting Equation 3.20 on relative changes as described in

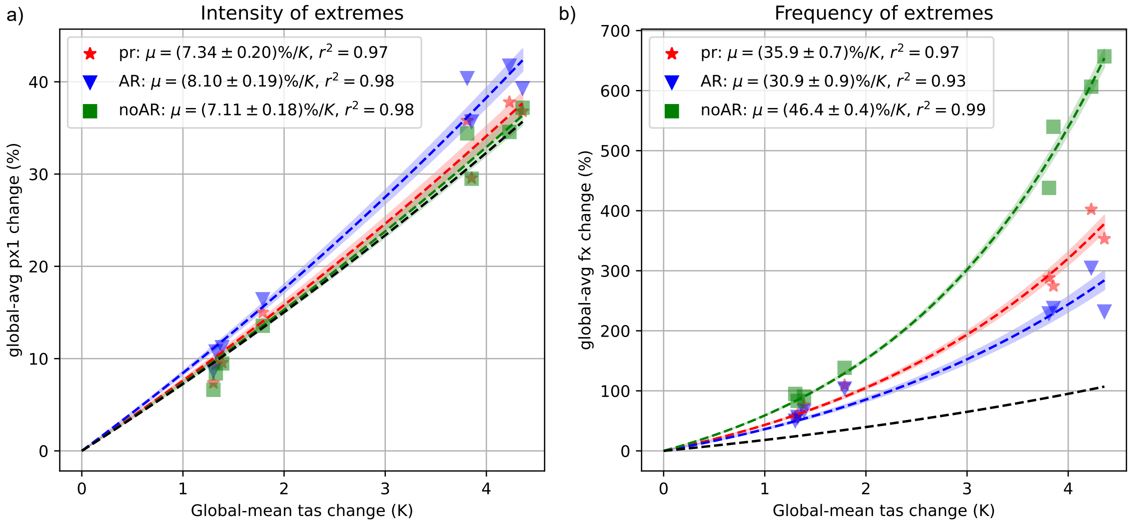

Figure 4.9: Exponential scaling rates for the relative change of a) annual extreme IVT intensity and b) extreme IVT frequency. Changes are calculated as the product of land-averaged area-weighted patterns with their temporal evolutions and divided by the historical reference from 1950 to 1970. Zeroes and very small values are excluded from both reference and area. Resulting changes are averaged over the period from 2090 to 2100 and plotted against global-mean surface-air temperature (tas) for both ssp126 and ssp585. Dashed lines show the results of least-square fits from Equation 3.20 with shaded uncertainty-bands for ivt (red), AR (blue) and noAR events (green). Coefficients of determination (r^2) are shown along with scaling rate results in the legend. The black line represents scaling expectations for precipitation from Clausius-Clapeyron.

section 3.5. Global area-weighted means of the last 10-years are averaged to produce one far-future result per scenario, model and event selection.

The results for extreme IVT intensities are displayed in Figure 4.9a and increase with $(7.33 \pm 0.20)\,\%/\mathrm{K}$, $(8.10 \pm 0.19)\,\%/\mathrm{K}$ and $(7.11 \pm 0.18)\,\%/\mathrm{K}$ for ivt, AR and noAR, respectively. Especially the AR scaling rate is significantly larger than the expectation and the scaling of noAR events, with agreement across all models.

Frequencies of extreme IVT scales significantly more strongly than the expectation of extreme precipitation frequencies with $(35.9{\pm}0.7)\,\%/\mathrm{K}$, $(30.9{\pm}0.9)\,\%/\mathrm{K}$ and $(46.4{\pm}0.4)\,\%/\mathrm{K}$ for ivt, AR and noAR, respectively. Changes and scaling rates are displayed in Figure 4.9b. Events without AR-link scale the fastest, while AR caused events scale significantly slower. Inter-model agreement on scaling rates are large for both intensity and frequency with coefficients of determination > 0.93 for all rate estimations.

4.3.3 Scaling of Precipitation Extremes

The first patterns of low-frequency change in surface air temperature tas, annual extreme precipitation intensity $px1$ and frequency of extreme precipitation fx increase strongly in time. Here, the scaling rates of relative changes with temperature are determined and compared to thermodynamic expectations.

First, the relative change is calculated per grid-cell with a fixed historical reference from 1950 to 1970, as described in section 3.5. Figure 4.10 shows a ten-year average of relative changes in the far-future (2090-2100) in analogy to the work of Kotz et al. 2023 for both ssp126 and ssp585. To test robustness, a period of 20 yr was also evaluated, yielding similar results as the 10 yr period analysis. Uncertainties result from the corresponding covariance of least-square fitting Equation 3.20. The intensity of all extreme precipitation events (pr) scales with $(5.8 \pm 0.5)\,\%/\mathrm{K}$ which aligns with the lower limit of the $6\,\%/\mathrm{K}$ to $7\,\%/\mathrm{K}$ expected from Clausius-Clapeyron scaling. AR events scale faster with $(7.7 \pm 1.1)\,\%/\mathrm{K}$ but also with increased model variability. noAR events scale the slowest with $(5.3 \pm 0.5)\,\%/\mathrm{K}$ and show similar model spread as all events.

The frequency of extreme precipitation events scale with $(12.4 \pm 0.9)\,\%/\mathrm{K}$, $(17.2 \pm 2.9)\,\%/\mathrm{K}$ and $(12.5 \pm$

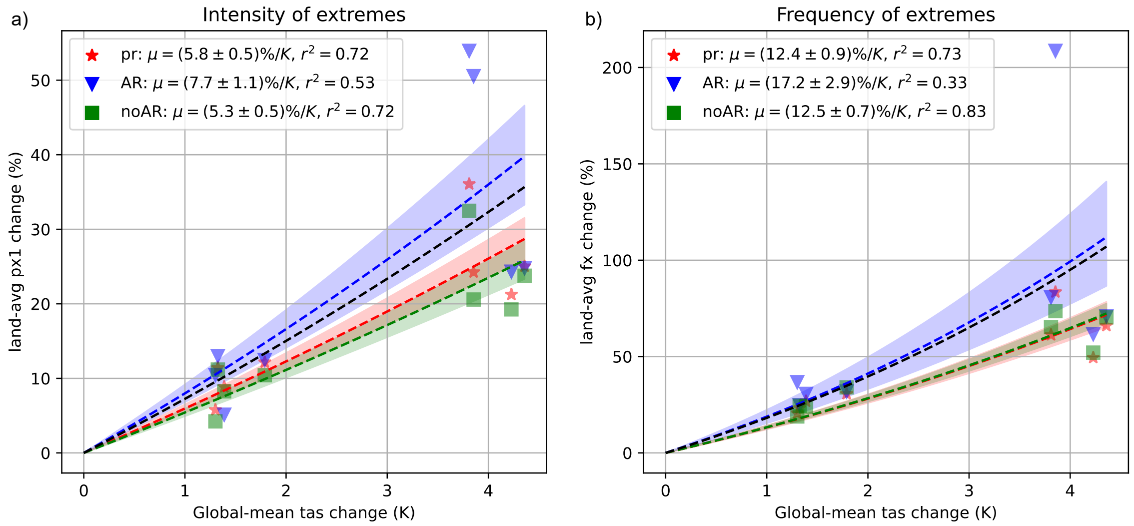

Figure 4.10: Exponential scaling rates for the relative change of a) extreme precipitation intensity and b) extreme precipitation frequency. Changes are calculated as the product of land-averaged patterns with their temporal evolutions and divided by the historical reference from 1950 to 1970. Zeroes and very small values are excluded from both reference and area. Resulting changes are averaged over the period from 2090 to 2100 and plotted against global-mean surface-air temperature (*tas*) for both ssp126 and ssp585. Dashed lines show the results of least-square fits of Equation 3.20 with shaded uncertainty-bands for pr (red), AR (blue) and noAR events (green). Coefficients of determination (r^2) are shown along with scaling rates in the legend. The black line represents expectations from Clausius-Clapeyron.

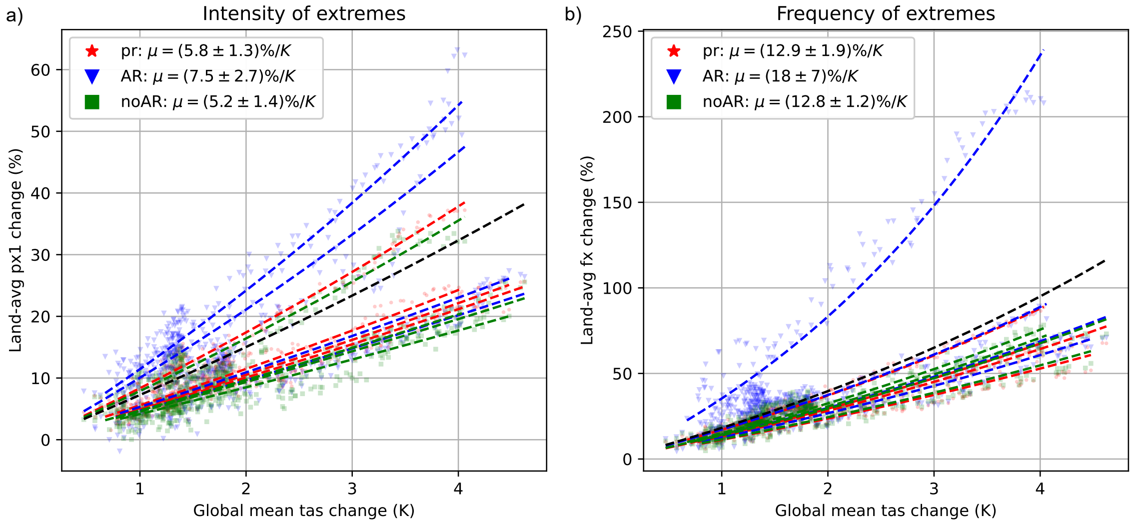

Figure 4.11: Exponential scaling rates for the relative change of a) extreme precipitation intensity and b) extreme precipitation frequency. Changes are calculated as the product of land-averaged patterns with their temporal evolutions and divided by the historical reference from 1950 to 1970. Zeroes and very small values are excluded from both reference and area. Each dot represents one year with its global-mean temperature and change estimation. Points of all models are shown, each with a least-square fit of Equation 3.20 on points of both scenarios. Dashed lines show the result of the best estimate of exponential scaling parameters per model for pr (red), AR (blue) and noAR events (green). The ensemble mean scaling rates with uncertainties from model spread can be seen in the legend. All resulting rates are listed in Table 4.1 and Table 4.2. The black line represents expectations from Clausius-Clapeyron.

0.7) %/K for pr, AR and noAR events, respectively. Here, the pr and noAR scaling falls significantly below the expected 16.7 %/K. The coefficient of determination (r^2) remains low for both metrics with values ranging from 0.33 to 0.83. The lowest coefficient occurs for AR caused scaling due to the large projected discrepancy between models. AR caused events scale faster, but uncertainties are again large mostly due to model spread.

Intensity of extremes

model	pr	AR	noAR
GISS-E2-1-G	5.00 ± 0.07 ($r^2 = 0.74$)	5.18 ± 0.10 ($r^2 = 0.53$)	4.07 ± 0.07 ($r^2 = 0.71$)
MIROC6	8.02 ± 0.05 ($r^2 = 0.97$)	9.57 ± 0.16 ($r^2 = 0.80$)	7.60 ± 0.07 ($r^2 = 0.94$)
MPI-ESM1-2-HR	5.43 ± 0.05 ($r^2 = 0.95$)	10.83 ± 0.08 ($r^2 = 0.96$)	4.62 ± 0.04 ($r^2 = 0.95$)
MRI-ESM2-0	4.80 ± 0.05 ($r^2 = 0.92$)	4.60 ± 0.07 ($r^2 = 0.83$)	4.47 ± 0.06 ($r^2 = 0.87$)
Diff. to AR	1.7 ± 2.2	–	2.4 ± 2.3
Ensemble Mean	5.8 ± 1.3	7.5 ± 2.7	5.2 ± 1.4

Table 4.1: Exponential scaling rates for the intensity of extreme precipitation. Values originate from least-square fitting Equation 3.20 and errors from the corresponding covariance matrix. A coefficient of determination (r^2) is given in parenthesis. The ensemble mean rates and the ensemble mean difference to AR rates are listed for each event selection with uncertainties from model spread. All scaling rate units are in %/K.

Frequency of extremes

model	pr	AR	noAR
GISS-E2-1-G	10.61 ± 0.16 ($r^2 = 0.56$)	11.86 ± 0.19 ($r^2 = 0.61$)	10.91 ± 0.17 ($r^2 = 0.58$)
MIROC6	12.89 ± 0.09 ($r^2 = 0.94$)	15.89 ± 0.20 ($r^2 = 0.82$)	13.39 ± 0.09 ($r^2 = 0.95$)
MPI-ESM1-2-HR	15.78 ± 0.06 ($r^2 = 0.99$)	30.29 ± 0.23 ($r^2 = 0.94$)	14.08 ± 0.07 ($r^2 = 0.98$)
MRI-ESM2-0	12.41 ± 0.14 ($r^2 = 0.81$)	13.08 ± 0.17 ($r^2 = 0.77$)	12.92 ± 0.14 ($r^2 = 0.82$)
Diff. to AR	4.9 ± 6.4	–	5.0 ± 7.2
Ensemble Mean	12.9 ± 1.9	18 ± 7	12.8 ± 1.2

Table 4.2: Exponential scaling rates as in Table 4.3, but for the frequency of extremes. All scaling rate units are in %/K.

A second approach calculates the relative changes as before, but keeps the global/land-averaged values of all years to compensate the small number of samples (i.e. number of models and scenarios). This allows for a more stable scaling rate estimation per model and an ensemble mean scaling rate with uncertainties resulting from model spread. The results for extreme precipitation intensities along with an ensemble mean rate are shown in Figure 4.11a, while individual scaling rates per model are listed in Table 4.1. The ensemble mean scaling rates of (5.8 ± 1.3) %/K, (7.5 ± 2.7) %/K and (5.2 ± 1.4) %/K for pr, AR and noAR events align well with previous results, but show increased uncertainties. Again AR caused events scale faster than pr and noAR events, but no longer significantly due to the large model spread. Nevertheless, all models predict a larger scaling rate for AR caused events than for noAR events. Coefficients of determination have increased overall and differ mainly between models, but smaller values for AR events are common (s. Table 4.1 and Table 4.2).

The scaling of extreme precipitation frequencies are shown in Figure 4.11b and results in ensemble mean rates of (12.9 ± 1.9) %/K, (18 ± 7) %/K and (12.8 ± 1.2) %/K for pr, AR and noAR events, respectively. Again, the scaling rates are comparable to those determined previously and to expectations, but with larger estimated uncertainties. Individual scaling results per model can be seen in Table 4.2. The model MPI-ESM1-2-HR falls out of line with especially large projections for AR caused events, resulting in major contributions to the total uncertainty. Excluding this model would results in an AR rate of (13.6 ± 1.7) %/K. Both AR rates are not significantly larger than pr and noAR events, even though all models simulate larger rates for AR events. Coefficients of determination are smaller for the model GISS-E2-1-G with $r^2 \in [0.56, 0.74]$, but larger for all others with $r^2 > 0.77$ compared to the previous 10 yr average analysis.

The least-square fitted scaling rates of annually estimated extremes for individual models can additionally be found in Appendix C for both intensity and frequency of extremes to increase visibility of single model results.

Although the results here are already similar to those of Kotz et al. 2023, another evaluation is performed with a running-average to further validate and compare the results. This has the benefit that only data for those years are used which are available in this work as well and prevents an impact of different historical reference periods. Additionally, 3/4 of models used here have also been used in Kotz et al. 2023, which makes results of pr event directly comparable.

	a) Intensity of extremes			**b) Frequency of extremes**		
Model	This work	Kotz et al. 2023		This work	Kotz et al. 2023	
GISS-E1-1-G	(5.11 ± 0.29)	-	×	(9.7 ± 0.6)	-	×
MIROC6	(7.8 ± 0.3)	(6.87 ± 0.50)	×	(12.4 ± 0.3)	(10.99 ± 1.00)	×
MPI-ESM1-2-HR	(4.95 ± 0.25)	(5.13 ± 0.75)	✓	(13.7 ± 0.5)	(14.77 ± 2.50)	×
MRI-ESM2-0	(4.9 ± 0.3)	(4.88 ± 0.50)	✓	(12.6 ± 0.6)	(12.46 ± 2.00)	✓
Ensemble Mean	(5.7 ± 1.3)	(6.1 ± 1.4)	✓	(12.1 ± 1.6)	(12.0 ± 3.6)	✓

Table 4.3: Linear scaling rates for all events (pr) for findings in this work in comparison to those taken from Kotz et al. 2023 (supplemented material) with estimated errors, since numbers are not given. Values are displayed for a) the intensity and b) the frequency of extreme precipitation. The ensemble mean from Kotz et al. 2023 refers to the total ensemble and not to the selection shown here. A third column shows either a tick or a cross, depending if the determined rate aligns with the one from Kotz et al. 2023. Units are in %/K.

The running mean is performed on pairs of 30-year separated non-overlapping decades. For both decades, the climate change signal is identified as the first low-frequency component. The reconstruction is calculated from the product of the first spatial pattern and its temporal evolution. The two decades are averaged as before with area weights over land without the Antarctica and their difference is expressed relative to the first decade. Temperature changes are the global area-weighted means of tas differences. The results for ssp126 and ssp585 are joint and least-square fitted with the linear function $f(x) = m \cdot x$ (and therefore called linear scaling rates, in contrast to the exponential scaling rates before). Again, the rates are determined for all events (pr), AR caused events (AR) and all except AR caused events (noAR).

Individual findings for the intensity of extreme precipitation are displayed in Figure 4.12. The ensemble mean rates are (5.7 ± 1.3) %/K for pr, (6.6 ± 1.9) %/K for AR and (5.3 ± 1.5) %/K for noAR. Uncertainties originate from model spread and are again larger than projected differences between the event selections. Individual AR rates per model are again larger than noAR rates, but the differences is not significant due to the high uncertainty.

The linear scaling rates for frequency of extremes are shown in Figure 4.13. The resulting ensemble mean rates are (12.1 ± 1.6) %/K for pr, (14 ± 5) %/K for AR and (12.5 ± 1.5) %/K for noAR events. Again the model spread is large with no significant differences between pr, AR and noAR events. The model MPI-ESM1-2-HR contributes strongly to the uncertainty of AR events by predicting an exceptionally high rate and shows increased internal variability compared to pr and noAR events or other models projection of AR events.

A comparison to the linear scaling rates in the work of Kotz et al. 2023 can be found in Table 4.3 for the analysis of all events (pr). Two of the three models align for the intensity of extremes, when evaluating the self determined values with their uncertainties against the rates in Kotz et al. 2023. Only one of the three models aligns for the frequency of extremes. The model MIROC6 does not align for both metrics and includes the largest discrepancy. Differences between this work and Kotz et al. 2023 can already be found in the first LFCA pattern of MIROC6, where the projection of extreme precipitation intensity (s. Figure 4.7) in South America shows a strong positive development here and a minor negative trend in Kotz et al. 2023. A possible reason for this difference could be the use of a different variant label and therefore different initial conditions in the model simulation, or a difference in the climate change signal identification. Because of the limitation to land areas, this regional difference could explain the larger scaling rates for this model. The ensemble mean values are comparable in both cases.

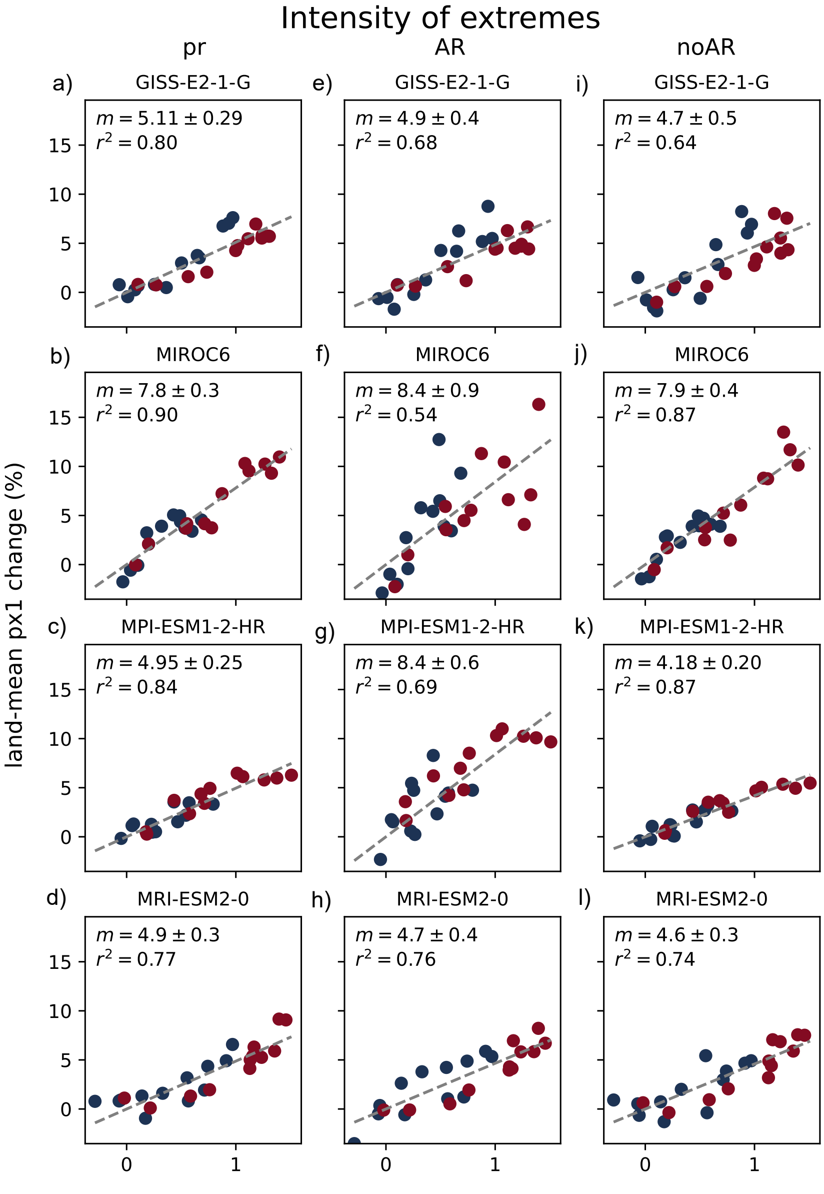

Figure 4.12: Individual scaling rates of extreme precipitation intensities. a)-d) shows results for all events (pr), e)-h) for AR-caused events and i)-l) for all except AR-caused events (noAR). Pairs of 30-year separated non-overlapping decades are analyzed. Temperature changes are the differences of 10-year averaged global-mean low-frequency reconstructions from tas LFCA results per pair. Relative changes are estimated by calculating the difference as for temperature and dividing by the first decades average. Resulting values for ssp126 and ssp585 are shown in blue and red, respectively. A linear least-square fit is shown in gray with the optimal rate and r^2-value. Uncertainties result from the corresponding covariances.

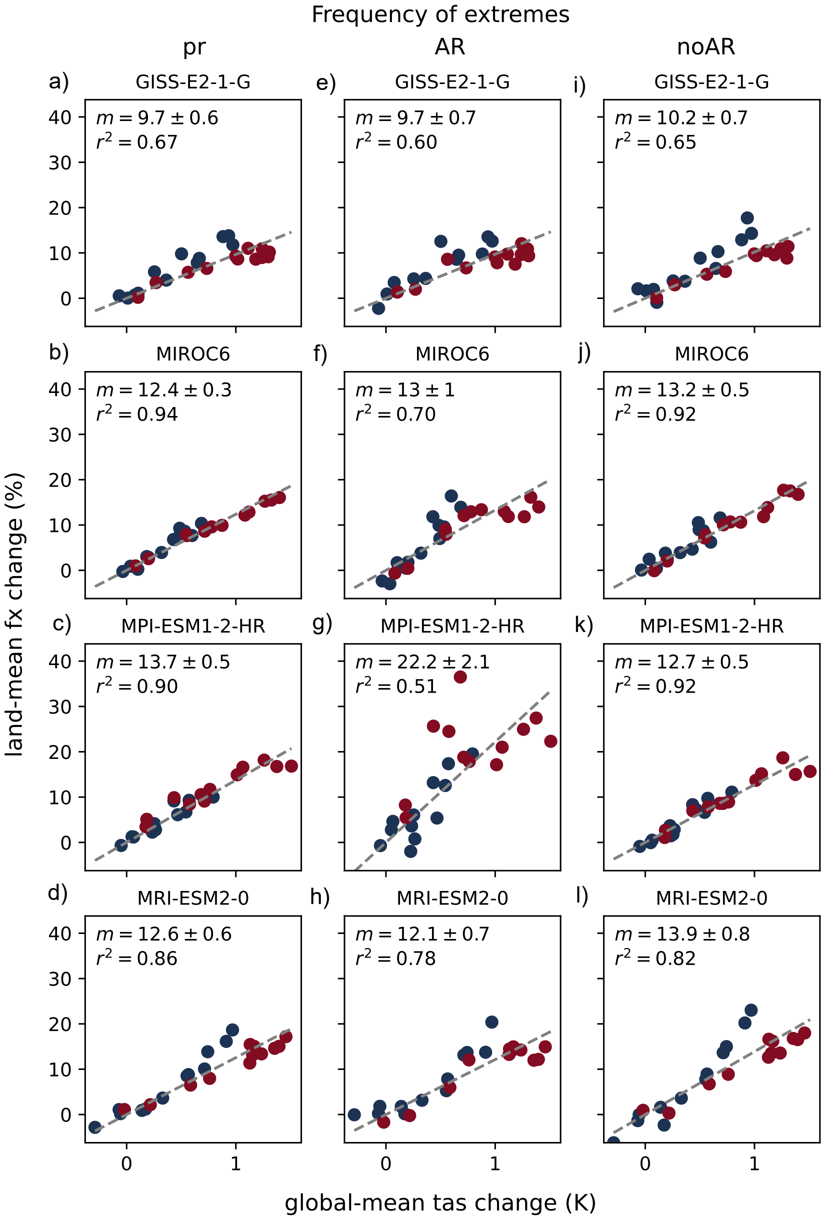

Figure 4.13: As in Figure 4.12 but for extreme precipitation frequency.

Chapter 5

Discussion

The plentiful results of the previous chapter are now consolidated, interpreted and put in comparison to the literature. First, a short summary repeats key findings of the results, which are then interpreted in the following two sections. Afterwards, different contributions to result uncertainties are regarded, followed by a sensitivity discussion, a comparison of results to previously findings in the literature, a specific focus on the general implications of results and an insight into methodological limitations of this study. Finally, ideas are presented on how to proceed and overcome these limitations.

5.1 Summary

In this work, the PIKART algorithm was tested on a small subset of observational-consistent data to evaluate the resolution sensitivity and to choose spatial and temporal resolutions for the following analyses. An optimum has been chosen, which preserves AR tracks while simultaneously trying to minimize the necessary data volume. The algorithm was then applied on four general circulation models, each for two different emission scenarios and a historical run. AR characteristic metrics were then analyzed for their link to global temperature and for changes in their distribution. Most metrics did not show significant or only minimal changes, while the mean integrated water-vapor transport of ARs increased distinctly with roughly estimated rates as expected from Clausius-Clapeyron and a poleward shift of AR tracks in the mid-latitudes.

The global frequency of AR occurrence was estimated by overlapping AR shapes. Dominant regions were identified over all major oceans with a poleward shift for ssp585. Only some areas projected changes that are stronger than the historical variability.

The climate change signal was identified for near-surface air temperature, intensity and frequency of extreme precipitation. The temperature showed strong agreement between models with major increases at the North Pole. Less coherence existed on land areas. Intensity and frequency showed an overall increase, but a large spread between models on magnitude and location.

The scaling rates for intensities, determined from the previously identified climate change signals, aligned well with Clausius-Clapeyron expectations, but uncertainties are large. Scaling of AR-caused extremes compared to non-AR events were larger in all models, but not significantly due to the large inter-model spread, while noAR events overall scaled with similar rates as all events.

Extreme precipitation frequencies scaled in most cases significantly slower than the expectation from scaling up historical distributions. AR caused events again scaled faster than noAR events in all models and the large uncertainty again originates from inter-model spread. The ensemble mean rates showed no significantly faster scaling for the AR event selection.

5.2 Interpretation of Projected Catalog Changes

The projected catalog changes can be summarized by an increase in AR intensity and a poleward shift, while all other metrics showed little to no significant change.

The intensity of an AR is accessed by its amount of integrated water-vapor transport, which increases significantly with strong agreement between models. The different changes for the two scenarios are explained by Equation 2.24, since the first scenario projects only a weak and the latter a strong radiative forcing. Both increased rates for the ssp126 and ssp585 scenario coincide with the lower limit of the thermodynamic expectation, which agrees with a strong thermodynamic contribution. The absent changes in the other metrics might support this assumption, as strong shifts in the dynamics could potentially be detectable in in the temperature dependence of AR characteristics or in their distributions.

The second robust projection is the poleward shift of mid-latitude AR trajectories, which could be observed for the ssp585 scenario, while ssp126 results showed only minor changes. This can not be explained by thermodynamic changes, since increased moisture availability does not directly relate to the latitude position of AR tracks. However, it has been found in previous studies that a warmer climate increases the size of the equatorial Hadley Cell. The dynamics in the mid-latitudes are largely driven by the equator-pole heat flux, which could reduce in a high emission scenario because of the strong temperature amplification in the Arctic which could partially level the temperature gradient. However, this strong regional amplification does not occur in the Antarctica, where the effect should therefore not be visible. A north/south separation of the effect has not been made. The collapse of the equatorial Hadley Cell marks the beginning of the mid-latitude region, where the dynamics of atmospheric rivers are embedded in. A larger Hadley Cell could therefore shift the whole mid-latitude region poleward and therefore also the included AR tracks. This would also align with the stable equatorial AR tracks, where no shift to higher latitudes could be observed. The weaker poleward shift in the ssp126 scenario can be explained by the weaker back radiation, which impacts the Hadley Cell by a smaller amount and the effect is therefore less distinct.

In the active AR regions, elliptically shaped dominate regions have been found in the mid-latitude above oceans with small poleward tilt. This aligns well with the theory, where ARs are expected to emerge subject to the complex dynamics in the mid-latitude region between the collapse of the equatorial and polar Hadley Cells. AR tracks embedded in the north-east trade winds would create the north-east tilted ellipses by small fluctuations in their size and starting location. The observed poleward shift of these regions, with a smaller insignificant shift for the ssp126 scenario and a stronger shift for the ssp585 scenario aligns well with the previously observed poleward shift in centroid latitudes.

5.3 Scaling Rates of Precipitation Extremes

The intensity of extreme precipitation events are linked to the available moisture in the atmosphere, where the robustness check showed an increase in extreme integrated water-vapor transport (IVT) slightly above expectations from Clausius-Clapeyron. This supports the assumption that an increase in available moisture increases extreme IVT consistent with a strong thermodynamical contribution, since IVT is governed by both humidity and wind speed. The significantly faster scaling of IVT within ARs may reflect additional dynamical contributions. Although AR lifetime and spatial characteristics remained largely unchanged, circulation changes could still modify moisture transport efficiency through altered convergence or transport pathways and therefore contribute to enhanced AR-IVT intensity scaling.

The frequency of extreme IVT events scaled significantly faster than intensities and fastest for noAR events. This reflects a shift in the IVT distribution relative to the historical threshold of extremes in a warmer climate. The threshold exceedance probability depends on the distributional shift of humidity and wind speed and their regional differences. Since the threshold is defined per grid cell, the strong increase in humidity for warmer climates in the tropics could affect the noAR-IVT frequency scaling, while ARs occur mainly in mid-latitudes with different dynamics. However, the tropical and mid-latitudinal humidity differences probably do not explain the whole difference, but changes in local moisture cycles might also contribute. Another possible contribution is that the low sample size of ARs could reduce the number of extreme events and biases the estimates towards lower values.

The intensity of extreme precipitation events showed a clear increase with temperature, which can be seen in the difference of ssp126 and ssp585 results. Similar IVT scaling rates and theoretical expectations again agree on a strong thermodynamic contribution of this change. Even tough large uncertainties remain, a possible faster scaling of AR-associated compared to noAR events can be inferred from faster scaling predicted in all models. Faster AR-IVT scaling increases the available moisture and can contribute to heavier precipitation. Nevertheless, all extreme precipitation intensity changes for pr, AR and noAR events scaled slower than corresponding IVT rates. The scaling of precipitation below the expectations from Clausius-Clapeyron is consistent with the fact that precipitation extremes additionally depend on dynamical processes like the vertical ascent of air, cloud microphysics or the formation of storms, which are not guaranteed to intensify at similar rates. Differences between land-only and global averages might further contribute, since high humidity and larger IVT values usually occur above oceans. Another reason for scaling rates below the Clausius-Clapeyron expectation is the inhomogeneous distribution of temperature increases, while the analysis uses constant global-mean temperatures as reference for all grid cells. Temperatures are expected to increase the strongest at the North Pole and the analysis is limited to precipitation events on land. This difference could lead to slightly over-estimated global-mean temperature projections on many land areas, which then result in smaller scaling rates.

Some models also projected scaling rates above those from Clausius-Clapeyron. While thermodynamics does give an upper boundary for saturation pressure increase, this does not hold for condensation rates, cloud and storm formation, or the efficiency of converting moisture into rain. Larger scaling rates can therefore originate from additional dynamical aspects. The global increase in temperatures could impact regionally dependent dynamics and allow for faster scaling than expected from thermodynamics alone. A faster rate is also mostly projected for AR events, where dynamics play a crucial role.

In contrast to the extreme IVT frequency rates, the frequency of extreme precipitation events was mostly largest for AR-associated events. Moreover, the precipitation scaling rates are generally smaller than the corresponding IVT scaling rates. A higher IVT frequency does not automatically lead to a higher precipitation frequency, because high humidity and IVT values do not automatically imply precipitation. Extreme precipitation also depends on the vertical rise of air and storm formation, which is largely dynamically driven and might not increase at the same rate. One model projected significantly larger scaling of its AR-associated events and dominated inter-model spread. All other models also showed larger scaling of AR compared to noAR associated events, but overall the difference remained smaller than inter-model variability.

The scaling of extreme precipitation frequency falls significantly below the expected rate in most cases, even though the estimated changes are presumably biased towards larger values, since regions with historically zero frequency prevent the determination of changes and had to be excluded. A possible explanation is that the assumption of a uniform precipitation up-scaling does not hold. Even if the precipitation intensities increase as expected, the exceedance probability of a historical threshold still depends heavily on the shape of the distribution, changes in its tail and on storm dynamics. The extreme frequency must therefore not necessarily follow the same rate as an up-scaled historical distribution.

5.4 Model Spread and Uncertainty

As introduced before, the uncertainty can be broadly decomposed into internal variability, structural/model variability and scenario variability. For far-future projections, scenario variability typically dominates, followed by model variability. Different analyzed metrics are subject to different underlying processes and can have stronger or weaker contributions from each of the three sources. This section discusses the model spread of results and possible origins of their estimated uncertainties.

AR catalog characteristics exhibited large year-to-year variability, primarily reflecting internal variability. Nevertheless, great coherence existed in multi-model results. Since most metrics showed no temperature sensitivity, both model and scenario variability played only a minor role. In the same manner, the distributions of AR metrics between models hardly deviated. An additional ensemble mean strongly reduced the variability, with robustly identified changes. Multi-decadal averages reduced the contribution from internal-variability, leaving only small remaining fluctuations.

The projected changes for both intensity and frequency of integrated water-vapor transport (IVT) showed large agreement between all models, presumably because the dominant change is governed by well-established thermodynamic relationships represented consistently across general circulation models and therefore directly simulated without many disturbances from complex dynamics or different structural parameterizations. The remaining fluctuations are mainly caused by internal variability, because scenario differences primarily modulate the magnitude of warming, which translates into comparatively predictable thermodynamic changes via the Clausius-Clapeyron equation. IVT values are largely controlled by large-scale moisture increases rather than by small parameterized processes, which makes inter-model spread comparatively limited.

In contrast, extreme precipitation projections are influenced by a wider range of processes, including cloud microphysics, convection, and sub-grid variability, which are parameterized differently across models and increase the model variability. Precipitation extremes are also strongly modulated by circulation variability, leading to larger internal variability compared to thermodynamically constrained variables such as IVT. The global distributions and magnitudes of changes varied strongly across models, which showed in the climate change signal identification and in the resulting scaling rates. However, the sign of changes was consistent across models, with positive, weaker increase for the ssp126 and positive, stronger increase in the ssp585 scenario. Additionally, all models indicated stronger scaling for AR-associated events relative to noAR events, although the magnitude of this difference varied. The low count of AR events in many regions further increased the variability of AR caused events, possibly leading to substantial sampling uncertainty and increased variance in scaling estimates.

The individual estimation of extreme precipitation scaling rates per model already showed large internal variability for some models and even larger variability when comparing the results between them. Uncertainties estimated from the covariance of least-square fitting are probably overly confident, with values roughly half the size of uncertainties from model-spread. Uncertainty estimates based on inter-model spread more realistically capture unknown temperature dependencies in many processes and include this structural difference between models. They are additionally consistent with common practices in climate analyses and resulting magnitudes from previous multi-model studies.

5.5 Sensitivity to Methods and Assumptions

This subsection assesses the robustness of the results with respect to key methodological choices. The estimated scaling rates showed limited sensitivity to most analysis choices. However, two notable dependencies emerged: 1) the treatment of Antarctica and 2) the order of temporal and global averaging, especially in regions with low AR event counts.

The exclusion of Antarctica was justified by low precipitation climatology and limited relevance for impact-focused analysis. More precisely, the grid cells south of 58°S were excluded additionally to the ocean grid cells. Excluding Antarctica led to a modest increase in the globally averaged scaling rates. Importantly, both internal variability and inter-model spread remained largely unchanged. The relative differences between all-, AR-associated, and non-AR scaling rates were mostly unaffected. The sensitivity likely arises from the extremely cold and dry climatology of Antarctica. At such low temperatures, absolute humidity is very small, so Clausius–Clapeyron scaling implies limited absolute increases in moisture content despite similar fractional changes. Precipitation changes are therefore constrained more strongly by circulation and moisture transport rather than by local thermodynamics, which might yield comparatively weak scaling behavior.

Scaling estimates for AR-associated events were sensitive to the order of temporal and spatial aggregation. The difference mainly occurred by either 1) producing changes on grid cell level followed by temporal and global averaging, or 2) producing temporal or global averages first and calculating changes later. In this work, all regions were treated by the first method on a grid cell level. Because grid cell areas varied due to the curvature of the globe, estimated values had to be area-weighted. For grid cells with low AR frequency, some years contained no ARs and therefore prevented the determination of changes. The grid cells were then excluded from the total area for normalization. Changing the order in the calculation decreased the AR scaling rate. Temporally averaging first increases the likelihood of at least on AR occurrence in the total temporal period and includes more area with low signal. Equivalently, spatially averaging first allows the contribution of grid cells, where few ARs occurred in the historical reference period. A small amount of AR events biases the estimation of extremes, since the annual maxima are calculated from a sparse ensemble. The inclusion of these grid cells therefore decreases the total AR scaling rates. Scaling rates for all- and noAR-associated events remained largely insensitive to the order of performed averages due to their larger sample rates. The large inter-model spread of AR scaling rates also remained unchanged.

5.6 Literature Comparison

This section compares all major findings in this work to previous studies to evaluate their robustness and consistency.

The AR catalog was calculated by the PIKART algorithm, which is presented in Vallejo-Bernal et al. 2025. The study compares the produced AR catalog results with other AR detection methods (namely tARget-4, AR-CONNECT and IPART) on the earth re-analysis-5 (ERA5) data. The observed distributions and average characteristics in this work are most similar to the PIKART results, since the same algorithm and geometric criteria were used. The number of detected AR tracks here was significantly larger, because the observed time period is longer (33 to 150 years). Extreme values of metrics like lifetime, area and IVT were also larger for the same reason, but the distributions have equal shape and similar peak values. Other detection algorithms showed different behaviors, like tARget-4 with smaller and broader AR-IVT detections. Far-future projections of AR characteristics have been studied in Payne et al. 2020 and showed a dominated thermodynamic response with increased AR-included moisture and scaling comparable to Clausius-Clapeyron similar to findings in this work. In Zhang et al. 2024 the AR catalog showed an increase in frequency, intensity, duration and spatial extent, which could only be reproduced for the intensity here. While the spatial extent assessed by length, width and area and the duration assessed by the lifetime showed mostly insignificant increases, the count of ARs showed a small but significant decrease, contrasting the findings of Zhang et al. 2024. The discrepancy likely arises from methodological differences as well as the different AR detection algorithm (namely PanLu). AR count and frequency represent distinct metrics with a possible higher frequency even for fewer counts when the spatial extent increases, since the frequency in Zhang et al. 2024 means the share of time steps with AR conditions.

In the study of Zhang et al. 2024, seasonal differences of regions with high AR frequency were observed, with similar detected dominate AR regions over large water basins for both winter and summer season. Smaller differences in the shape might be explained by the annual average in this work.

The development of global changes in near-surface air temperature has been studied in many cases for the predefined socioeconomic pathways (SSP's). As an example, the dominant amplification at the North Pole is consistent with long-established findings such as Hansen et al. 2006. Also in Tebaldi et al. 2021, a dominant temperature increase was found at the pole, with an increase similar to the ensemble and area-weighted mean of the low-frequency filtered temperature change in this work.

Links between ARs and extreme precipitation events have also been studied regionally before, with higher expected intensity, frequency and a longer duration of rainfall events in Jeon et al. 2015 and Whan et al. 2020. Results of both studies align well with findings in this work.

The different scaling of AR linked extreme precipitation compared to non-AR events has - to the authors knowledge - not been analyzed before, but Vallejo-Bernal et al. 2025 investigated different AR and non-AR included integrated water-vapor transport (IVT), which was used here to test the robustness of methods. Vallejo-Bernal et al. 2025 identified faster AR-IVT scaling in all observed regions, which overall could be reproduced here, although scaling rates were larger in the previous study presumably due to the limitation to smaller regions.

Both intensity and frequency of all extreme precipitation events showed, that the magnitude and uncertainty of scaling rates aligned well with the previous study by Kotz et al. 2023. Ensemble mean rates here remained slightly lower because of the specific model selection, which individually also showed slower rates in the previous study. This agreement supports the robustness of the applied methods. The estimated uncertainties from model spread are of similar magnitude, despite the use of only four climate model here compared to 27 in Kotz et al. 2023. Individual models partly showed different scaling results, highlighting the sensitivity of scaling rates to model-variability in the otherwise broadly similar methods.

5.7 Implications and Relevance

Climate change impacts on atmospheric rivers mostly by increased integrated water-vapor transport, directly enhancing precipitation extremes by moisture availability. Regardless of the projected magnitudes, the sign of projected changes in extreme precipitation with temperature is robust. In a warmer climate, the intensity and frequency of extreme events will increase, with potentially devastating consequences for infrastructure and human life.

Usually, precipitation is accommodated by natural or engineered drainage systems, like soil infiltration, rivers and streams and urban sewer networks. All these systems have finite capacities, which may be exceeded more frequently due to the increase in precipitation intensities. When these capacities are exhausted, floods become more likely. In addition, the increased frequency amplifies the cumulative damages and recovery challenges. A potentially stronger increase of atmospheric river caused extremes especially increases the vulnerability of exposed coastal regions, where AR caused precipitation plays a dominant role.

The differences between the scenarios highlight the dependence on future emission pathways, with significantly smaller impacts in the low-emission ssp126 compared to the high-emission ssp585 scenario. A fast implementation of mitigation strategies can help affected regions to strengthen their resilience and manage long-term risks.

5.8 Limitations and Outlook

A major limitation of this work is the restriction to a small number of general circulation models in this analysis. Especially in metrics with strong dynamical contributions, the structural differences between models result in a large range of projections. The limited number of climate models here does not fully cover this range, which may lead to a possible under-estimation of structural variability. The combination of high wind speed and humidity data for atmospheric river detection, as well as precipitation and temperature data resulted in large storage requirements, which proved to be challenging.

The same reasoning holds for additional scenarios with in-between greenhouse gas emissions, which would further increase the amount of data. The different implementation of responses to an increase in temperature and the difference of slow transitions to long-term feedback could be evaluated better with a larger range of scenarios and help to limit inter-scenario variability.

Reliance on the PIKART algorithm to detect and track atmospheric rivers does not explicitly sample methodological uncertainty or the sensitivity of AR metrics to algorithm choices and thresholds. However, using a single method ensures internal consistency for a deeper insight of the methods strengths and limitations to help evaluate results. The expansion of this analysis to multiple AR detection algorithms was beyond practical capabilities in this work.

Far-future projections generally exhibit larger uncertainties as a result of the increased model and scenario variability over time. The strong dynamical contribution to estimated metrics further increases uncertainty, resulting in large confidence intervals. The limited number of emission scenarios restricts the representation of scenario variability, which may not fully cover the true range of uncertainty. Far-future analyses benefit from distinguishing between internal variability and long-term trends and can help to separate internal fluctuations from temperature responses.

The selection of atmospheric river associated extreme precipitation events drastically reduces the number of annual events. The resulting rate-event statistics limits the reliability of annual extreme event estimates and the sparsely populated tail of the precipitation distribution can bias the definition of the 99th percentile threshold towards lower values. Scaling rates of extreme intensity, which are based on historical extremes, are therefore subject to stronger fluctuations. The frequency of extremes is evaluated as the number of events exceeding the historical 99th percentile threshold with a period from 1950 to 1970, which can also introduce larger fluctuations if the number of events in this 20 year period reduces.

The number of annual AR events is driven by atmospheric dynamics. Larger event counts in the historical reference could be realized with a longer period, but then temperature responses would start to impact the projections. The AR sample rate in far-future estimates could be improved by longer averaging periods, like decadal extremes instead of annual extremes. Another idea would be to use percentile based thresholds, like the 99th percentile used for the frequency calculation. Both ideas could improve reliability of the estimated extreme values but would lose comparability to the previous study of Kotz et al. 2023.

Expanding the analysis to a larger multi-model ensemble could improve the estimation of structural differences and capture a more robust range of inter-model scaling rates, especially for metrics with strong dynamical contributions.

The limitation of sparse atmospheric river events could be improved by geographically limiting the analysis to regions with high AR activity. This could also allow the use of higher resolution simulations, since

AR catalog metrics showed large resolution sensitivity and could provide more robust atmospheric river catalog characteristics. Extreme precipitation events are also highly resolution sensitive, which could be improved at the same time.

The relatively short historical time span was chosen to reduce the data amount, but longer time spans are typically available in most GCMs, reaching back to pre-industrial years. Their use could further reduce the influence of radiative forcing on the baseline period and the larger sample size could additionally improve AR scaling results and stabilize tail estimates of AR events.

A stronger focus on the statistical evaluation of AR extremes by the use of extreme value theory could help to provide more reliable tail estimates and improve confidence in uncertainties of AR associated extremes.

Different atmospheric river detection algorithms could enable a deeper focus on temperature-dependent AR metrics against methodological choices.

This study linked atmospheric rivers to relevant impacts by physically motivated extreme precipitation metrics, but a stronger impact focus could improve the use and interpretation of results.

Chapter 6

Conclusion

This thesis analyzed far-future projections of atmospheric rivers cataloged by the PIKART algorithm. The two future scenarios ssp126 and ssp585 with different radiative forcing were compared to simulations with historical conditions. Extreme precipitation events were assessed as intensity and frequency and separated between AR-associated and non-AR events by the spatial overlap of cataloged AR footprints with precipitation extremes.

Key findings in this work were strong AR intensity increases, a poleward shift of mid-latitude AR tracks and a possible minor decrease in annual AR counts for far-future projections. The radiative forcing feedback in extremes and global temperature was separated from internal variability by applying a low-frequency component analysis. Changes relative to a 1950-1970 baseline were then calculated on a grid cell level for all, AR-associated and non-AR extreme events. Estimated scaling rates were largely consistent with results in previous studies and align well with thermodynamic expectations. The faster scaling of integrated water-vapor transport (IVT) in ARs was significant, compared to non-AR IVT, while extreme precipitation events showed larger rates in all individual models, but no significant faster scaling due to the large inter-model spread.

The scientific contribution of this analysis is the first application of the PIKART algorithm on two future scenarios in a multi-model ensemble, further showing robustness and sensitivity of key AR changes to methodological choices. Faster scaling of AR-associated extreme precipitation events can be presumed from a faster projection in all models, but the large structural variability limits statistical significance.

Nevertheless, the significant increase in extremes with radiative forcing and the projected differences between the two scenarios show the hazardous impact of global climate change. This highlights the risk of continuing greenhouse gas emissions, while the worsening even in the scenario of limited radiative forcing illustrates the importance of mitigation and adaptation strategies. A possible faster increase of extreme precipitation events linked to atmospheric rivers shows the need to further study and understand atmospheric rivers, as their future changes can have strong regionally dependent changes.

References

Peixóto, Josè P. and Abraham H. Oort (1984). *Physics of climate.* The American Physical Society.

Boer, G. J. (1993). “Climate change and the regulation of the surface moisture and energy budgets”. In: *Climate Dynamics.*

Vincent, Luc (1993). “Morphological grayscale reconstruction in image analysis: applications and efficient algorithms”. In: *IEEE Transaction on Image Processing.* URL: `https://doi.org/10.1109/83.217222`.

Allen, Myles R. and William J. Ingram (2002). “Constraints on future changes in climate and the hydrologic cycle”. In: *Nature insight.*

Hansen, James et al. (2006). “Global temperature change”. In: *PNAS.* DOI: `https://doi.org/10.1073/pnas.0606291103`.

Oki, Taikan and Shinjiro Kanae (2006). “Global Hydrological Cycles and World Water Resources”. In: *Science.* DOI: `https://doi.org/10.1126/science.1128845`.

Etling, Dieter (2008). *Theoretische Meteorologie.* Springer-Verlag.

Hawkins, Ed and Rowan Sutton (2009). “The Potential to Narrow Uncertainty in Regional Climate Predictions”. In: *American Meteorological Society.* DOI: `https://doi.org/10.1175/2009BAMS2607.1`.

Spangler, Timothy (2012). *Introduction to Climate Models.* URL: `https://www.meted.ucar.edu/nwp/climate_models/print.htm`.

Lavers, David A et al. (2013). “Future changes in atmospheric rivers and their implications for winter flooding in Britain”. In: *Environmental Research Letters, Volume 8, Number 3.* DOI: `10.1088/1748-9326/8/3/034010`.

O’Neill, Brian C., Elmar Kriegler, et al. (2013). “A new scenario framework for climate change research: the concept of shared socioeconomic pathways”. In: *Climatic Change.* URL: `DOI:10.1007/s10584-013-0905-2`.

Gimeno, Luis, Raquel Nieto, et al. (2014). “Atmospheric rivers: a mini-review”. In: *Frontiers in Earth Science.*

Jeon, S. et al. (2015). “Characterization of extreme precipitation within atmospheric river events over California”. In: *Advances in Statistical Climatology, Meteorology and Oceanography.* URL: `https://doi.org/10.5194/ascmo-1-45-2015`.

Lavers, David A. and Gabriele Villarini (2015). “The contribution of atmospheric rivers to precipitation in Europe and the United States”. In: *Journal of Hydrology.* URL: `https://doi.org/10.1016/j.jhydrol.2014.12.010`.

O’Neill, Brian C. et al. (2015). “The roads ahead: Narratives for shared socioeconomic pathways describing world futures in the 21st century”. In: *Global Environmental Change.* URL: `http://dx.doi.org/10.1016/j.gloenvcha.2015.01.004`.

Warner, Michael D., Clifford F. Mass, and Eric P. Salathé Jr. (2015). “Changes in Winter Atmospheric Rivers along the North American West Coast in CMIP5 Climate Models”. In: *Journal of Hydrometeorology.* URL: `https://doi.org/10.1175/JHM-D-14-0080.1`.

Bauer, Nico et al. (2016). “Shared Socio-Economic Pathways of the Energy Sector – Quantifying the Narratives”. In: *Global Environmental Change.* URL: `http://dx.doi.org/10.1016/j.gloenvcha.2016.07.006`.

Eyring, Veronica et al. (2016). “Overview of the Coupled Model Intercomparison Project Phase 6 (CMIP6) experimental design and organization”. In: *Geosci. Model Development.* URL: `doi:10.5194/gmd-9-1937-2016`.

Nolting, Wolfgang (2016). *Theoretical Physics 5. Thermodynamics.* Springer Cham.

O'Neill, Brian C., Claudia Tebaldi, et al. (2016). "The Scenario Model Intercomparison Project (ScenarioMIP) for CMIP6". In: *Geosci. Model Development.* URL: `doi:10.5194/gmd-9-3461-2016`.

Riahi, Keywan et al. (2016). "The Shared Socioeconomic Pathways and their energy, land use, and greenhouse gas emissions implications: An overview". In: *Global Environmental Change.* URL: `http://dx.doi.org/10.1016/j.gloenvcha.2016.05.009`.

Guan, Bin and Duane E. Waliser (2017). "Atmospheric rivers in 20 year weather and climate simulations: A multimodel, global evaluation". In: *Journal of Geophysical Research: Atmospheres.*

Paltan, Homero et al. (2017). "Global Floods and Water Availability Driven by Atmospheric Rivers". In: *Geophysical Research Letters.* URL: `https://doi.org/10.1002/2017GL074882`.

(C3S), Copernicus Climate Change Service (2018). *Climate Data Store (CDS).* DOI: `10.24381/cds.adbb2d47`. URL: `https://cds.climate.copernicus.eu/datasets/reanalysis-era5-single-levels?tab=overview` (visited on 12/05/2025).

McSweeney, Robert and Zeke Hausfather (2018). *Q&A: How do climate models work?* URL: `https://www.carbonbrief.org/qa-how-do-climate-models-work/`.

Wills, Robert C. et al. (2018). "Disentangling Global Warming, Multidecadal Variability, and El Niño in Pacific Temperatures". In: *Geophysical Research Letters.* URL: `https://doi.org/10.1002/2017GL076327`.

Federation, Earth System Grid (2019). *ESFG Metagrid.* URL: `https://esgf-metagrid.cloud.dkrz.de/search` (visited on 12/18/2025).

Guan, Bin and Duane E. Waliser (2019). "Tracking Atmospheric Rivers Globally: Spatial Distributions and Temporal Evolution of Life Cycle Characteristics". In: *Journal of Geophysical Research: Atmospheres.* URL: `https://doi.org/10.1029/2019JD031205`.

Payne, Ashley E. et al. (2020). "Responses and impacts of atmospheric rivers to climate change". In: *Nature Reviews Earth and Environment.* URL: `https://doi.org/10.1038/s43017-020-0030-5`.

Whan, Kirien et al. (2020). "Future changes in atmospheric rivers and extreme precipitation in Norway". In: *Climate Dynamics.*

Wills, Robert C. J., David S. Battisti, and Kyle C. Armour (2020). "Pattern Recognition Methods to Separate Forced Responses from Internal Variability in Climate Model Ensembles and Observations". In: *American Meteorological Society.* URL: `https://doi.org/10.1175/JCLI-D-19-0855.1`.

Xu et al. (2020). "Image-processing-based atmospheric river tracking method version 1 (IPART-1)". In: *Geosci. Model Development.* URL: `https://doi.org/10.5194/gmd-13-4639-2020`.

Matte, Dominic, Jens H. Christensen, and Tugba Ozturk (2021). "Spatial extent of precipitation events: when big is getting bigger". In: *Climate Dynamics.* DOI: `https://doi.org/10.1007/s00382-021-05998-0`.

Michel, Clio et al. (2021). "Characterization of the atmospheric environment during extreme precipitation events associated with atmospheric rivers in Norway - Seasonal and regional aspects". In: *Science Direct: Weather and Climate Extremes.* DOI: `https://doi.org/10.1016/j.wace.2021.100370`.

Mukherjee, Sourav and Ashok Kumar Mishra (2021). "Cascading effect of meteorological forcing on extreme precipitation events: Role of atmospheric rivers in southeastern US". In: *Science Direct: Journal of Hydrology.* DOI: `https://doi.org/10.1016/j.jhydrol.2021.126641`.

Tebaldi, Claudia et al. (2021). "Climate model projections from the Scenario Model Intercomparison Project (ScenarioMIP) of CMIP6". In: *Earth Syst. Dynam.* URL: `https://doi.org/10.5194/esd-12-253-2021`.

Ashfaq, Moetasim et al. (2022). "Evaluation of CMIP6 GCMs Over the CONUS for Downscaling Studies". In: *Journal of Geophysical Research: Atmospheres.* URL: `https://doi.org/10.1029/2022JD036659`.

Gimeno, Luis, Rogert Sorí, et al. (2022). "Extreme precipitation events". In: *WIREs Water* 9 (6). DOI: `https://doi.org/10.1002%2Fwat2.1611`.

Kotz, Maximilian et al. (2023). "Constraining the Pattern and Magnitude of Projected Extreme Precipitation Change in a Multimodel Ensemble". In: *American Meteorological Society.*

Zhang, Lujia et al. (2024). "Future Changes in Global Atmospheric Rivers Projected by CMIP6 Models". In: *Journal of Geophysical Research: Atmospheres.* DOI: `https://doi.org/10.1029/2023JD039359`.

Vallejo-Bernal, Sara M. et al. (2025). "PIKART: A Comprehensive Global Catalog of Atmospheric Rivers". In: *Authorea.* URL: `DOI:%2010.22541/au.172124457.79023385/v1`.

European Commission: Joint Research Center (n.d.). Acessed on February 3, 2026. URL: `https://joint-research-centre.ec.europa.eu/jrc-news-and-updates/worlds-constructed-areas-expanding-twice-fast-population-1975-2025-11-18_en`.

Declaration of Originality

I, Lars Radtke, student registration number: 22668981, hereby confirm that I completed the submitted work independently and without the unauthorized assistance of third parties and without the use of undisclosed and, in particular, unauthorized aids. This work has not been previously submitted in its current form or in a similar form to any other examination authorities and has not been accepted as part of an examination by any other examination authority.

Where the wording has been taken from other people's work or ideas, this has been properly acknowledged and referenced. This also applies to drawings, sketches, diagrams and sources from the Internet.

In particular, I am aware that the use of artificial intelligence is forbidden unless its use an aid has been expressly permitted by the examiner. This applies in particular to chatbots (especially ChatGPT) and such programs in general that can complete the tasks of the examination or parts thereof on my behalf.

Any infringements of the above rules constitute fraud or attempted fraud and shall lead to the examination being graded "fail" ("nicht bestanden").

Place, data

Signature

Appendix A

Model Selection List

Source ID	hus, ua, va	indep	res	ensemble	6hrPlevPt
ACCESS-CM2	TRUE	TRUE	1.2 × 1.8	TRUE	FALSE
ACCESS-ESM1-5	TRUE	TRUE	1.2 × 1.8	TRUE	FALSE
AWI-CM-1-1-MR	TRUE	TRUE	≈ 0.9	TRUE	FALSE
AWI-ESM-1-1-LR	TRUE	TRUE	0.9 × 0.9	TRUE	TRUE
BCC-CSM2-MR	TRUE	TRUE	1.1 × 1.1	TRUE	FALSE
BCC-ESM1	TRUE	FALSE	≈ 2.2	TRUE	FALSE
CanESM5	TRUE	TRUE	2.8 × 2.8	TRUE	FALSE
CMCC-CM2-SR5	TRUE	TRUE	≈ 0.9	TRUE	FALSE
CNRM-CM6-1	TRUE	TRUE	≈ 0.5	TRUE	FALSE
CNRM-CM6-1-HR	TRUE	FALSE	≈ 0.4	TRUE	TRUE
CNRM-ESM2-1	TRUE	FALSE	≈ 2.2	TRUE	TRUE
EC-Earth3	TRUE	TRUE	0.7 × 0.7	TRUE	FALSE
EC-Earth3-Veg	TRUE	FALSE	≈ 0.9	TRUE	TRUE
EC-Earth3-Veg-LR	TRUE	FALSE	≈ 2.2	TRUE	TRUE
FGOALS-f3-L	TRUE	TRUE	2.3 × 2.0	TRUE	FALSE
FGOALS-g3	TRUE	TRUE	2.3 × 2.0	TRUE	FALSE
GFDL-CM4	TRUE	TRUE	1.0 × 1.3	TRUE	FALSE
GFDL-ESM4	TRUE	FALSE	≈ 0.9	TRUE	TRUE
GISS-E2-1-G	TRUE	TRUE	2.0 × 2.5	TRUE	TRUE
HadGEM3-GC31-LL	TRUE	FALSE	≈ 2.2	TRUE	TRUE
HadGEM3-GC31-MM	TRUE	FALSE	≈ 0.9	TRUE	TRUE
INM-CM4-8	TRUE	TRUE	1.5 × 2.0	TRUE	FALSE
INM-CM5-0	TRUE	FALSE	1.5 × 2.0	TRUE	FALSE
IPSL-CM6A-LR	TRUE	TRUE	1.3 × 2.5	TRUE	TRUE
KACE-1-0-G	TRUE	TRUE	2.2 × 2.2	TRUE	FALSE
MIROC6	TRUE	TRUE	1.4 × 1.4	TRUE	TRUE
MIROC-ES2L	TRUE	TRUE	4.5 × 4.5	TRUE	FALSE
MPI-ESM-1-2-HAM	TRUE	FALSE	≈ 2.2	TRUE	TRUE
MPI-ESM1-2-HR	TRUE	TRUE	≈ 0.9	TRUE	TRUE
MPI-ESM1-2-LR	TRUE	FALSE	≈ 2.2	FALSE	FALSE
MRI-ESM2-0	TRUE	TRUE	1.1 × 1.1	TRUE	TRUE
NESM3	TRUE	TRUE	1.9 × 1.9	TRUE	FALSE
NorCPM1	TRUE	TRUE	1.9 × 2.5	TRUE	FALSE
NorESM2-LM	TRUE	FALSE	1.9 × 2.5	TRUE	TRUE
NorESM2-MM	TRUE	TRUE	1.2 × 0.9	TRUE	TRUE
SAM0-UNICON	FALSE	TRUE	0.9 × 1.3	TRUE	TRUE
UKESM1-0-LL	FALSE	FALSE	≈ 2.2	TRUE	TRUE

Table A.1: List of GCM's with exclusion reasons. Highlighted are those passing all criteria and taking part in ScenarioMIP. The resolution was not considered in the selection process, since all data are interpolated to a 1° grid.

Appendix B

Low-Frequency Component Analysis Patterns

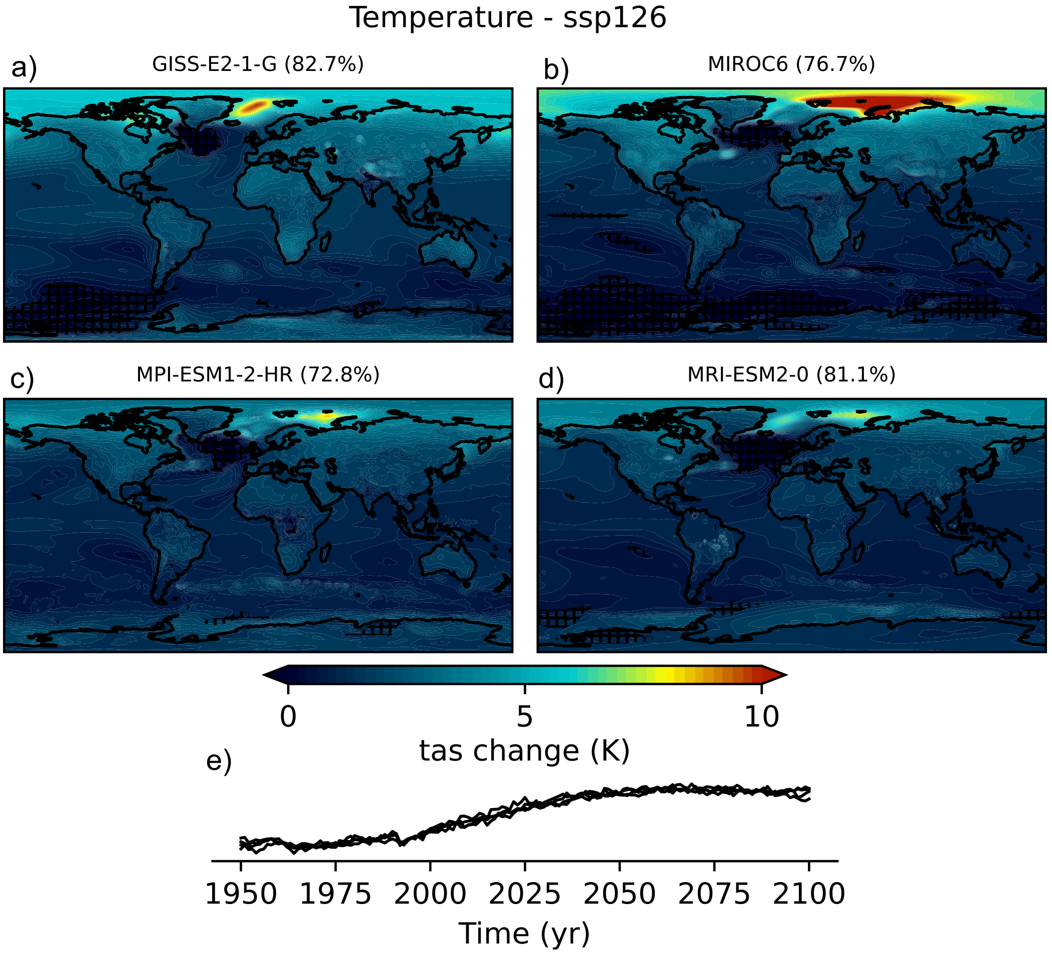

Figure B.1: As in Figure 4.6 but for the ssp126 scenario.

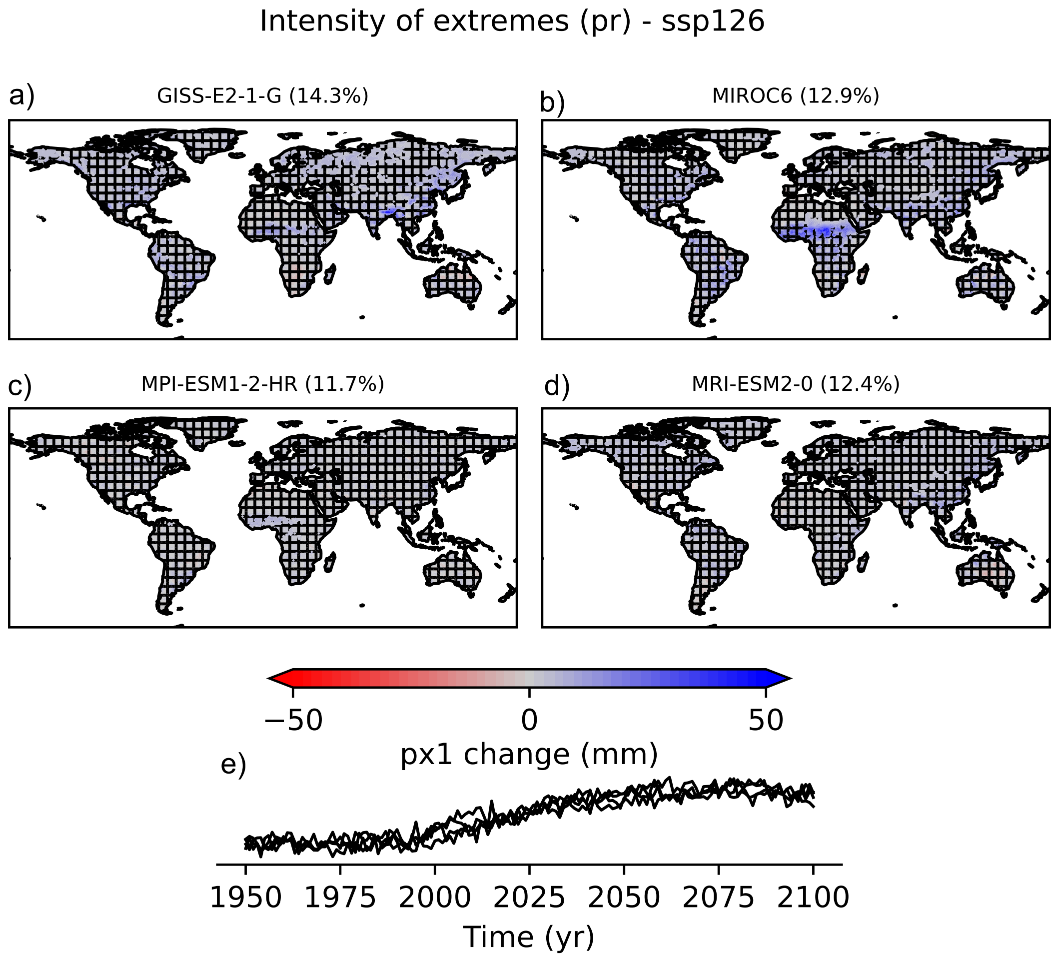

Figure B.2: As in Figure 4.6 but for low-frequency change of extreme precipitation intensity of all events (pr) for the ssp126 scenario.

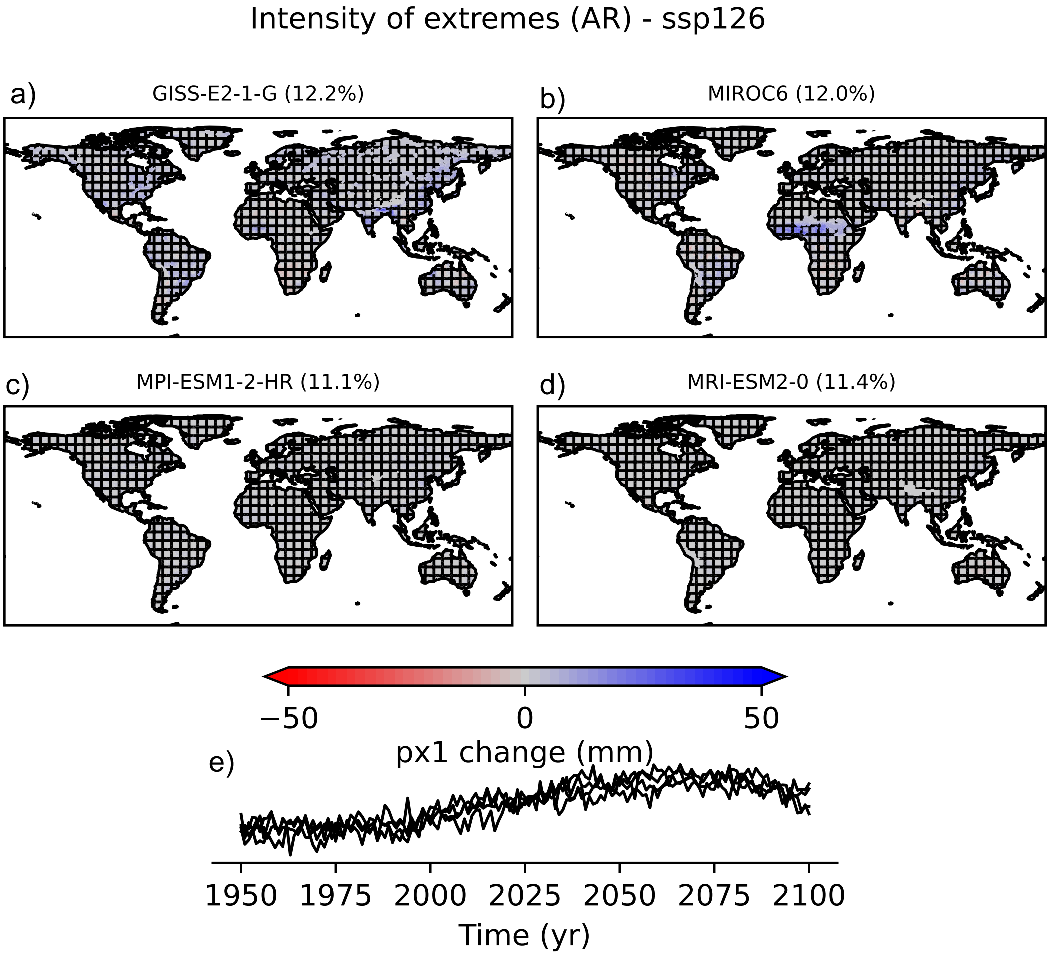

Figure B.3: As in Figure 4.6 but for low-frequency change of extreme precipitation intensity of AR-caused events (AR) for the ssp126 scenario.

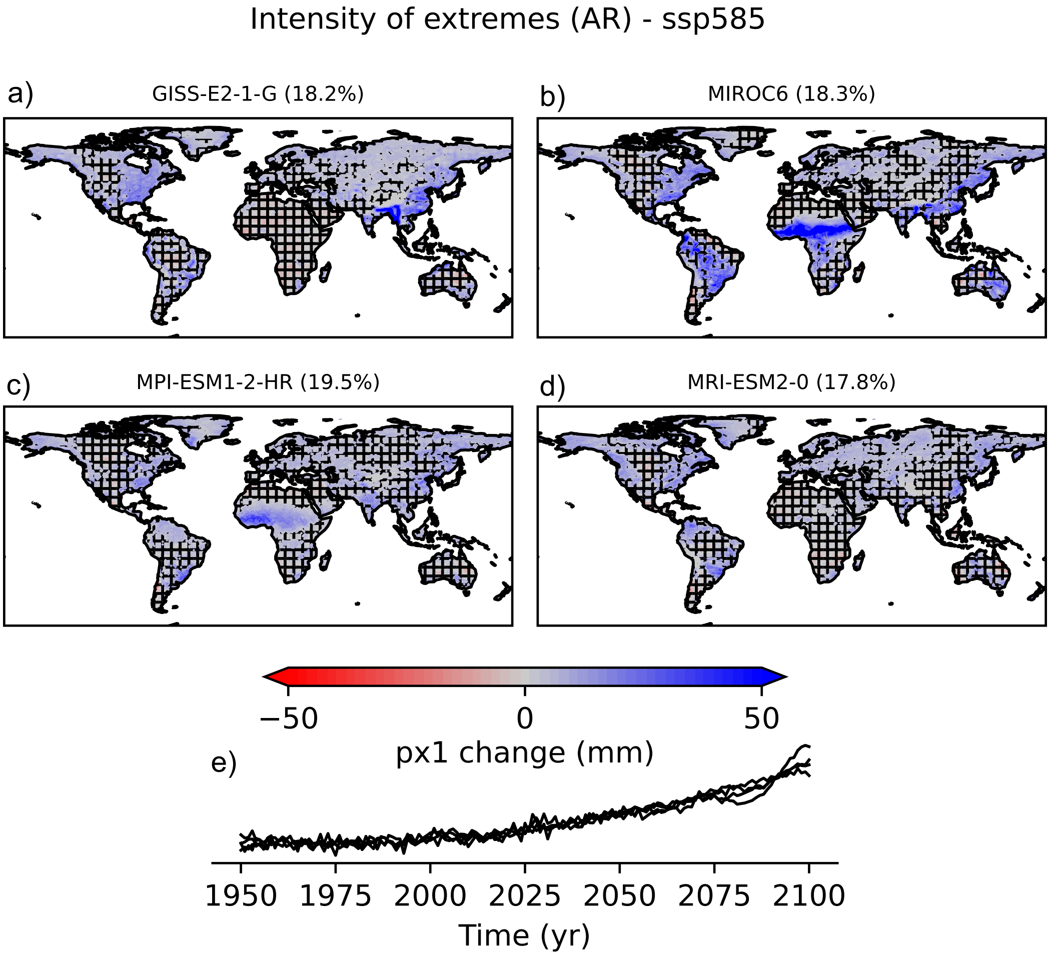

Figure B.4: As in Figure 4.6 but for low-frequency change of extreme precipitation intensity of AR-caused events (AR) for the ssp585 scenario.

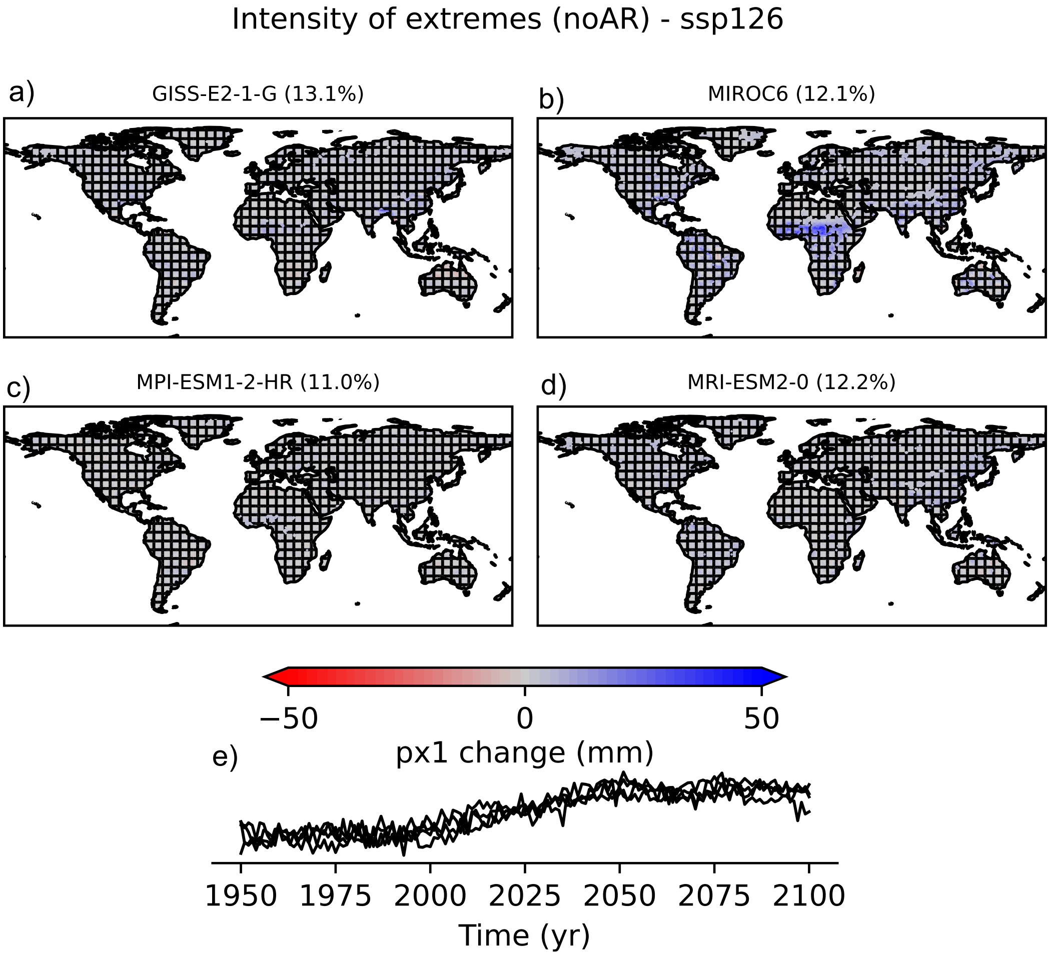

Figure B.5: As in Figure 4.6 but for low-frequency change of extreme precipitation intensity of all except AR-caused events (noAR) for the ssp126 scenario.

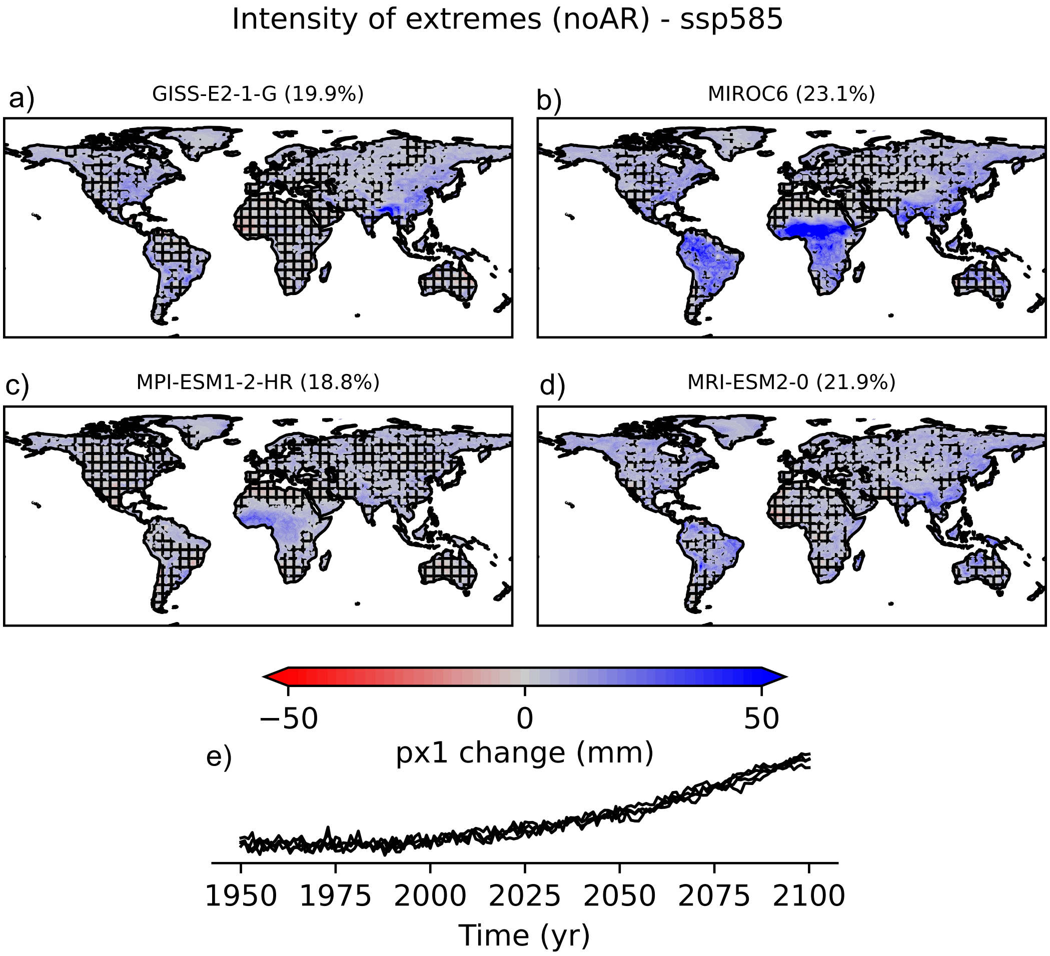

Figure B.6: As in Figure 4.6 but for low-frequency change of extreme precipitation intensity of all except AR-caused events (noAR) for the ssp585 scenario.

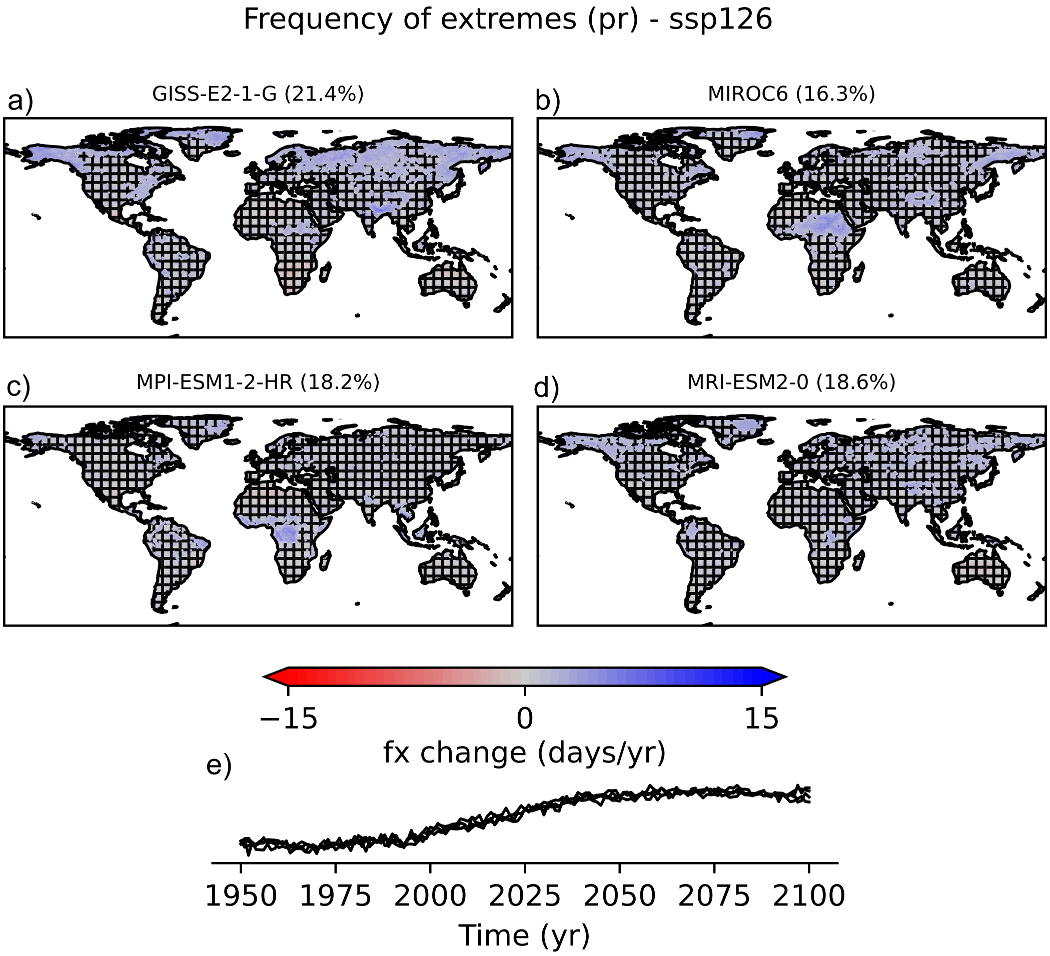

Figure B.7: As in Figure 4.6 but for low-frequency change of extreme precipitation frequency of all events (pr) for the ssp126 scenario.

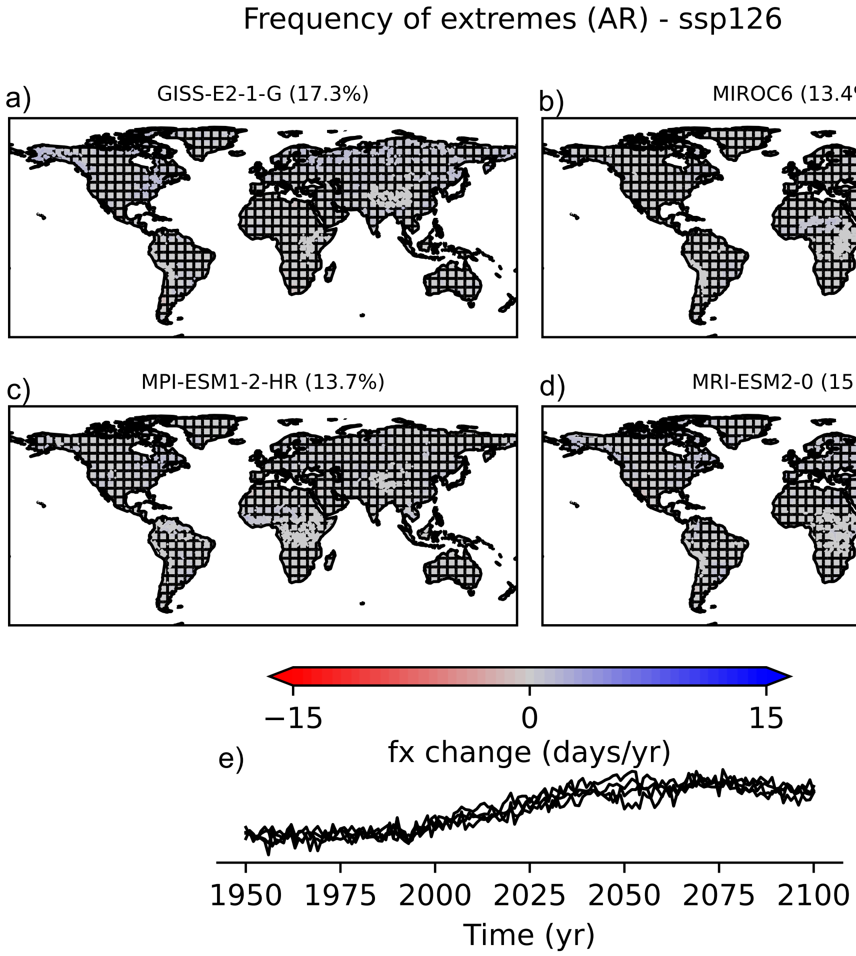

Figure B.8: As in Figure 4.6 but for low-frequency change of extreme precipitation frequency of AR-caused events (AR) for the ssp126 scenario.

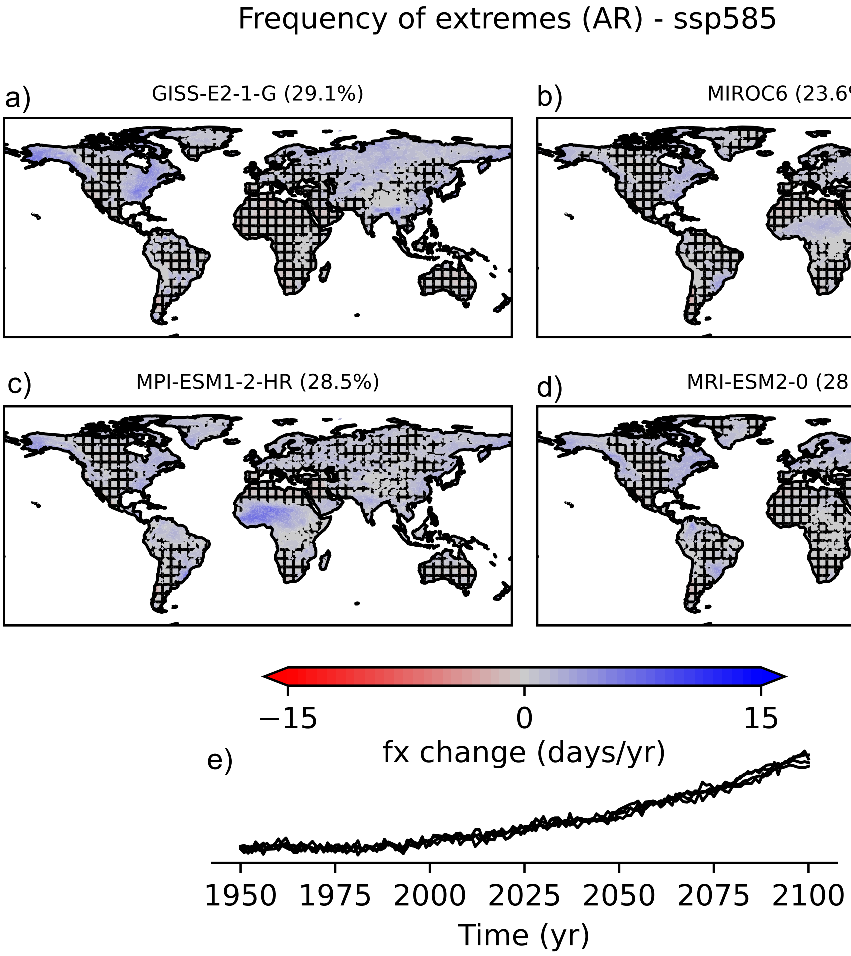

Figure B.9: As in Figure 4.6 but for low-frequency change of extreme precipitation frequency of AR-caused events (AR) for the ssp585 scenario.

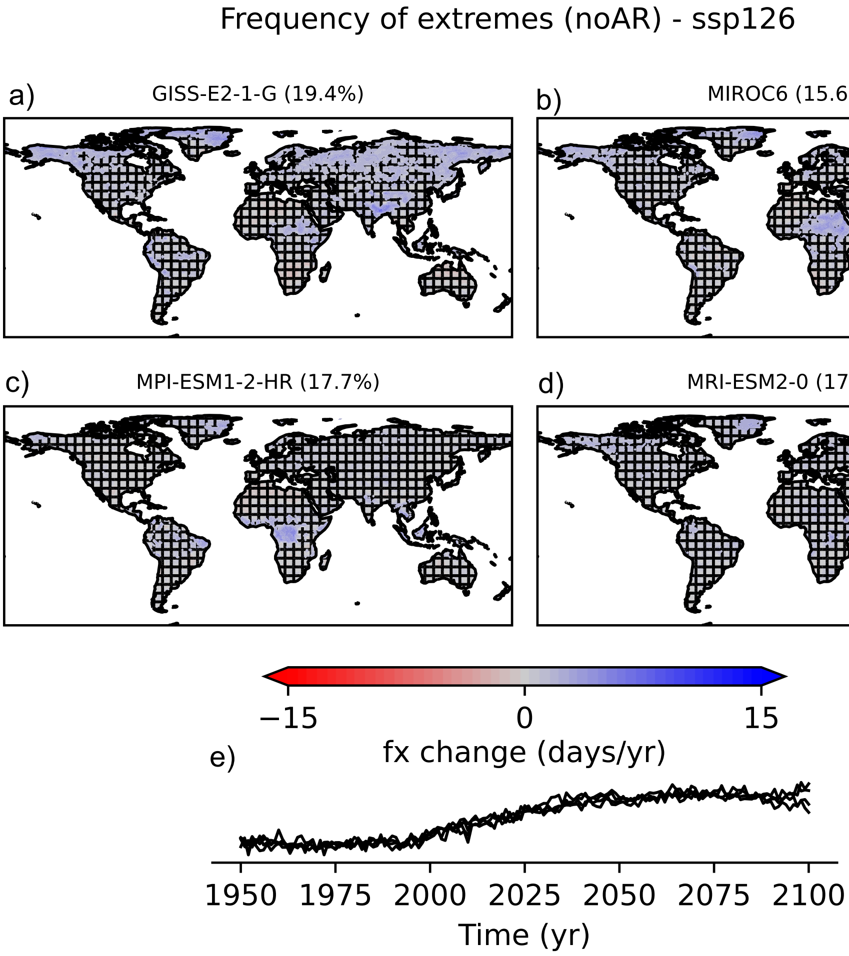

Figure B.10: As in Figure 4.6 but for low-frequency change of extreme precipitation frequency of all except AR-caused events (noAR) for the ssp126 scenario.

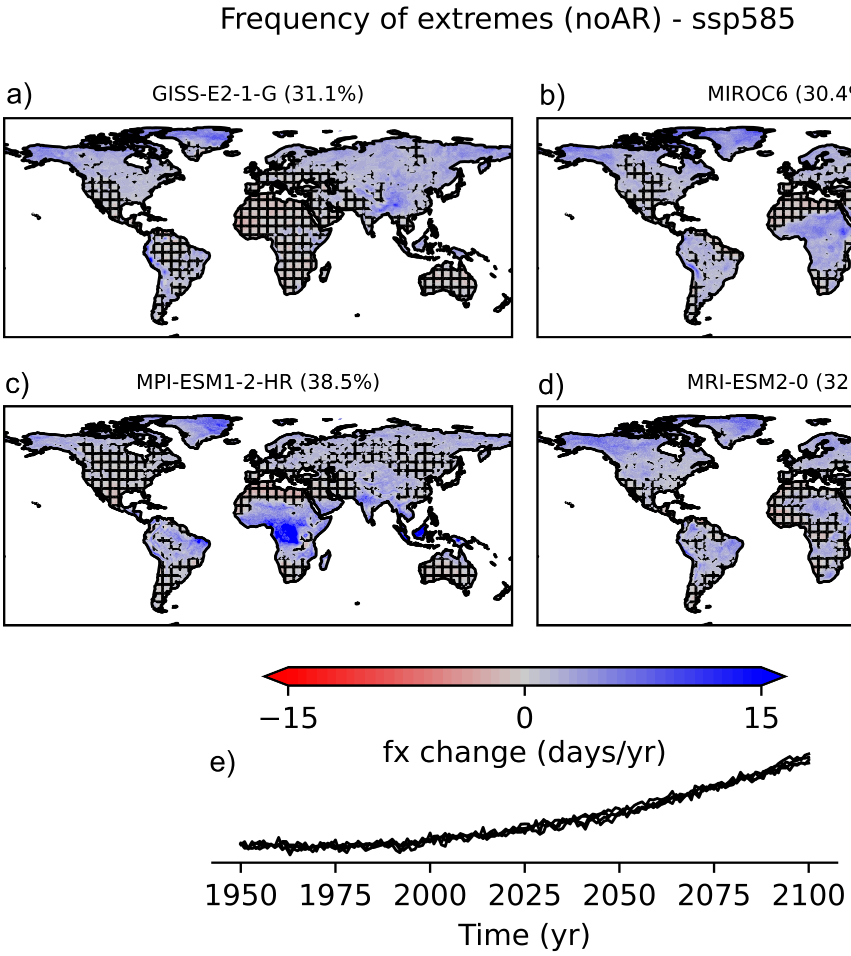

Figure B.11: As in Figure 4.6 but for low-frequency change of extreme precipitation frequency of all except AR-caused events (noAR) for the ssp585 scenario.

Appendix C

Annual scaling rates for individual models

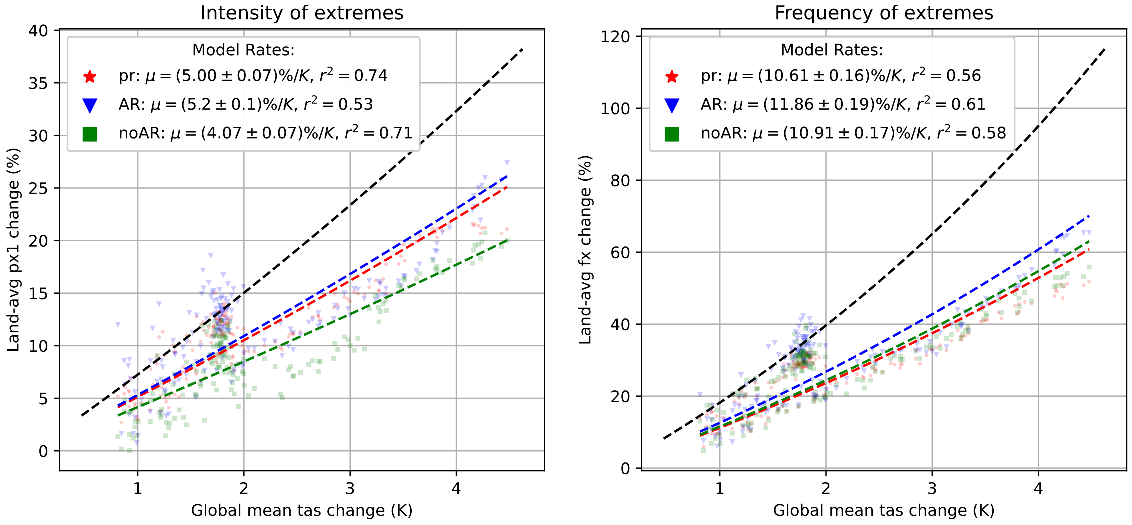

Figure C.1: Exponential scaling rates based on annual estimates of extremes as in Figure 4.11, but only for results of the model GISS-E2-1-G.

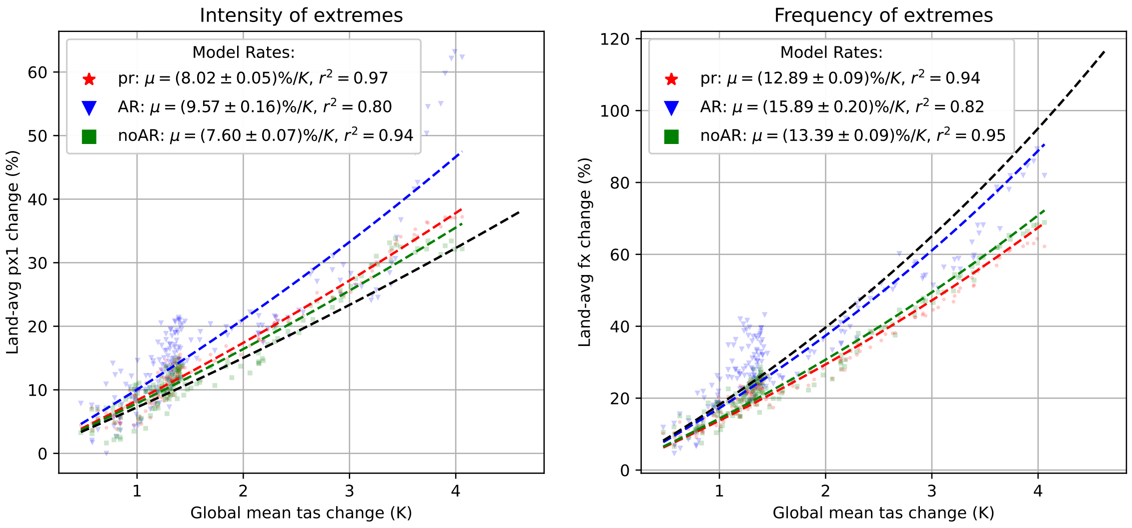

Figure C.2: Exponential scaling rates based on annual estimates of extremes as in Figure 4.11, but only for results of the model MIROC6.

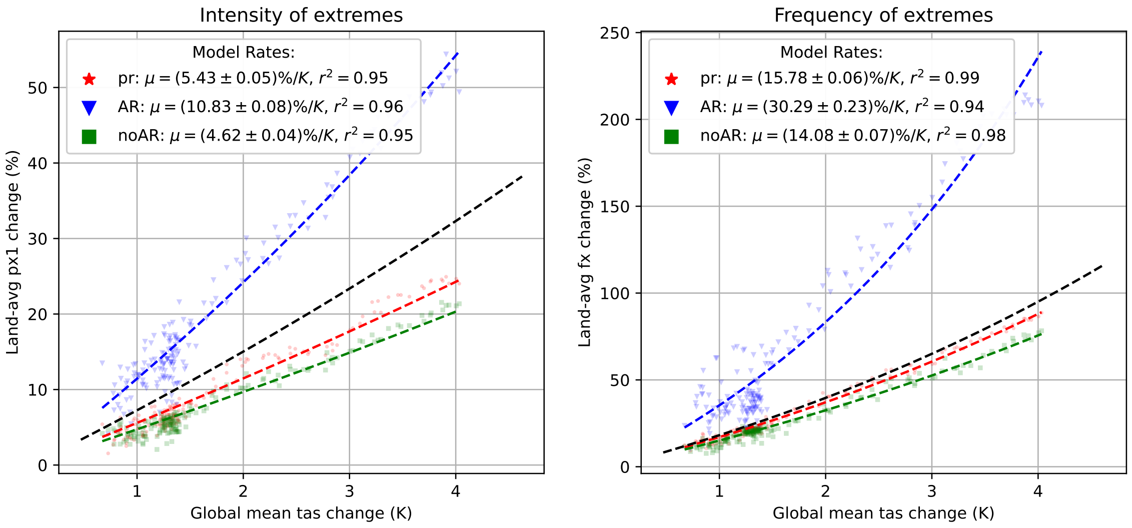

Figure C.3: Exponential scaling rates based on annual estimates of extremes as in Figure 4.11, but only for results of the model MPI-ESM1-2-HR.

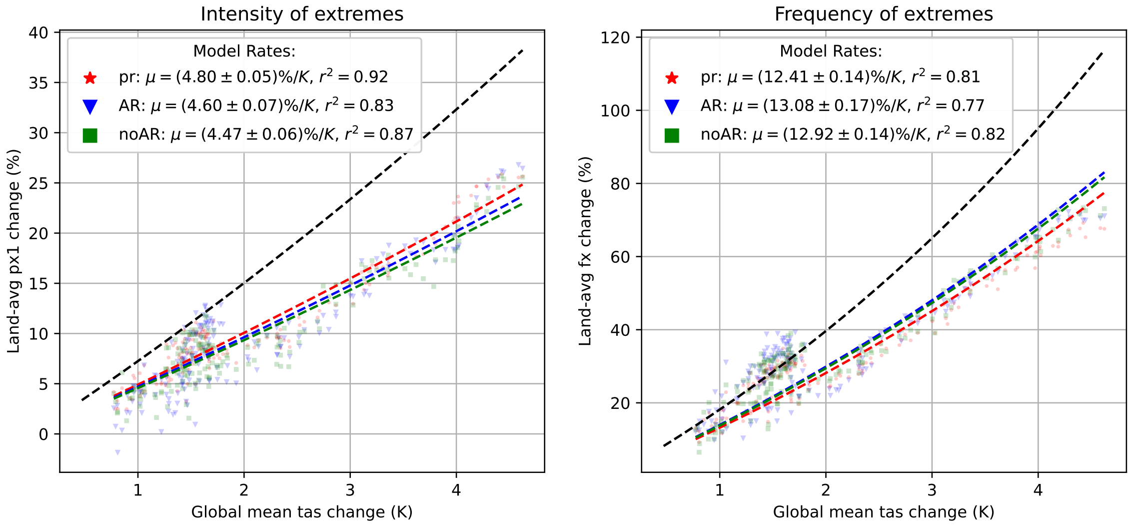

Figure C.4: Exponential scaling rates based on annual estimates of extremes as in Figure 4.11, but only for results of the model MRI-ESM2-0.